ABSTRACT

Title of Dissertation: MODELING AND CHARACTERIZATION OF BIOINSPIRED HYBRID FLAPPING/GLIDING FLIGHT FOR FLAPPING WING AIR VEHICLES

Lena Johnson
Doctor of Philosophy, 2022

Dissertation Directed by: Professor Hugh Bruck
Department of Mechanical Engineering

Unmanned Aerial Vehicles (UAVs) are increasingly being used for applications that require longer, reliable flight duration and distances. The greatest limitation to achieving these desired flights is the current on board battery technology which, restricted by internal chemistry and external size, can only provide a finite amount of power over time. Efforts to increase the battery's efficiency and energy storage tend to rely on cumbersome methods that add weight and/or complexity to the system. However natural flyers, though also limited by a finite amount of internal energy gained through food consumption, are able to extend their flights through techniques that either utilize their inherent aerodynamic advantages or advantageously employ atmospheric phenomena. Flapping-Wing UAVs (FWUAVs) are as limited by their onboard battery as any other type of UAV, but because of their bio-inspired functionality are uniquely suited to utilize natural flight extension methods. Therefore, this PhD presents an analysis of the exploration of bio-inspired, hybrid flapping/gliding, also known as intermittent gliding, techniques to improve the flight per-

formance of a FWUAV. Robo Raven is the FWUAV that was chosen as the research platform for this work. It was developed by researchers at the University of Maryland to perform prolonged, untethered flights and exhibit a flight proficiency that combined the maneuverability of rotary-wing flight with the efficiency of fixed-wing flight. The technique to improve FWUAV flight time, presented in this work incorporates (1) the modeling of Robo Raven's flapping/gliding potential through the development of a state-space representation directly linking Robo Raven's onboard battery dynamics with its aerodynamic performance, (2) the use of the state-space model to characterize the effect of intermittent gliding techniques on flight performance through simulation, (3) the real-world characterization of the simulation and of intermittent gliding techniques through flight demonstrations, and (4) the development of a design space by which the effect of wing design on gliding performance might be explored and lead to the potential tailoring of wing design to desired flight performance. The expected outcome of this technique is scientific analysis of the extension of Robo Raven's flight time without added complexity of weight of the battery system.

MODELING AND CHARACTERIZATION OF BIOINSPIRED HYBRID FLAPPING/GLIDING FLIGHT FOR FLAPPING WING AIR VEHICLES

by

Lena D. Johnson

Dissertation submitted to the Faculty of the Graduate School of the
University of Maryland, College Park in partial fulfillment
of the requirements for the degree of
Doctor of Philosophy
2022

Advisory Committee:
Professor Hugh Bruck, Chair/Advisor
Professor Derek Paley, Dean's Representative
Professor Miao Yu
Professor Mikhil Chopra
Assistant Professor Yancy Diaz-Mercado

© Copyright by
Lena D. Johnson
2022

ACKNOWLEDGEMENTS

First of all, I would like to thank my Lord and Savior Jesus Christ. You have given me the ability to make this work. You have fathered me through medical nightmares and personal loss. Even though I have walked through the valley of the shadow of death I have feared no evil for You are with me. I would like to acknowledge Dr. Hugh A. Bruck for his excellent work as my advisor and mentor these past ten years. I would also like to thank Dr. Paley for helping me finish my dissertation. Thank you to all of the students I have mentored over the years, particularly Keene, Luxi, Ashley, Carla, Benz, Zach, Matthew, and Dior. You have inspired me and make me try to be better. Finally, a great thank you to my mom, Beverley Johnson, my dad, Richard Johnson, and my family (both spiritual and natural) who have always loved, cared for and supported me. A final acknowledgement to my amazing aunt, Gwendolyn Prioleau, and my wise grandmother, Caroline Prioleau, who passed away as I was pursuing this degree. I have so wished for you to see this day, but knowing our Father in heaven, you probably have seen it.

TABLE OF CONTENTS

Acknowledgments ii

List of Tables vi

List of Figures viii

Chapter 1: Introduction 1

1.1 Motivation 1

1.2 Relation to the State of the Art 2

1.2.1 Natural Flyers and the Mechanics of Naturally Efficient Flight 2

1.2.2 Current Unmanned Aerial Vehicle Flight Time Extension Methods 4

1.2.3 Introduction to Phugoid Dynamic Modeling 13

1.2.4 Introduction to Battery Dynamics Modeling 14

1.2.5 RoboRaven Platform Review 16

1.3 Technical Approach 18

1.4 Contributions of Dissertation 19

1.5 Outline of the Dissertation 21

Chapter 2: Technical Background 22

2.1 Phugoid Dynamics and Modeling 22

2.2 Battery Dynamics and Modeling 24

2.3 RoboRaven Platform Review 26

Chapter 3: State Space Modeling the Flight Dynamics and Battery Utilization for Hybrid Flap/Glide Flight 30

3.1 Extension of Phugoid Model 30

3.2 Extension of Battery and Motor Model 34

3.3 Glide Cycle Design and Performance Analysis 39

3.3.1 Time-based switching 39

3.3.2 Altitude-based switching 42

3.3.3 Voltage-based switching 43

3.4 Conclusion 45

Chapter 4: Gliding Wing Design and Performance Characterization 46

4.1 The Study of Glide Performance and Wing Geometry 46

4.2 Development and Analysis of Chosen Wing Geometries 48

4.2.1 The Original Robo Raven1 Wing Planform 50

4.2.2 The Chosen Wing Planforms 50

4.3 Experimental Study of Chosen Wings 52

4.3.1 Wing Prediction Study Using Test Stand Characterization 52

4.3.2 Flight Analysis of Gliding Wings 56

4.4 Summary of Gliding Wing Characterization Results 65

4.5 Conclusion 66

Chapter 5: Flight Validation of Hybrid Flapping-Gliding State Space Model 68

5.1 Description of Modified Experimental Test Bed: Robo Raven 1 68

5.1.1 Measurement of Battery Voltage 69

5.1.2 Final Robo Raven 1 Configuration and Block Diagram 71

5.2 Experimental Flight Test Results 72

5.2.1 Demonstration of Continuous Flapping Flight Behavior 72

5.2.2 Demonstration of Hybrid Flapping/Gliding Flight 77

5.3 Analysis of Aerodynamic Performance 84

5.3.1 Experimental Analysis of $C_{L,flap}/C_D$ Ratio 84

5.3.2 Modified Simulation of $C_{L,flap}/C_D$ Ratio based on Experimental Results . . 86

5.4 Conclusion 88

Chapter 6: Conclusion 90

6.1 Scientific and Technical Contributions 90

6.1.1 State Space Modeling the Flight Dynamics and Battery Utilization for Hybrid Flap/Glide Flight 90

6.1.2 Gliding Wing Design and Performance Characterization 90

6.1.3 Flight Validation of Flapping-Gliding State Space Model 91

6.2 Ongoing and Future Work 91

References 104

LIST OF TABLES

2.1 RoboRaven1 Wing Parameters 27

2.2 Comparison of properties of Robo Raven1 and Common Raven 28

3.1 Number of teeth for each internal gear 32

3.2 Initial conditions of the combined flight, motor, and battery dynamical system . . . 37

3.3 Parameters of the combined flight, motor, and battery dynamical system 38

4.1 A comparison of the percent change in planform parameters between the original Robo Raven wing and the chosen wing specimens. The design chosen wing planform specimens were further inspired by the natural fliers of (a) a crow (b) an eagle and (c) an albatross [110] 51

4.2 Measured parameters for the original Robo Raven 1 wing and each wing planform specimen 52

4.3 Calculated slope of $\Delta C_{L,glide}$ from the previous wing A data that was used to calculate Δ lift for each of the wing specimens 55

4.4 Calculated average $C_{L,glide}/C_D$ ratio values for the original Robo Raven wing specimens after using a linear fit of the flight path data and the final overall average and standard deviation of the $C_{L,glide}/C_D$ ratio 60

4.5 Calculated flight path angle θ values for each linearized path for each wing specimen 62

4.6 Calculated average $C_{L,glide}/C_D$ ratio values for each of the wing specimens after parameterizing the flight path and the final average $C_{L,glide}/C_D$ ratio for each wing specimen 62

4.7 Final summary of gliding wing characterization relating wing planform to slope of Lift and $C_{L,glide}/C_D$ values using information from the prediction study and the flight analysis 66

5.1 Weight account of the Modified Robo Raven1 Platform 69

5.2 $\Delta V_{bat}$for each of the continuously flapping flight demonstrations 77

5.3 ΔV_{bat} for each of the 1 glide and 2 glide hybrid flight demonstrations 82

5.4 A comparison of the voltage drop vs. flight time for each of the flights and the average value for each flight method 83

5.5 A comparison of the flight distance vs. flight time for each of the flights and the average value for each flight method. 83

5.6 A comparison of the voltage drop vs. flight distance for each of the flights and the average value for each flight method. 83

5.7 A comparison of the aerodynamic coefficient ratios between the original simulation values and the final values from this experiment. As can be seen, the values are very far off because the simulation assumed an optimized platform as stated before. Using the values from the experiment, the simulation values were modified to more system correct values 85

5.8 Adjusted initial conditions of the combined flight, motor, and battery dynamical system 86

5.9 A comparison of the aerodynamic coefficient ratios between the experimental and modified simulations. The experimental coefficient of thrust C_T value was calculated using information from past drag experiments. The more correct coefficient of thrust C_T was calculated according to the ratio values. 88

LIST OF FIGURES

1.1 Graphical representation of sinusoidal bounding. The graph shows the altitude and body angle overtime of a bird in bounding flight with the corresponding flapping or gliding mode [19]. 4

1.2 Comparison of (a) dynamic soaring flight path simulation showing the stages of a dynamic soaring path [34] vs. (b) static soaring flight path showing the use of up drafts for flight paths [35] 6

1.3 Examples of fixed-wing UAVs used in autonomous soaring experiments (a) A powered fixed-wing glider used at Dryden Airforce base [41] (b) The ALOFT glider UAV used in flight experiments [39] 9

1.4 Flapping flight platforms (a) BatBot [58], and (b) Delfly [53, 59] 11

1.5 Examples of Micro-Scale UAVs (a) RoboBee [3] (b) Harvard Robot Moth [66] . . 13

1.6 Pictorial examples of battery models (a) A 1st order Thevenin equivalent equivalent circuit model [81] (b) A two-well, kinetic battery model [76] 15

1.7 Examples of the Robo Raven platform (a) Robo Raven 1 [56] (b) Robo Raven 3 [4, 25, 97] (c) Robo Raven 5 [49, 99] 17

1.8 Flow diagram representing the technical approach of this dissertation 19

2.1 The forces and coordinates of the phugoid dynamics, after [75]. The $\hat{e}_1, \hat{e}_2$ coordinates represent the world frame and the $\hat{b}_1, \hat{b}_2$ represent the platform frame at the center of gravity 23

2.2 Phase portraits of (a) gliding phugoid dynamics with $C_{L,glide}/C_D = 20$; (b) flapping phugoid dynamics with $C_{L,flap}/C_D = 5$ 24

2.3 The equivalent circuit model for battery discharge 25

2.4 (a)The RoboRaven 1 platform developed at the University of Maryland [99] (b) A diagram of the RoboRaven1 100% wing [49, 95, 4] 27

2.5 The RoboRaven1 hardware system diagram. 29

3.1 This figure shows the reference motor circuit from which the motor model equations were derived. 34

3.2 The effect of $K_{R_{bat}}$ on the battery resistance $R_{bat} = R_{bat}(Z_{bat})$ 36

3.3 This graph shows the results of experimentally obtained values of wing stiffness. . 37

3.4 Simulation of continuous flapping mode: (a) longitudinal dynamics; (b) angular rate; and (c) onboard energy usage. 39

3.5 Model simulation with a 30-10 second duty cycle: (a) longitudinal dynamics; (b) angular rate; and (c) onboard energy usage. 40

3.6 Longitudinal dynamics with (a) time-based switching; and (b) altitude-based switching 41

3.7 Simulation results for time-based switching: (a) battery endurance vs. glide cycle; and (b) flight distance vs. glide cycle 41

3.8 Flight distance and battery endurance for time-based switching. The red dots show the points chosen for the simulation results described above. 41

3.9 Simulation results for altitude-based switching: (a) battery endurance vs. altitude-based cycle; and (b) flight distance vs. altitude-based cycle 43

3.10 Flight distance and battery endurance for altitude-based switching. The ”null” space above the altitude outputs represent impossible altitude combinations where the minimum altitude is larger than the maximum. The red circles show the points tested by the original simulation. 43

3.11 Longitudinal dynamics using voltage-based switching 44

3.12 Simulation results for voltage-based switching: (a) battery endurance vs. voltage-based cycle; and (b) flight distance vs. voltage-based cycle 44

3.13 Performance of voltage-based switching mode 44

4.1 Geometric representation of Robo Raven 1 baseline wing with important design space parameters 49

4.2 The original Robo Raven1 Wing. 50

4.3 The Robo Raven 1 configured test stand (a) while flapping [95] (b) with the force direction notated [97] 53

4.4 Raw lift vs. angle of attack data from previous wing experiments for wing A in a 5 m/s airflow wind tunnel. This experiment looked at the gliding behavior with two wings on the test stand 54

4.5 Interpolated, predicted slope of Δ lift values, scaled for each of the wing specimens according to slope of Δ angle-of-attack 55

4.6 The gliding dynamics of Robo Raven1 57

4.7 Pictures of the GPS sensor system showing (a) the Teensyduino and GPS and (b-c) the position of the GPS on the platform 59

4.8 The graphical results of the $C_{L,glide}/C_D$ ratio experiments 60

4.9 Flight demonstration results for the (a) Wing A (b) Wing B and (c) Wing E 62

4.10 Modeled bilinear surface of $C_{L,glide}/C_D$ ratio as a function of aspect ratio, AR and planform area, A_w 64

4.11 Comparison of displacement in Robo Raven wings during downward flapping. It displays the effect of variable in wing stiffness on wing flexion. This characterization was originally conducted in previous Robo Raven research by Perez-Rosado [116]. The region of high convexity in the original Robo Raven wing can be seen in the red circle. 64

4.12 Measured thrust and lift values for wings A and B from previous research [56, 95] Please note, "wings C and D" have not been used in this chapter's gliding evaluations, but represent wings that have similar AR as wings A and B but have been scaled up in area. 65

5.1 Voltage sensor (a) circuit and (b) picture 70

5.2 The modified Robo Raven 1 hardware system diagram 71

5.3 The modified Robo Raven 1 software system diagram 72

5.4 Flight demonstration results of continuous flapping flight (a) 2D phugoid profile, (b) Latitude vs. Longitude during flight for the three represented flights 76

5.5 (a) Raw voltage vs. time (b) voltage data trend lines for each flight 77

5.6 Flight demonstration results of 2D phugoid profile for hybrid flapping-gliding flights with (a) one gliding cycle (b) two gliding cycles 79

5.7 Flight demonstration results of Latitude vs. Longitude during flight with (a) one gliding cycle (b) two gliding cycles 80

5.8 Voltage discharge vs time for the hybrid flapping-gliding flights with (a) one gliding cycle (b) two gliding cycles 81

5.9 Average ΔV_{bat} values for the full flapping, 1 glide hybrid and 2 glide hybrid flights 83

5.10 A comparison of (a) the graphical results of the $C_{L,flap}/C_D$ ratio experiments with (b) the original simulated longitudinal dynamics 85

5.11 A comparison of longitudinal dynamics for a fully flapping phase and a 1 glide hybrid phase for both the experimental flight paths and the modified simulations. The C_L/C_D ratio values for both flap and glide were achieved by adapting the C_T parameters to the flight apparatus and qualitatively fitting the curves to more geometrically fit the experimental curves. 87

5.12 Comparison of experimental results for longitudinal dynamics for a fully flapping phase and a 1 glide hybrid phase modified with the simulation using a C_L/C_D of 3 for glide and 1 for flapping, which are closer to what we expect from the Robo Raven 1 platform. The resulting simulated flight paths were also within the range of experimental measurements, similar to the flight paths in figure 5.11 that were qualitatively fit. Thus, it could be concluded that the sensitivity of the simulation to C_L/C_D values was in the range of uncertainty for the experimental data. 88

6.1 A pictoral representation of the PID controller parameters [98] 93

6.2 A closeup of the Robo Raven 5 platform. Note the increase in payload afforded by the rear propellers 94

CHAPTER 1
INTRODUCTION

1.1 Motivation

Unmanned Aerial Vehicle (UAV) technology is expanding to applications that require longer, more reliable flight times and distances. Nonetheless, the limitations of battery life and flight efficiency continue to be a hinderance to this goal [1]. Flight time is determined, primarily, by the amount of battery power provided to the thrust and lift generating actuators overtime. Therefore, overcoming this obstacle is necessary if UAV technology will continue to expand into new application areas.

Natural flyers face similar challenges. In a sense, they continually fly on a fixed amount of "fuel" generated through their body's utilization of food. However, their flight time can vary greatly depending on the weather, their hunting behaviors, or the time of the year. Amazingly, they are able to increase or decrease their flight time without necessarily increasing or decreasing their fuel intake. They do this by effectively utilizing atmospheric phenomena such as wind changes, and thermals, or by intelligently cycling from flapping to not flapping. This is especially true and important during long migrations.

Attempting to directly mimic this flight prolonging behavior to improve battery life would, therefore, require a UAV platform sufficiently suitable to performing natural flight. For this reason, bio-inspired flapping-wing flight platforms (FWUAVs) and bio-inspired energy harvesting methods have been investigated as potential technologies capable of efficient, extended flight time. Bio-inspired, flapping-wing, flight platforms (FWUAV) have increased in sophistication and capability since the turn of the current century. The technology is being used in a wider range of applications, such as animal control on a flight line [2]. However, they are often limited by weight, the power required for flapping, and the ability to sustain prolonged, untethered flight [3, 4]. Fixed-wing UAV attempts to mimic natural energy harvesting methods such as gliding or soaring can be

found [5, 6, 7]. However, few researchers have combined FWUAV technology with these methods as a means of improving flight. Therefore, there remains the potential to combine FWUAV technology with energy-harvesting flight methods to prolong battery life. This work will be focused on exploring the combination of bio-inspired flight extension methods with FWUAV technology.

1.2 Relation to the State of the Art

In this section, the current science and state-of-art aerial flight time extension methods will be discussed. Furthermore, background information critical to the understanding of FWUAVs and the approach described in this work will be presented.

1.2.1 Natural Flyers and the Mechanics of Naturally Efficient Flight

Natural flyers, such as birds, bats, and various flying insects, have been observed by human scientists and engineers for millennia [8, 9]. Many of the earliest attempts at human flight were based upon the observation of and mimicking of natural flight behavior [8, 9, 10]. In observing natural flight, researchers have gained an understanding of the aerodynamic fundamentals that make natural flight possible. One important foundation of natural flight is the frequent interchange during flight between different aerodynamic regimes. Birds in particular can exhibit flight in the steady-state aerodynamic regime when gliding or soaring, characterized by a laminar flow field around the bird that does not alter with time [11, 12]. However, when flapping, birds can transfer into a quasi-steady state aerodynamic regime, characterized by an attached, though time sensitive, flow field over the body [12, 13, 14, 15]. Depending on anatomical size and flapping speed a bird can move even further into an unsteady aerodynamic flight regime, characterized by a separation of the boundary layer from the body [12, 14, 16, 17]. Each regime is scientifically dissimilar to each other and requires separate physical and mathematical characterizations. Nonetheless, they are each integral to natural flyers' ability to produce and sustain flight.

The majority of artificial flying machines are designed to work in laminar flow streams, induced by smooth airfoils. In contrast, the feathers of a bird, though rough and pocketed, can induce strate-

gic sections of turbulent flow across the chord and leading edge of its wings [16, 18]. This results in a laminar boundary layer, induced over the sections of turbulence, that enable flight through flapping. Furthermore, the aeroelasticity of a bird's wing, exhibited by its constant deformation during flapping allows for the real-time manipulation of flow fields to improve flight performance [15]. Natural flyers are highly adept at using these and other aspects of flapping flight to their aerodynamic advantage.

Continuous flapping flight, however, is not very energy efficient and therefore bird species are adept at using a variety of methods to conserve energy. These methods can be broken into two categories; methods that are based solely on natural aerodynamics or behaviors and methods that advantageously utilize atmospheric phenomena [12, 19]. The first category includes such flight modes as bounding flight, intermittent gliding and formation flying [19]. Bounding flight and intermittent gliding rely solely on the bird's ability to generate enough forward velocity, through repetitive maneuvers, to sustain non-flapping flight. Pennycuik [13] modeled intermittent gliding behavior using a glide polar, the formula for which is a ratio of forward velocity and sinking speed. The forward velocity must overcome a bird's stalling speed and, therefore, is affected by the wing's ability to generate lift. Videler [19] modeled bounding flight as a sinusoidal behavior wherein birds generate propulsion through fast flapping and then shoot themselves forward with their wings pulled back. Furthermore, both Videler and Pennycuik [13, 19] spoke on the benefits of formation flying for preserving energy as the forward drag is lessened by the front bird in formation.

The second category of flight includes flight modes that tend to save a higher degree of energy than the first flight modes and are often used for prolonged flight. These flight modes include static and dynamic soaring and wind gliding [13, 19]. Dynamic soaring is a method by which birds tack into wind speed gradients to generate lift and propel themselves forward without flapping. Sachs [20] completed in-flight, on-bird measurements of this process and determined that the energy gain necessary for non-flapping propulsion is achieved at the upper curve of the dynamic soaring cycle when the bird tacks its direction vector into the leeward flow of the wind. Furthermore, work

done by Sachs and Denny [21, 22] speak to the curve profile of dynamic soaring and discusses the variations in this profile as well as the advantages and disadvantages in these variations as a matter of energy calculations. Static gliding is another methodology that has been widely studied, during which birds use the lift energy from rising thermals to propel themselves to higher altitudes [23].

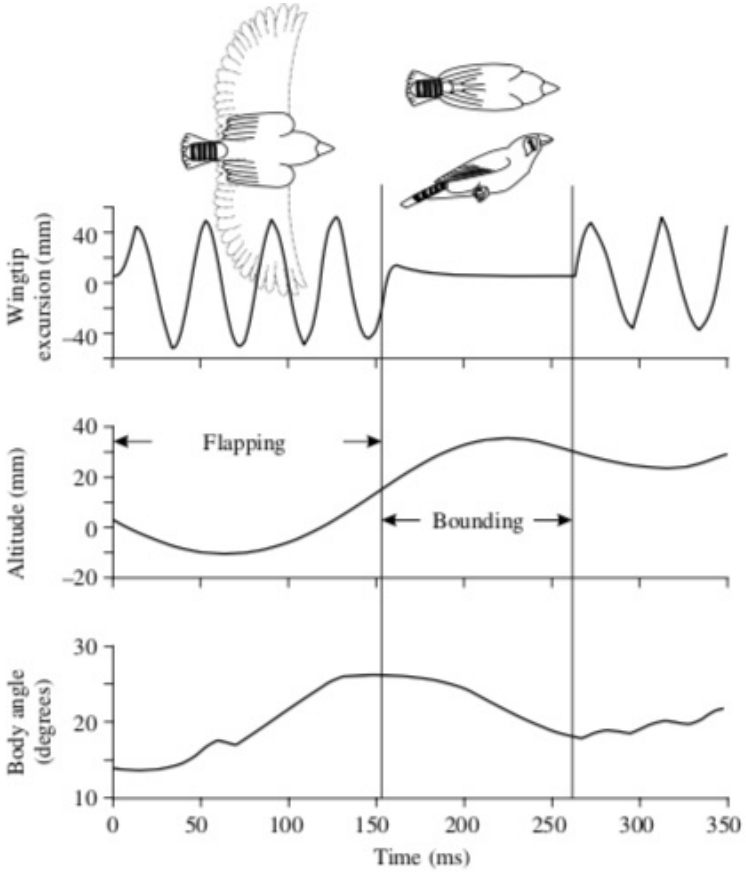


Figure 1.1: Graphical representation of sinusoidal bounding. The graph shows the altitude and body angle overtime of a bird in bounding flight with the corresponding flapping or gliding mode [19].

1.2.2 Current Unmanned Aerial Vehicle Flight Time Extension Methods

There are two main approaches to extending UAV flight time and distance. The first focuses on improving the battery's chemical composition, capacity, charging methods or integration. The second utilizes aerodynamic behavior or atmospheric phenomena to harvest flight energy. The research discussed in [4, 24, 25] is an example of battery integration research in which solar panels and

flexible batteries were integrated into the wing design of a FWUAV. This configuration allowed for solar energy capture and storage, thus prolonging the flight time. Another approach to this method was the use of wireless charging to increase the battery life during flight [26]. Furthermore, there are advances in the chemical capacity and weight of batteries. In [27], a battery was presented which could increase its discharge time through a self-charging material layer and was also lightweight and flexible. Even though these, and other advancements have been made, there still exist the major disadvantage of available chemical technology.

Static and dynamic soaring, intermittent gliding, and wind gliding are all nature-inspired methods of harvesting energy that have been implemented in UAV's to improve flight time. The main advantage of this second method is the achievable flight time increase on existing platforms without the need to improve the battery itself. Furthermore, there is the potential for method-centric design or the tailoring of platforms to the chosen energy harvesting method.

Fixed-Wing Aircraft

The majority of research in this second category is accomplished using fixed-wing UAVs of both powered and glider configurations. The choice of fixed-wing aircraft for static and dynamic soaring implementation lies in their advantageous design. In this research sphere, the vast majority of foundational work and control design has been accomplished using simulations [28, 29, 30, 31].

Dynamic soaring can be defined as the use of wind shear, caused by changes in atmospheric wind speed, to increase flight energy [32]. The success of a dynamic soaring, fight path is determined by the maximized ratio of potential energy extracted from the atmosphere while climbing into an increasing wind gradient and kinetic energy utilized while descending out of it [32]. An effective flight path capitalizes on the wind gradient profile by such parameters as angle of attack, banking angle, and angle of descent. For this reason, in Bonin [28] researchers represented the most energy efficient flight path as an optimization problem. A given initial to final energy ratio was maximized subject to constraints such as a range of flight path angles, banking angles and the equations of motion. Similar path optimization research was conducted in [29, 30, 31] where best

path was based upon the exploitation of wind gradients and the maximization of extracted energy from the atmosphere. A morphing, wing strategy, with variable wing span and sweep, has also been shown to affect dynamic soaring as shown in [33].

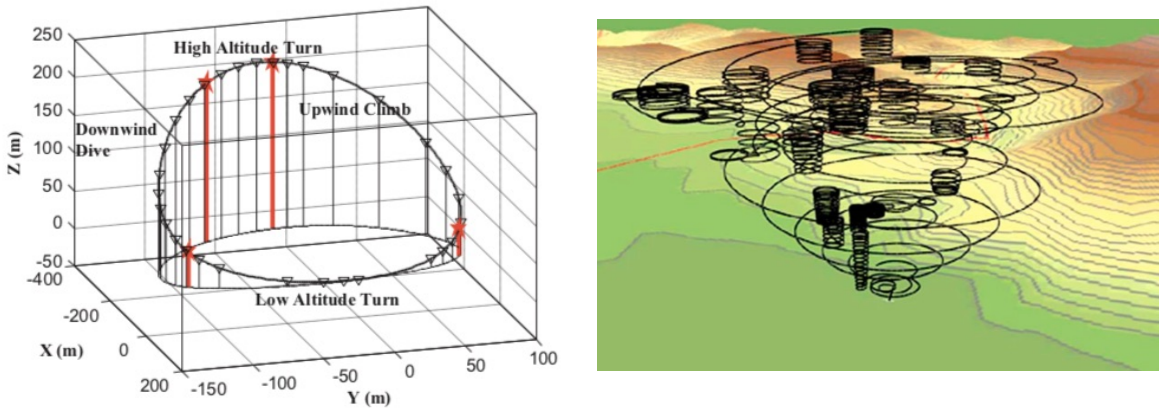


Figure 1.2: Comparison of (a) dynamic soaring flight path simulation showing the stages of a dynamic soaring path [34] vs. (b) static soaring flight path showing the use of up drafts for flight paths [35]

The natural atmosphere can be unpredictable and wind gradients are subject to change overtime. Therefore, simulations have been developed to demonstrate the active sensing of wind speed, direction and profile as useful methods to maintain an effective dynamic soaring path. Tools such as deep neural networks and trajectory parameterization have been used in simulated environments to create an optimized flight path in natural, unpredictable conditions [36]. As simulations improve in accuracy, the testing of optimized flight paths as a method of improving flight becomes possible. Testing optimized flight paths on a more accurate simulated environment is another method of improving outcomes. Special attention has been given to improving simulated wind shear and flow patterns using in flight data [30]. Furthermore, computationally simple guidance strategies have been presented to increase the computational speed of optimal flight path generation [34].

Due to the difficulty of autonomously locating the wind shear conditions necessary for dynamic soaring and because the control of UAVs in dynamic soaring flight paths is easily perturbed, there are very few examples of real-world dynamic soaring implementation [32]. There are cur-

rently no examples of autonomous dynamic soaring in UAVs. However, the work conducted by Boslough [37] is a rare example of successful, radio-controlled, dynamic soaring flight implementation. Firstly, to prepare for the flight, Boslough used a genetic algorithm to analyze and optimize potential dynamic soaring paths in simulation [37]. Using a series of combined simulation systems and packages a 6 DOF flight simulator was developed, that contained a very realistic atmospheric, geodesic and gravitational environment [38]. In further preparation for radio-controlled flight test, the feasibility and effectiveness of the optimized flight paths were analyzed in this simulator. Finally, the researchers were able to use the information gained through simulation to successfully implement human-controlled, dynamic soaring on foam UAV sailplanes [37, 38].

Static soaring can be defined as the use of thermals, which are atmospheric temperature gradients generating an updraft of air, to maintain flight or gain altitude without increasing energy expenditure [13, 32]. Thermals have been used by manned planes and hang gliders for a long time to maintain and extend flight [32, 35], but the design of a UAV system capable of advantageously using static soaring techniques requires a scientific understanding of static soaring principles [39, 35, 40]. For example, the optimization of a static soaring flight path, the nature of thermals and the ability to predict or sense the presence of a thermal are all necessary when designing such a system [32, 40, 41, 42, 43].

Research has shown that static soaring success is determined by both the maintenance of an updraft enabled, elliptical, flight path that maximizes lift and minimizes sink, and the ability to recognize and act on ever-changing conditions favorable to thermals [13, 32, 35, 39, 40, 43]. Natural flyers tend to discover thermals visually, tactilely, and through the observance of other natural flyers [13, 32]. Furthermore, the maintenance of a successful soaring path tends to rely heavily on the weight, wing shape and flight behavior of the individual bird [32]. Therefore, thermal utilizing UAVs have often implemented methods similar to and inspired by natural ones.

Foundational work in creating thermal utilizing UAVs often begins in simulations that characterize the atmospheric environment and test the implementation of static soaring strategies. For example, in Stole [43] a vision-based, time-sensitive model of sub-cumulous, thermal positioning

and vanish time was presented as a simulated method of thermal recognition and utilization. Static soaring simulations have also experimented with thermal sensing using nature-inspired flight patterns. Cheng and Langelaan [42] utilized multiple UAVs in a cooperative flight pattern to discover and track thermals. The cooperative flight patterns were generated and evaluated using a Monte Carlo experiment according to the parameters of flock sizes, topographical exploration, and different starting altitudes. In the work presented by Allen [35], different spiral searching patterns were simulated for optimal searching path.

Static soaring techniques have been successfully demonstrated on UAVs in flight. AutoSoar is an energy-estimation algorithm that has been successfully demonstrated on a powered fixed-wing UAV [44]. Using AutoSoar, the platform was able to autonomously map, explore and exploit thermals. A similar system, the Autonomous Location of Thermals (ALOFT) craft, used geo-location to locate thermals and a centroid, adaptive grid method to utilize them [39]. Energy state estimation is another method for finding a thermal position [41]. While in a thermal, an autonomous UAV needs to maintain a centered path in order to maintain flight. Therefore in Andersson [45], a thermal centering controller was used to maintain an optimal flight path. Finally, in Cobanoan [6], RRT path planning algorithm was used to control a multi UAV search and utilization of thermals.



Figure 1.3: Examples of fixed-wing UAVs used in autonomous soaring experiments (a) A powered fixed-wing glider used at Dryden Airforce base [41] (b) The ALOFT glider UAV used in flight experiments [39]

Intermittent gliding can be defined as the cycling of a thrust generating, power cycle (i.e using propellers, servo motors, etc.) with a lift-controlled glide cycle [46]. The success of an intermittent flight depends upon the amount of usable kinetic energy generated during the power cycle, the gliding efficiency of the UAV design and the ability to use incident wind currents [13]. Fixed-wing UAVs have the potential to utilize intermittent gliding through the harvesting of differential wing or gust energy [47]. Similar to dynamic and soaring conditions, differential wind vectors can be created via instantaneous thermal variations in the atmosphere, or through directional wind shear [5, 47]. However, conditions that produce wind gusts or turbulence can often be shorter in duration

and with a greater special variance than conditions seen in soaring [48]. Therefore, any flight path designed to successfully utilize wing gusts will be one that advantageously utilizes their constantly changing temporal and spatial aspects [5, 48, 47].

The author was unable to find research showing successful intermittent gliding or gust energy harvesting flight implementation in fixed-wing UAVs. However, there are a few examples of simulations demonstrating the feasibility of this energy harvesting modality. Patel [5] made the observation that a UAVs instantaneous change in coefficient of lift due to a wind gust could be used as a control law to improve the recognition and utilization of favorable wind paths. He demonstrated this concept in a simulation that used the Dryden power spectral density function to produce realistic wing turbulence [5]. Furthermore, the simulations conducted by Langelaan and Gavrilovic [47, 48] showed that trajectory optimization might be modeled as an energy transfer function. The goal of each optimization strategy was to maximize the amount of energy transferred to the craft from the wind gust through certain maneuvers or flight paths.

Flapping-Wing UAVs

Flapping wing UAVs (FWUAVS) are bio-inspired platforms that generate lift and thrust through the cyclical, flapping motion of wings. They are not a new concept, as Leonardo DaVinci produced some of the first drawings of flapping-wing flying machines [9, 8]. The greatest advantages of FWUAVs is the combined efficiency and maneuverability of its flight, as well as the added benefit of operating in Reynolds numbers where fixed-wing performance decreases [25, 49]. Furthermore, it is a type of UAV that is capable of switching between aerodynamic flying regimes and adapting its flight modality to fit in-the-moment environments. While other platforms will always behave like a fixed wing craft, or a rotary craft, a FWUAV has the potential to switch between flight behaviors that utilize the advantages of both.

FWUAV platforms fall into the two categories of meso-scale and micro-scale sizes. Meso-scale platforms are often inspired by birds or bats and maintain similar size scales. Onboard motors produce the flapping actuation through gears or drive systems. Many examples of this type of

UAV exist. Batbot is a bat-inspired platform engineered by researchers at the University of Illinois-Urbana Champlain and features a novel drive system for articulated limbs covered by a skin-like film [50]. Early versions of this platform mimicked the nuanced bat flapping behavior in a tethered environment. However, further improvements allowed for untethered flight in a motion-capture environment [50, 51]. Similarly the Delfly platform, created by researchers at the Delft University of Technology, created a FWUAV with four primary wings that could fly and hover like a fly [52, 53, 54]. Researchers created a design of iteratively smaller sizes that utilized passive peal and clap phases of outward and inward wing stroking to generate life and thrust [52, 53]. Further iteration achieved autonomous untethered flight in a motion capture arena [54, 55]. Finally, RoboRaven was the first servo-driven FWUAV with independent wing control and has the ability to perform prolonged untethered flight [56, 57]. This platform will be discussed in more detail later in this chapter.

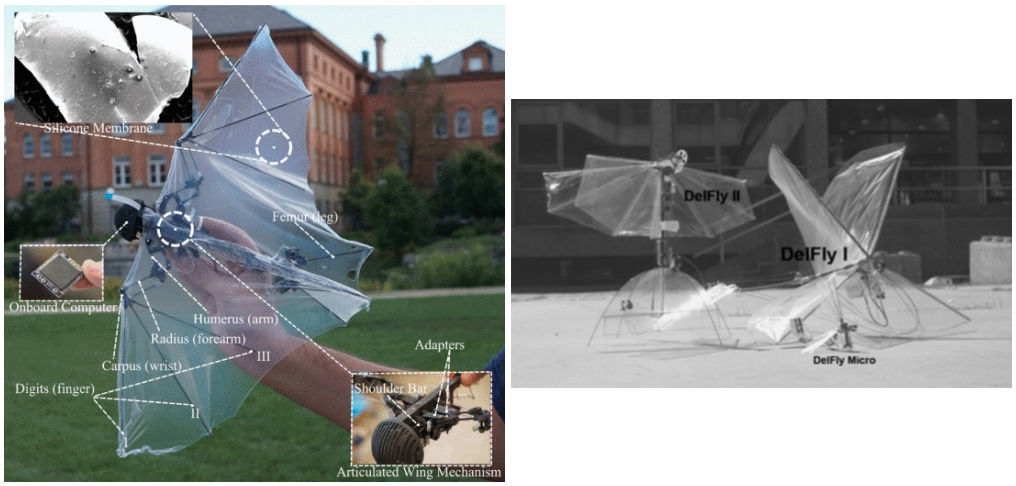


Figure 1.4: Flapping flight platforms (a) BatBot [58], and (b) Delfly [53, 59]

The greatest difference between meso-scale and micro-scale UAVs besides their overall size, are the actuation methods by which they generate flapping flight. Scaling down the size of a platform will invariably change the effect of all relevant physical forces. For example, while the electromagnetic forces generated in the windings of a dc or servo motor do not very much affect the behavior of a large platform, such forces become very large at the sub-micro scale and can

effectively hinder the platform's functionality [60]. Therefore, novel actuation methods were developed to produce flapping flight in smaller-scale platforms [3, 61]. Manufacturing techniques also had to be tailored to this scale. Sterolithography and fusion deposition are examples of manufacturing methods used to produce platforms on this scale. Material folding techniques have also been explored for platform assembly [62].

RoboBee is a well-known and prolific series of sub-micro UAV platforms developed by researchers at Harvard University [63, 64]. RoboBee is unique in that it was the first micro-scale UAV platform to take off vertically. Overtime, the vertical takeoff capabilities of the platform improved. Whereas, the first iteration was only able to take off using guide wires [63], the final design included parts for stabilization during takeoff and landing [65]. Future designs featured integral, flexible circuitry that made on board, closed-loop control possible. To create RoboBee a novel microfabrication methodology called Smart Composite Microstructures was developed [60]. Further scientific contributions include, the use of folding parts for assembly and a novel piezo-electric transmission system for flapping actuation [60].

In contrast to RoboBee, the dragonfly platform from Harvard University was designed to actuate via a very small DC motor and was not designed for vertical takeoff, but rather for flight energetics testing [62]. It also features more onboard electronics, such as an IMU board, further sensor arrays, and wireless antennae, and therefore had a more capable controls system from its inception. However, like RoboBee, it currently has no independent wing control [62]. Testing was done on aerodynamic flight performance. It was accomplished using a low-speed wing tunnel and motion capture arena.

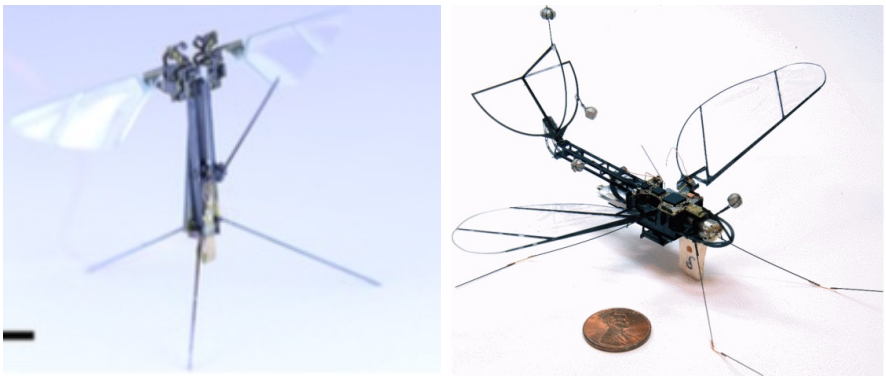


Figure 1.5: Examples of Micro-Scale UAVs (a) RoboBee [3] (b) Harvard Robot Moth [66]

As was stated before, there is limited demonstration of bio-inspired flight extension strategies in FWUAVs. There are currently little to no examples of soaring demonstration on flapping-wing UAVs. However, a recent publication by Delft University of Technology demonstrated a version of Delfly that could steer into wind gusts as a potential flight strategy [67]. There are also simulated examples of intermittent gliding and sinusoidal bounding flight. Simulations exist that show that sinusoidal, oscillating flap-gliding flight can improve the efficiency of flight in FWUAVs [68]. Furthermore, platforms such as those represented in [69] have demonstrated in flight flapping-gliding behaviors. Finally, though it is not strictly a gliding behavior, RoboRaven was able to demonstrate in flight, autonomous, altitude-based, flap-dive flying [70].

1.2.3 Introduction to Phugoid Dynamic Modeling

Modeling a UAV's flight path has been undertaken using various methods. The phugoid mode is a lightly-damped, low oscillation mode that can be used to represent the long-term translation behavior of a flight vehicle's center of gravity [71, 72]. It arises from an examination of the aircraft's equations of motion in the longitudinal plane and can be used to understand a plane's pitching, gliding, and flight path [72, 73]. The first notable representation and approximation of the phugoid mode was completed by Lanchester in his 1908 work titled "Aerodonetics." [71, 72, 74]. In this work fundamental equations for phugoid flight path and radius of curvature were

developed and demonstrated through experimentation. The phugoid mode has been adapted to approximate the flight path of almost every type of aircraft including fixed-wing, flapping-wing and hypersonic vehicles [73]. The approximation methods themselves continue to improve in accuracy and usability [71, 75].

1.2.4 Introduction to Battery Dynamics Modeling

Electrically powered, and more specifically battery powered, UAVs comprise the majority of the current state-of-the-art technology. A battery at its core is an electrochemical energy storage device that supplies voltage and current to electrical systems. In a UAV system, a battery's charge and discharge profiles are directly related to a UAV's flight time, distance and the efficiency of its propulsion and control mechanisms. Thus, any complete understanding of a UAV's flight performance must include a model of the on board battery.

Modeling a battery's charging and discharging behavior can be a complicated process depending upon the type of battery and which aspects of the battery most affect the current UAV application. Each approach to battery modeling was developed to characterize fundamental aspects of battery composition in a way that would allow for the design, analysis and prediction of charge and discharge specific to the application [76, 77]. At their core, most modeling approaches are interested in characterizing a battery's voltage, current and power discharge and charge parameters. However, to fully understand these parameters, elements such as the battery's state-of-charge (SOC), the ratio of current available charge to battery capacity, the state-of-health (SOH), the degradation of a battery's internal composition overtime, and the internal resistance are also important [78, 79, 80, 81]. Finally, when analyzing the full usefulness or efficiency of a battery, internal thermodynamics, heat transfer and internal chemistry might also be important.

Choice of battery model is dependent upon its suitability for the current application [81, 82]. Depending upon the application, each model varies in accuracy, complexity, usability and even processing requirements. For example, electrochemical models are the some of the most complex and accurate models. They characterize both the "macroscopic" variables such as voltage, and the

"microscopic" variables such as internal temperature [76]. These models are often best used for the design of a battery or battery system [81]. Kinetic battery models represent a battery's discharge behavior as a change of height, characterized by a differential equation and are best used for modeling the discharge profile of large lead-acid batteries [76]. Mathematical and analytical models are often used for the prediction of battery behavior and often require experimental validation [81]. They can be based on statistical methods such as Bayesian analysis [83, 84] or more complex methods such as machine learning [85]. Finally, equivalent circuit models represent a battery's internal properties as corresponding circuit elements. These types of models can range from highly complex to simple and are easily adaptable to battery type and application [82, 86, 87, 77]. They are often best used for real-time system control and battery discharge tracking [81]. Often developers combine different battery model types to characterize complex systems [76, 81]. For instance, the characterization of a complex UAV battery system might include the use of equivalent circuit models for real-time SOC tracking and a thermal model to understand the efficiency of the battery in terms of amount of energy lost to heat [81].

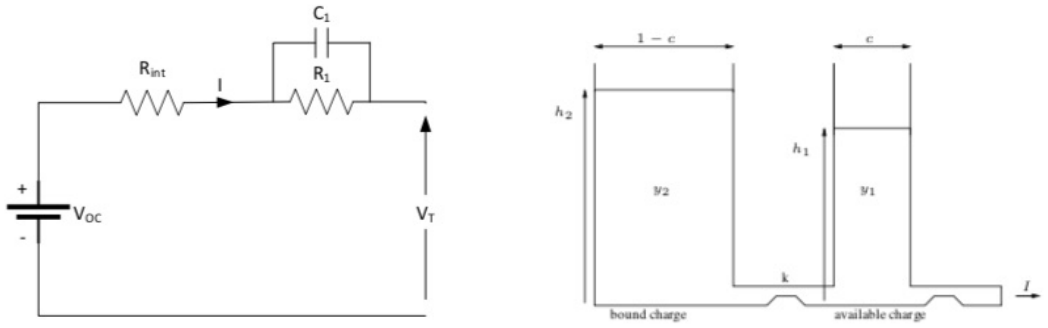


Figure 1.6: Pictorial examples of battery models (a) A 1st order Thevenin equivalent equivalent circuit model [81] (b) A two-well, kinetic battery model [76]

Battery models have been used in the development and characterization of UAV energy utilization and power dynamics [83, 84, 85, 88, 89]. Analytical models appear to be the most common method used for the prediction of UAV flight endurance. For example, in a series of publications Saha [83], utilized Bayesian analysis to predict the onboard battery's "remaining useful life

(RUL)", which is a critical parameter of flight endurance characterizing the remaining time before the battery fails to provide sufficient power [83, 90]. Further research improved this method by using an RC equivalent circuit model and logarithmic functions to analyze the battery's internal chemistry and track discharge rate [84]. The result was an optimization of battery life based upon a particle filtering framework [84]. As was stated above, because analytical models are most often used for prediction, they are best understood when coupled with experimental data. Many examples exist of combining analytical models with wind tunnel [89, 91] and flight experiments [88].

The use of equivalent circuit models in UAV battery modeling is well documented [92, 93, 94, 95]. Previous research has demonstrated successful use of simple 1st and 2nd order RC circuits [92, 94] and more complex combined systems [93, 95].

1.2.5 RoboRaven Platform Review

Robo Raven is a series of FWUAV platforms designed and developed by students and faculty at the University of Maryland-College Park. Six unique versions of this platform have been developed over time. The original design, Robo Raven v.1, was based on the biological flight patterns and size of the raven bird [56, 95]. It was the first FWUAV with "independent wing control", which is the ability to decouple the actuation of each primary wing from one another [56, 57]. Flight behavior and control of the craft increased in performance because of this feature. Acrobatic maneuvers, such as flips and rolls were also made possible [56]. Finally, this version developed the foundational Robo Raven design features, which were used throughout the other versions. These features included servo motor choice, required flapping frequency and wing design parameters and manufacturing methods [95].

Robo Raven v.2 was used for wing parameterization studies in which wings of various sizes and layouts were tested for their thrust and lift generation [57, 95]. A design space was created in which flapping frequency and wing size were directly correlated with flight performance and potential payload [57, 95]. This platform was also the first to utilize an on board sensor system

that measured flight speed, battery voltage, altitude and position [96].

Robo Raven v.3 was the first FWUAV that successfully charged on board batteries through embedded solar panels in the wings [4, 25, 97]. Potential solar panels were tested and chosen based on both their battery charging efficiency and ability to flex with the flapping wings [25]. This work displayed the first instance of multifunctional wing design as a variety of wings were developed and tested based upon their ability to increase solar panel coverage and also improve flight performance through strategic wing stiffening [25, 97]. Finally, with additional solar panels on the tail and platform body, the solar panels were able to supply 64% more power to the system and improve flight times by over 27 seconds [25, 97].

Further improvements in the platform, in the form of Robo Raven v.4, created the first semi-autonomous Robo Raven platform, capable of autonomous loitering and diving [70, 98]. Robo Raven v.5 was the first version of Robo Raven to be a propellor-driven, mixed-model FWUAV [49, 99]. Rear motors provided an additional thrust that increased platform flight speed and payload capacity. It also allowed for improved acrobatic capabilities and increased flight ceiling. Finally, Robo Raven v.6 expanded on the use of multifunctional, charging wings to include the integration of flexible batteries for further improvement in flight time [24].



Figure 1.7: Examples of the Robo Raven platform (a) Robo Raven 1 [56] (b) Robo Raven 3 [4, 25, 97] (c) Robo Raven 5 [49, 99]

1.3 Technical Approach

This work presents a method for the exploration of intermittent gliding strategies to improve the flight duration and battery endurance of the flapping/gliding FWUAV, Robo Raven1. The method described in this work began with the development of a mathematical model and simulation to analyze the effects of intermittent gliding on flight performance. The modeling process included the design of a state-space representation that directly related the aerodynamic behavior of the FWUAV to its onboard battery discharge profile. The aerodynamic behavior was represented by a novel, modified phugoid equation that added a term representing the thrust of the platform generated when flapping. A modified equivalent circuit model was used to characterize the onboard lithium-polymer battery. The simulation, developed using MATLAB, made the novel assumption that the coefficient of lift when gliding ($C_{L,glide}$) was different from the coefficient of lift when flapping ($C_{L,flap}$). Furthermore, the aerodynamic and battery variables were chosen based upon the characteristics of the Robo Raven 1 platform. The state-space model was used to compare and analyze the statistical performance of three intermittent gliding strategies that were configured by duty cycle, altitude and voltage level.

Use of the method proceeded through the development of a design space relating the design of wing planform to the flight analysis of glide performance. Creation of the design space included the parameterization of three wing planform specimens chosen because of previous research and theoretical effect on gliding behavior. The Robo Raven1 platform was modified to include a sensor suite capable of measuring the aerodynamic parameters outlined in the MATLAB simulation. Each wing was tested in an experiment designed to isolate the gliding performance. Real-world aerodynamic ratios were extracted and analyzed.

The method was finalized via the flight analysis of intermittent gliding (hybrid flap/glide) effect on flight performance. To accomplish this goal, the Robo Raven 1 platform was further modified to include voltage sensing capabilities. The platform was then used in intermittent gliding flight demonstrations to test the viability and performance of real-world hybrid flight strategies. The

statistical performance of the tested intermittent gliding techniques was extracted and compared to the performance of a continuously flapping flight. Finally, the real-world flapping and gliding aerodynamic ratios for this platform were extracted and analyzed. They were then used to further develop the chapter 3 simulation to a more correct characterization of hybrid flap/glide flight behavior.

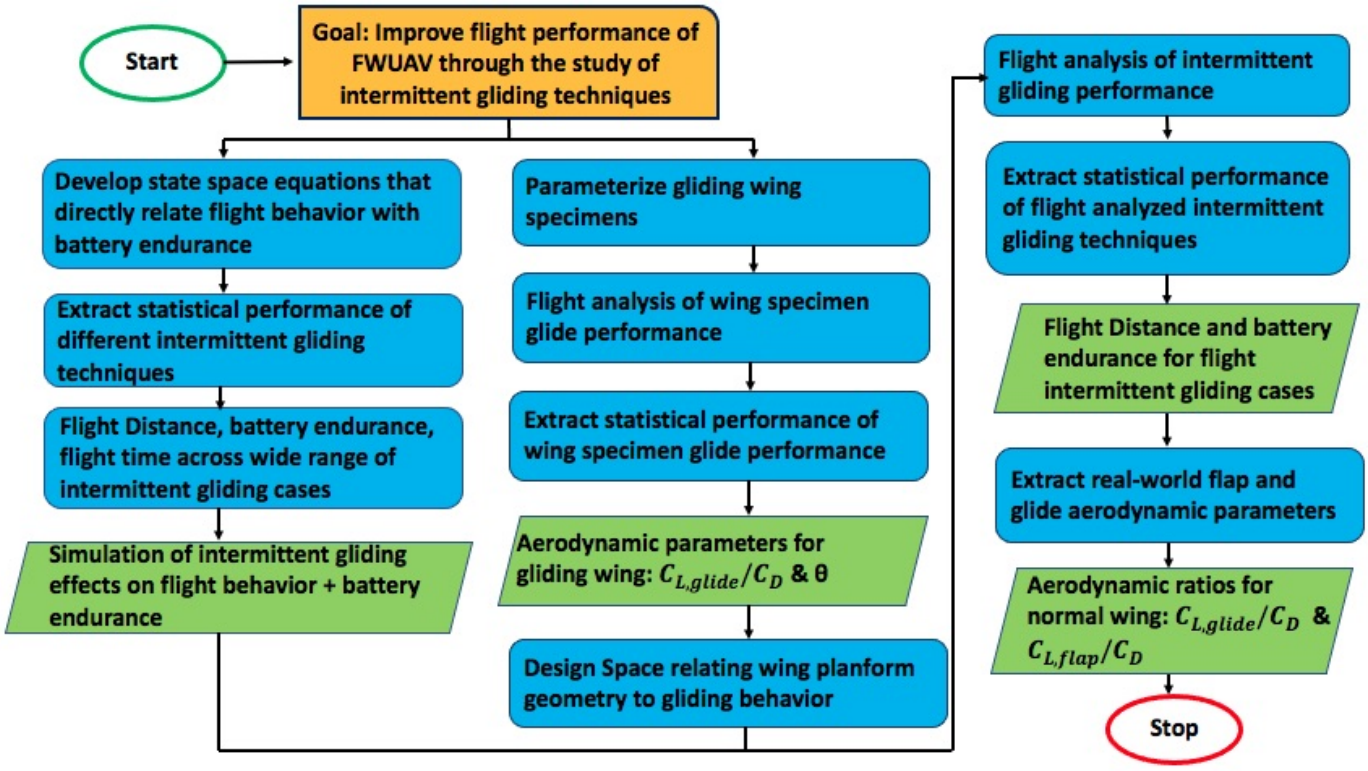


Figure 1.8: Flow diagram representing the technical approach of this dissertation

1.4 Contributions of Dissertation

The scientific and technical contributions of chapter 3 are as follows. First, a novel, adaptable, and expandable state-space model was developed that directly related the aerodynamic performance of a flapping-wing UAV to its onboard battery dynamics. The second contribution was the identification of a fundamental hybrid flap/glide principle, unique to flapping-wing UAVs; namely, the assumed inequality of the coefficient of lift during gliding ($C_{L,glide}$) and the coefficient of lift when flapping ($C_{L,flap}$) due to the quasi-steady state dynamics of flapping vehicles. This identified prin-

ciple informed the utilization of the state-space model in a simulation. The third contribution was the development of a simplified method, using the simulation, that allowed for the identification and characterization of performance metrics for hybrid flap/glide design. The final contribution was the analysis of three hybrid flap/glide methods, generally applicable to other UAV platforms, that were shown to be effective in improving flight time. The contributions of this chapter developed a simulation by which future UAV platforms can be evaluated according to the relationship between their aerodynamic performance and battery behavior. Furthermore, hybrid flight methods might be designed and evaluated using this technique. Finally, the scientific understanding of hybrid flight mechanics was expanded through the identification of the unequal flap/glide C_L/C_D ratio principle.

The contributions of chapter 4 are as follows. First, it was demonstrated in this chapter that the wing planform design of a flapping-wing vehicle could be tuned to a preferred gliding behavior. The second contribution was the identification and analysis of real-world effectiveness of hybrid flapping/gliding through the characterization of gliding cycle performance according to wing planform design. The final contribution was the observation and explanation of wing flexion effects on gliding performance according to the fundamental science laid out in previous research. The contributions of this chapter laid out a foundational understanding of wing geometry and flexion effects on FWUAV gliding performance and created a method by which future FWUAV wings designs might be characterized.

The contributions of chapter 5 are as follows: First, a foundational flight analysis was developed and utilized to test the feasibility of hybrid flapping/gliding implementation on a flight vehicle and validate the state-space model. The second contribution was the development of a method to evaluate the improvement of hybrid flight over continuously flapping flight. Furthermore the third contribution was the development of a method to experimentally validate the fundamental hybrid flap/glide principle dictating that the ratio of $C_{L,glide}/C_D$ was not equal to $C_{L,flap}/C_D$. The final results of this analysis proved the fundamental principle and returned ratio values more correct to the Robo Raven platform. The final contribution of this chapter was the development of a more

realistic simulation using the experimental values and more correct aerodynamic calculations. The contributions of this chapter laid a foundational method for the flight analysis of hybrid flap/glide techniques. Furthermore, it created a means by which the hybrid flap/glide simulation might be tuned to the behavior of real-world unmanned aircraft.

1.5 Outline of the Dissertation

Chapter 2 presents the mathematical and scientific background important to the technical approach of this work. It will present phugoid and equivalent circuit theory as well as a technical review of the Robo Raven1 platform. Chapter 3 presents the development of the state-space model through the modification of the phugoid and equivalent circuit theories and the addition of a servo motor, circuit model. It will also discuss the results of the intermittent gliding simulation. Chapter 4 presents the scientific background behind the development of a FWUAV wing planform design space based upon intermittent gliding potential. It will discuss the development of the wing designs and the subsequent results of the flight analysis. Chapter 5 details the re-development of the Robo Raven1 platform into an FWUAV capable of manual intermittent flight and the in flight sensing of the performance parameters. Furthermore, it will show the results for the in flight intermittent gliding demonstrations. Chapter 6 concludes the work with a discussion of the overall results, future research and scientific contribution of this work.

CHAPTER 2
TECHNICAL BACKGROUND

This chapter will present the fundamental mathematic and scientific principles that govern the research presented in this work. It will discuss phugoid dynamics and modeling and the means by which a state space representation of longitudinal dynamics is formulated. Furthermore, the fundamentals of equivalent circuit modeling will be discussed. Finally, an in depth overview of the Robo Raven1 platform, including a list of components, fuselage and wing design, and past research will be presented.

2.1 Phugoid Dynamics and Modeling

Phugoid model characterization begins with a point-mass representation of the aircraft. When developing a point-mass model it is assumed that the evaluated body is rigid and there is no internal torque or compliance of members. While this is inherently valid for fixed or rotary-wing aircraft, FWUAV's often contain components, such as wings or tails, that are highly flexible. This problem is resolved by utilizing the flat plate model and representing compliant wings and tails as rigid structures. The use of this method was demonstrated in previous work [70, 95, 98].

The characterized body is presented in a 2D plane. The platform's body frame has its origin at its center of gravity, G, and has principal axes, $\hat{b}_1, \hat{b}_2$. In keeping with aerodynamic tradition, the platform's velocity, ν, and drag vectors are opposite each other along the $\hat{b}_1$ vector line. The platform's lift vector points along the $\hat{b}_2$ axis, tangential to the platform's drag vector. The world frame is represented by the principal axes $\hat{e}_1, \hat{e}_2$. The weight vector follows along the $\hat{e}_2$ axis. Finally, the angle, θ, represents the platform's flight path angle. The final model can be seen in the figure below.

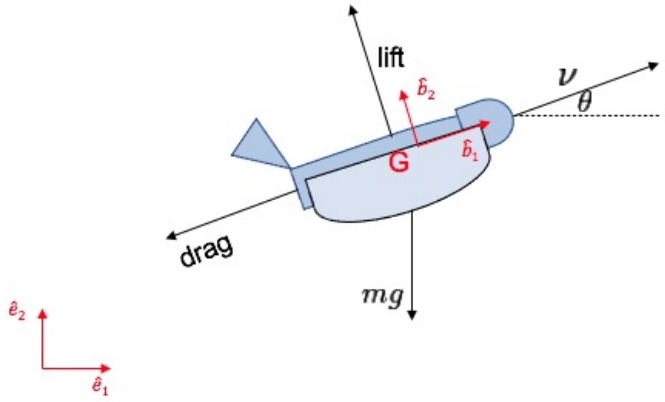


Figure 2.1: The forces and coordinates of the phugoid dynamics, after [75]. The $\hat{e}_1, \hat{e}_2$ coordinates represent the world frame and the $\hat{b}_1, \hat{b}_2$ represent the platform frame at the center of gravity

Applying Newton's second law yields the following mathematical representation.

$$-mg\hat{e}_2 - F_{drag}\hat{b}_1 + F_{lift}\hat{b}_2 = m(\dot{\nu}\hat{b}_1 + \nu\dot{\theta}\hat{b}_2) \tag{2.1}$$

This equation can be further simplified into a state space representation by separating the equation into the principal $\hat{b}_1, \hat{b}_2$ components. This yields the following.

$$m\dot{\nu} = -mg\sin\theta - F_{drag} \tag{2.2}$$

$$m\nu\dot{\theta} = -mg\cos\theta + F_{lift}. \tag{2.3}$$

Assuming quadratic models for lift and drag yields the final state space equations seen below, where $C'_{L,glide}$ and C'_D represent the lift and drag coefficient variables respectively, during gliding [73, 46]. The variables $C'_{L,glide}$ and C'_D can be seen in equation 2.6 – 2.7.

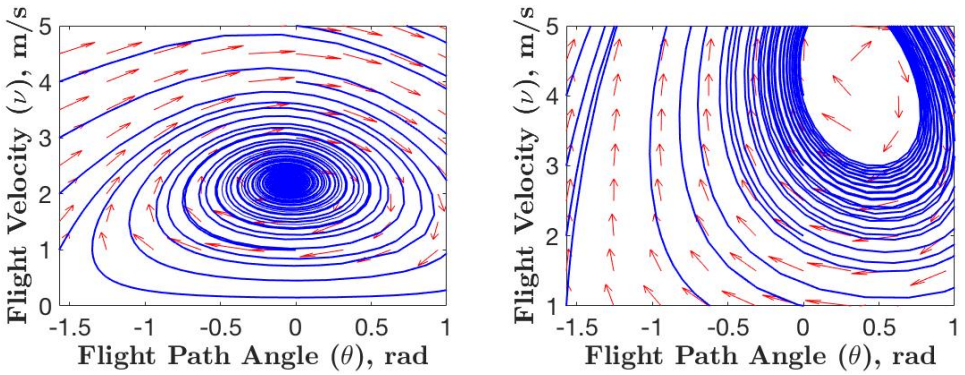
$$\dot{\nu} = -g\sin\theta - C'_D\nu^2 \tag{2.4}$$

$$\dot{\theta} = \frac{-g\cos\theta + C'_{L,glide}\nu^2}{\nu} \tag{2.5}$$

$$C'_D = \frac{1}{2m}\rho A_w C_D \tag{2.6}$$

$$C'_{L,glide} = \frac{1}{2m}\rho A_w C_{L,glide} \tag{2.7}$$

Reducing the coefficient variables to their simplified form, it is clear that the ratio of $C'_{L,glide}/C'_D$ equals the $C_{L,glide}/C_D$ ratio. It is important to note that the ratio of $C_{L,glide}$ to C_D greatly affects the flight performance of the vehicle. It can determine the stability and flight distance of the vehicle. The graphical study shown below demonstrated the importance of this ratio.



(a) (b)

Figure 2.2: Phase portraits of (a) gliding phugoid dynamics with $C_{L,glide}/C_D = 20$; (b) flapping phugoid dynamics with $C_{L,flap}/C_D = 5$

2.2 Battery Dynamics and Modeling

As stated before, equivalent circuit models represent a battery's characteristic elements as electrical circuit components. The ease of use and adaptability of these models make them ideal for characterizing batteries that are integral system components. They have been used widely in characterizing the behavior of UAV batteries and their effect on overall system behavior [95, 100].

The most basic equivalent circuit model represents a battery as the simple Thevenin Equivalent circuit shown in Fig. 2.3. The resistor, R_{bat}, represents a battery's internal resistance that impedes the flow of current from the electrolyte to the external load. The battery's internal resistant is in-

tegral to understanding parameters such as the state-of-health (SOH) of a battery, which degrades overtime in correlation with an increase in internal resistance. It also greatly affects battery elements such as its current, I_{bat} and SOC. The voltage source in the circuit represents the battery's open circuit voltage (VOC). Finally, the voltage across the open leads represents the voltage in the battery that is supplied to the load, V_{bat}. A battery's VOC varies from equaling V_{bat} when no load is applied to being related to V_{bat} as a function of the current I_{bat} when the battery is discharging. Solving this circuit, assuming discharging behavior, produces the following mathematical representation.

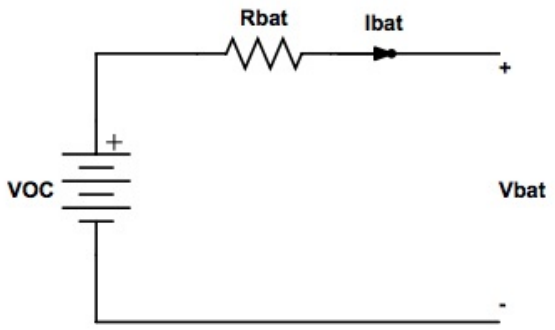


Figure 2.3: The equivalent circuit model for battery discharge
[81]

$$V_{bat} = VOC - I_{Bat}R_{bat} \tag{2.8}$$

The accuracy of this simple model is improved when the battery's state-of-charge is integrated into the mathematical formula. A battery's state of charge (SOC) is the percentage of available charge within the battery at any given time. It is a direct measurement of battery charging and discharging behavior and can be used to more accurately represent elements such as VOC and R_{bat}. In a simple situation, it is possible to directly equate VOC with SOC. However, increased accuracy can be achieved by characterizing VOC as a non-linear, exponential, and even polynomial function of SOC.

Calculating SOC accurately is therefore important to completing a battery's characterization.

At the most basic level, SOC is the ratio of the battery capacity at any time step, Q(t), over the battery's overall capacity (Q_{bat}). However, tracking the change in this ratio overtime can require more complicated methods. Following the framework outlined in [87], it is possible to organize SOC estimation methods into four categories. First, direct measurement methods experimentally obtain the variables necessary to mathematically characterize SOC [95, 86]. These methods allow for the model to be adapted to specific batteries and has been used in previous work to characterize a FWUAV battery system [95]. However, they often require experimental setups that take time to develop. Next, book-keeping methods characterize the SOC using I_{bat} data as a continual input to update the model. The column counting method is a widely used example [95, 86]. Finally, there are adaptive system methods, such as neural network and vector machine models, and hybrid methods which create a framework by combining other methods.

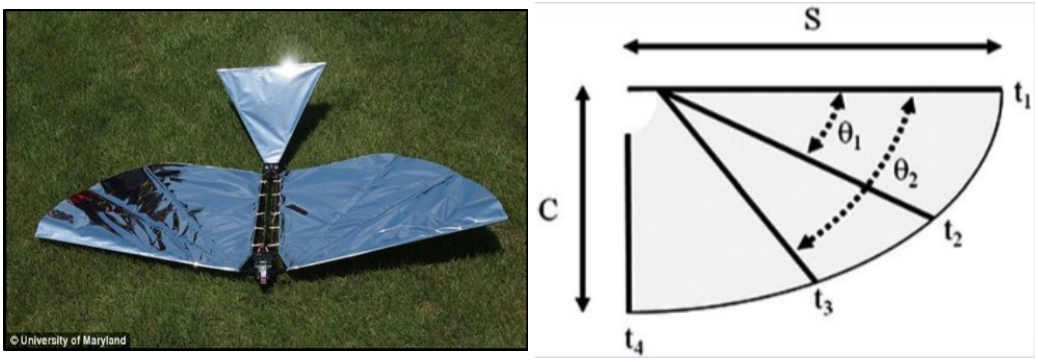
The column counting method tracks the change in SOC overtime via a summation or integration function of I_{bat} and Q_{bat} [87]. The equation below is a version that uses integration to track the SOC. The equation tracks the SOC from 100% charge (SOC(0)) to a completely drained state.

$$SOC(t) = SOC(0) - \int_0^t \frac{I_{bat}(\tau)}{Q_{bat}} d\tau. \tag{2.9}$$

2.3 RoboRaven Platform Review

The Robo Raven 1 (RR1) platform was designed to be a lightweight, durable platform capable of sustained, untethered flapping flight [57]. The main fuselage needed to both contain the large vibrations produced during flapping and provide a stable structure to hold actuators and electrical components. To that end, the fuselage structure was composed of flexible ¼" thick carbon fiber rods, and stiffening, lightweight Delrin©pieces. The wings and tail are highly-compliant, membrane-style actuators. The wing's span and chord are given structural stiffness via a combination of carbon fiber rods. The wing's flexible structure is made by a less than .0001 inch thick piece of Mylar. The wing's design and parameters can be seen in the figure and table below. The wing's lightweight construction allows it to deform during upstroke and downstroke, creating an

"induced airfoil" that aids in the platform's production of lift ans thrust [56]. The front of RR1 is accentuated by a beak-like, Delrin©cap that protects the servo motors in the event of a crash.



(a) (b)

Figure 2.4: (a)The RoboRaven 1 platform developed at the University of Maryland [99] (b) A diagram of the RoboRaven1 100% wing [49, 95, 4]

State	Units	Value
t_1	inches	0.125
t_2	inches	0.059
t_3	inches	0.059
t_4	inches	0.064
θ_1	degrees	20.5
θ_2	degrees	43
$Span$	inches	20.75
$Chord$	inches	12.25
$Area$	inches sq.	254.2
$Mass$	grams	12.7

Table 2.1: RoboRaven1 Wing Parameters

RoboRaven1's flapping motion is generated by two front-facing, metal gear Futaba S9373SV digital servos. These S-Bus servo motors provide between 1hz and 4hz of flapping frequency and a 100°total flapping angle via a rated 341.7 oz.in of torque at 7.4 V. A designed servo horn allows the servo to attach and actuate the Robo Raven wing. The dedication of each servo to flapping only one wing allows for independent wing control, or the ability to control each wing separately. The platform is steered largely by the rear tail that is controlled by a smaller DS 188HV servo motor. This servo is able to turn the tail at a rated 13.1 oz/in of torque and speed of .06 sec/60 °at 7.4

V. All of the servo motors, and other onboard electronics, are controlled by an Atmega328 chip, Arduino Nano microcontroller. The microcontroller receives commands via a Spektrum AR6115e receiver from a Spektrum DX5e radio controller. The entire platform is powered by a 360mAH, 8.38V Turnigy Lithium-Polymer battery.

In previous testing, RR1 demonstrated a maintenance of untethered flight, high maneuverability, and diving capabilities [56]. Cruising flight speeds and climbing rates were measured at approximately 6.7 m/s and 0.53 m/s respectively. Robo Raven was the first untethered FWUAV that performed controlled, acrobatic maneuvers such as rolls and flips. Programmable wing kinematics and the ability to adjust flight modes were also demonstrated. It was also possible to program the wing dihedral, or internal angle between the wing tips, during a dive [70]. The wing dihedral had a direct effect on the dive path and descent speed. Finally, it was possible to modify Robo Raven with sensors to allow for more intelligent flight behavior [96].

Parameter	**Robo Raven**	**Common Raven**	**Unit**
Total Mass	0.29	0.69–2.00	kg
Length	0.554	0.63	m
Wingspan	1.168	1.00–1.50	m
Average Chord	0.248	0.21	m
Aspect Ratio	2.01	2.77	–
Flight Speed	6.7	9.80–12.50	m/s

Table 2.2: Comparison of properties of Robo Raven1 and Common Raven

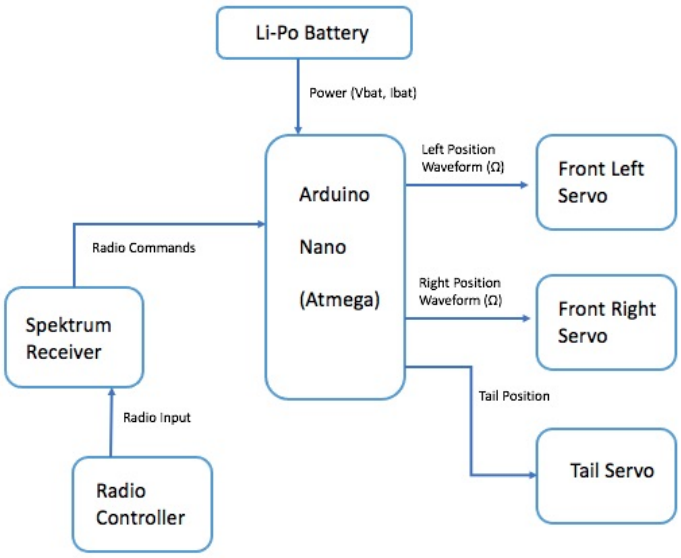


Figure 2.5: The RoboRaven1 hardware system diagram.

CHAPTER 3
STATE SPACE MODELING THE FLIGHT DYNAMICS AND BATTERY UTILIZATION FOR HYBRID FLAP/GLIDE FLIGHT

This chapter will discuss the development of a mathematical model that was capable of simultaneously capturing the simulated flight path profile and battery dynamics of the RoboRaven1 platform. The purpose of this model was, firstly, to simulate the flight and power system behavior of the Robo Raven1 platform with the understanding that this information would inform intermittent gliding strategies. Secondly, this model became a means by which theoretical intermittent glide strategies were tested for viability [46, 73]. The development of this model is step one in this work's methodology to explore the ability of intermittent gliding to improve flight performance. This step will be followed by flight experiments and models that will further explore this concept.

This chapter will begin with presenting the development of a novel state-space representation that combined an extended phugoid model with battery and servo motor dynamics. The theory and method of extending the traditional phugoid model to represent RoboRaven1's gliding and flapping behavior will be discussed. Furthermore, this chapter will present an expansion of the battery model to improve accuracy and fit a lithium-polymer battery configuration. It will also examine the specific equations and methods by which the battery model was combined with a model representing the mechanical and electrical dynamics of a servo motor.

Next this chapter will discuss the voltage-based, altitude-based, and time-based methods of intermittent gliding that were simulated using the model. It will display a graphical comparison between the three methods and discuss the results of the comparisons.

3.1 Extension of Phugoid Model

As was stated in the previous chapter, the original phugoid model characterizes the gliding flight path of an aerodynamic vehicle. However, in order to model the full flapping/gliding behavior of

Robo Raven 1, the model was expanded to include a term that represented the thrust produced by Robo Raven's flapping stroke. Starting once more with a point-mass representation of the aircraft, the platform's thrust vector is added to the $\hat{b}_1$ axis in the same direction as its ν vector. Applying Newton's second law reveals a new equation with thrust represented.

$$-mg\hat{e}_2 - F_{drag}\hat{b}_1 + F_{thrust}\hat{b}_1 + F_{lift}\hat{b}_2 = m(\dot{\nu}\hat{b}_1 + \nu\dot{\theta}\hat{b}_2). \tag{3.1}$$

Further division into the $\hat{b}_1$ components, yield the following equation. The original equation for the flight path angle, $\dot{\theta}$, derived in chapter 2 remained unchanged.

$$m\dot{\nu} = -mg\sin\theta - F_{drag} + F_{thrust} \tag{3.2}$$

The thrust equation used to expand the phugoid model was developed from previous work [49, 99, 12, 101] which indicated the proportional increase of thrust with the amplitude of flapping angle and the square of flapping frequency, Ω_{flap}. This equation was successfully utilized in previous Robo Raven research [99]. As can be seen in equation 3.3 the wing stiffness ,k_f, wing area, A_w, and flapping angle,$\Delta\alpha$, were constants relating the Robo Raven wing parameters and flight behaviors to the flapping frequency (Ω_{flap}). A coefficient, $C_{T,flap}$, was used to represent the wing parameters relating thrust with Ω_{flap}. Therefore, Eq.3.4 was developed.

$$F_{thrust} = k_f A_w \Delta\alpha \Omega_f^2 \tag{3.3}$$

$$\dot{\nu} = -g\sin\theta - C_D'\nu^2 + C_{T,flap}\Omega_f^2 \tag{3.4}$$

As was stated before, the generation of thrust on the Robo Raven platform is generated via the front servo motors. A servo motor transforms the angular rotation of an internal DC motor to the controllable angular rate of its servo horn via a gear drive train and an internal potentiometer. The battery and motor models are connected via the principle that the voltage and current are

transferred from the battery to the servo's internal DC motor. Therefore, a gear ratio needed to be calculated that would transform the flapping angular rate, seen in the thrust term (3.3), into the internal motor's angular rate (Ω). The final relationship between the motor's angular rate (Ω) and the flapping angular rate (Ω_{flap}) can be seen in equation3.6. The gear model shown below was developed to adequately represent the Futaba S9373SV's unique gear drive train. The analysis of the gear ratio, K_g followed the basic principles of the law of gearing. The number of teeth for each gear was counted and can be seen in table 3.1. Noting the position and connection of each gear, the the ratio formula seen in equation 3.5 was developed. Adding the gear ratio to equation 3.4, equation3.7 was developed.

$$Kg = \frac{-B}{A}\frac{-D}{C}\frac{-F}{E}\frac{-H}{G} \tag{3.5}$$

$$\Omega_{flap} = \frac{\Omega}{K_g} \tag{3.6}$$

Gear	Number of Teeth
A	10
B	50
C	10
D	41
E	16
F	37
G	12
H	43

Table 3.1: Number of teeth for each internal gear

As was shown in the phase portrait analysis of chapter 2 (figure 2.2), the choice of aerodynamic coefficients (C_L and C_D) is very important in determining the stability of the model. Previous Robo Raven research used a combination of kinematic equations and experimental data to determine the coefficients of lift and drag in a diving maneuver [56]. Assuming the wings were at a 40° dihedral angle, the coefficients were found to be: $C_{D_x} = 1.7, C_{D_y} = 0.7$ and $C_L = 0.19$. These values were used to inform the model developed in this work. However, the adapted phugoid model varied in

the following two ways.

Firstly, this model assumed that the flapping and gliding coefficients of lift were different. In the steady-state analysis of a fixed-wing craft one might use a gliding test to determine an overall coefficient of lift (peak) that is valid for both powered and unpowered flight regimes [11, 15]. However, this analysis assumes that the wings do not generate thrust through constant deformation [11, 12, 14]. With a flapping vehicle, this may not be assumed. Therefore, it is reasonable to postulate that the lift coefficient generated by "fixed" wings when gliding differs from the lift coefficient generated when the wings are flapping.

Secondly, the adjusted phugoid model assumed that during a glide, the wings are held at a 0° dihedral angle (not a 40° angle). The resulting increase in flow-contacted, surface area should also increase the lift according to the lift equation. Therefore, in turning to previously determined lift coefficients from an idealized fixed wing craft [102], the final lift coefficient during gliding was determined. The final nominal values for the coefficients of lift and drag were formulated: $C_D = 0.1, C_{L,flap} = 0.5, C_{L,glide} = 2$. This gives a $C_{L,glide}/C_D$ ratio of 20 and a $C_{L,flap}/C_D$ ratio of 5.

$$\dot{\nu} = -g \sin\theta - C'_D \nu^2 + \frac{C_T}{K_g^2}\Omega^2. \tag{3.7}$$

Finally, the original phugoid equations did not characterize RoboRaven's horizontal and vertical flight. Therefore, the following equations were quadratically obtained.

$$\dot{x} = \nu \cos\theta \tag{3.8}$$

$$\dot{z} = \nu \sin\theta \tag{3.9}$$

3.2 Extension of Battery and Motor Model

It was assumed that each onboard servo posses a common electro-mechanical motor whose dynamics could be described by a resistor-inductor circuit with backwards electromotive force (EMF). Back EMF relates the motor's angular velocity to the internal current. Let K_I denote the motor torque coefficient, b the motor damping coefficient, and J the motor moment of inertia. The dynamics of the motor angular rate arise from Euler's second law, where the last term denotes the load torque.

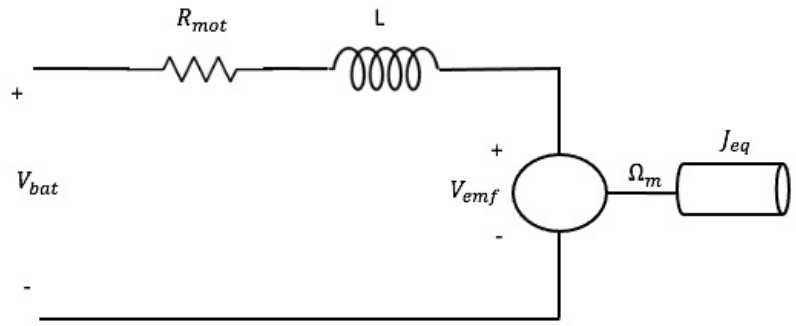


Figure 3.1: This figure shows the reference motor circuit from which the motor model equations were derived.

$$\dot{\Omega} = \frac{K_I}{J} I_{mot} - \frac{b}{K_g^2 J}\Omega - \frac{1}{J}\Omega, \tag{3.10}$$

The corresponding dynamics for the motor current from Kirchoff's law are

$$\dot{I}_{mot} = \frac{1}{L} V_{bat} - \frac{R_{mot}}{L} I_{mot} - \frac{K_{emf}}{L}\Omega, \tag{3.11}$$

where R_{mot} is the motor coil resistance, L the motor inductance, and K_{emf} the electromotive force constant. Finally, because the direction of current in the motor coils is the opposite of the direction in the battery, let $I_{bat} = -I_{mot}$.

The onboard lithium-polymer battery is modeled by differentiating the equivalent circuit model (2.8) and the Coulomb counting model (2.9) with respect to time, assuming R_{bat} and $VOC = SOC = Z_{bat} \in [0,1]$ are state variables. As was mentioned in chapter 2, the accuracy of an equivalent circuit model can be improved by relating the circuit elements to Z_{bat}. Following [81, 86], R_{bat} is an exponential function of Z_{bat} given by

$$R_{bat}(Z_{bat}) = R_{bat}(0)(1 - e^{K_{soc}Z_{bat}}),\ K_{soc} < 0,\ Z_{bat} \in [0,1], \tag{3.12}$$

which implies

$$\dot{R}_{bat} = \frac{d}{dt}\left(R_{bat}(0)(1 - e^{K_{soc}Z_{bat}})\right) = -R_{bat}(0)K_{soc}e^{K_{soc}Z_{bat}}\dot{Z}_{bat}. \tag{3.13}$$

For this model to work properly, an acceptable, initial R_{bat} value had to be calculated. This was achieved using a simple experimental setup and, to ensure idealized conditions, a brand new lipo battery. First, the initial voltage of the battery was measured. Then, the battery was placed under load for 10 seconds and the voltage measured again. The current was also measured during this drop. Using equation 3.14, the internal resistance was calculated.

$$R_{bat}(0) = \frac{V_{init} - V_{load}}{I_{measured}} \tag{3.14}$$

Figure 3.2 illustrates the effect of the parameter $K_{R_{bat}} < 0$ on the battery discharge behavior, where $R_{bat}(0) = 0.036$. As $K_{R_{bat}}$ increases in negativity, the R_{bat} curve asymptotically approaches $R_{bat}(0)$. From these graphical results, a K_{bat} value between -2 and -5 was chosen.

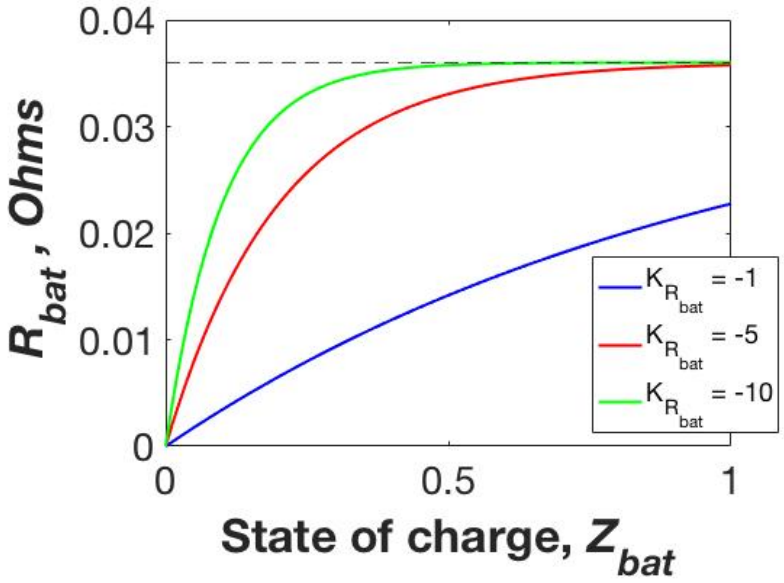


Figure 3.2: The effect of $K_{R_{bat}}$ on the battery resistance $R_{bat} = R_{bat}(Z_{bat})$

Finally, the equations of motion combining the flight, motor, and battery dynamics during the flapping phase can be seen in the equation 3.15–3.23 below.

$$\dot{x} = \nu \cos\theta \tag{3.15}$$

$$\dot{z} = \nu \sin\theta \tag{3.16}$$

$$\dot{\theta} = \frac{-g\cos\theta + C'_{L,flap}\nu^2}{\nu} \tag{3.17}$$

$$\dot{\nu} = -g\sin\theta - C'_D\nu^2 + \frac{C_T}{K_g^2}\Omega^2 \tag{3.18}$$

$$\dot{\Omega} = \frac{K_I}{J}I_{mot} - \frac{b}{K_g^2 J}\Omega - \frac{1}{J}\Omega \tag{3.19}$$

$$\dot{I}_{mot} = \frac{1}{L}V_{bat} - \frac{R_{mot}}{L}I_{mot} - \frac{K_{emf}}{L}\Omega = -\dot{I}_{bat} \tag{3.20}$$

$$\dot{Z}_{bat} = -\frac{I_{bat}}{Q_{bat}} \tag{3.21}$$

$$\dot{R}_{bat} = -R_{bat}(0)K_{R_{bat}}e^{K_{R_{bat}}Z_{bat}}\dot{Z}_{bat} \tag{3.22}$$

$$\dot{V}_{bat} = \dot{Z}_{bat} - R_{bat}\dot{I}_{bat} - \dot{R}_{bat}I_{bat} \tag{3.23}$$

When the platform is gliding, the battery and motor dynamics are disengaged and the state-

space equations revert to the original phugoid model (2.4–2.5). Tables 3.2 and 3.3 list the initial conditions and parameters, respectively. The choice of initial conditions were based upon previous Robo Raven research (i.e $\nu(0)$ and $V_{bat}(0)$) or parameters from the environment (i.e z(0)). As was seen above, $R_{bat}(0)$ and K_g were determined experimentally. The wing stiffness parameter, within (C_T), was also chosen based on previous Robo Raven experimentation as seen in figure 3.3. The variables, Q_{bat}, C_T, K_I, and K_{emf} were all calculated based upon the mechanical specifications of Robo Raven's components. The values J, L, and b served as gains to tweek the model fit. Finally, the aerodynamic coefficients were chosen via the method described previously.

State	Description	Units	Initial Value
x	Horizontal position	m	0
z	Vertical position	m	2
θ	Flight path angle	rad	0
ν	Flight speed	m/sec	7.4
Ω	Motor angular rate	rad/sec	0
I_{mot}	Motor current	A	1
Z_{bat}	Battery state-of-charge	N/A	1
R_{bat}	Battery internal resistance	ohms	0.036
V_{bat}	Battery voltage	V	8.5

Table 3.2: Initial conditions of the combined flight, motor, and battery dynamical system

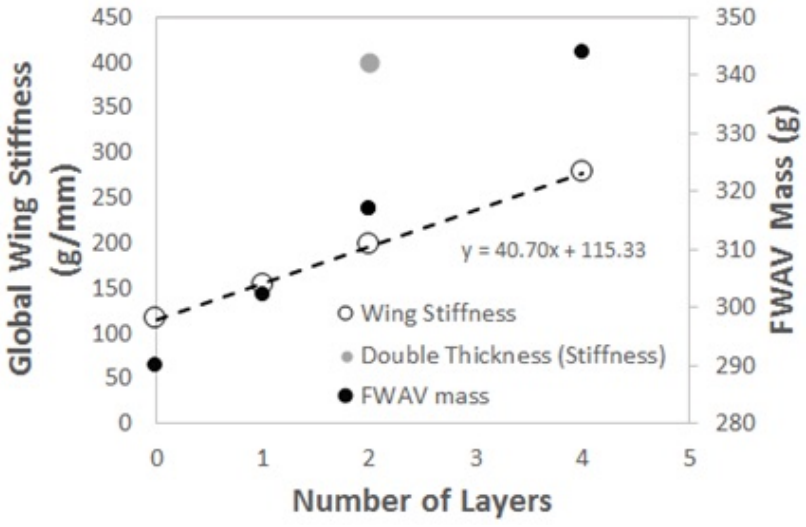


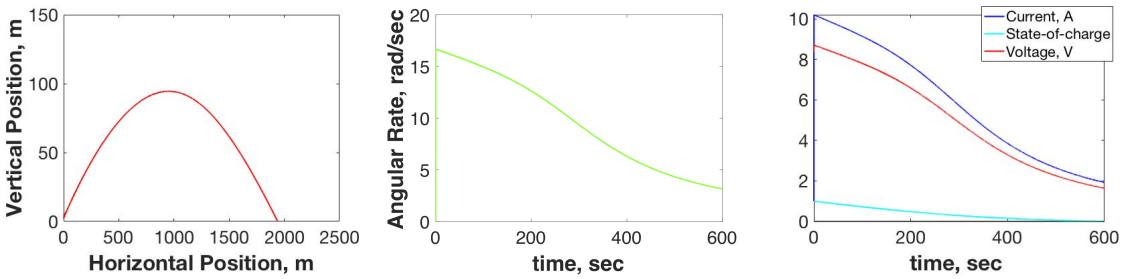
Figure 3.3: This graph shows the results of experimentally obtained values of wing stiffness.

Figure 3.4 depicts a numerical simulation of the state-space system (3.15–3.23) for the flapping

Parameter	Description	Units	Value
C'_D	Coefficient of drag	N/A	0.1–0.5
$C'_{L,flap}$	Coefficient of lift during flapping	N/A	0.5–1
$C'_{L,glide}$	Coefficient of lift during gliding	N/A	1–2
C_T	Coefficient of thrust	N/A	386.4
g	Gravity	m/sec^2	9.81
K_{emf}	Electromotive force constant	V/rad/sec	0.4
b	Motor damping coefficient	N·m·sec	0.2–0.5
K_g	Gear ratio	N/A	169.87
J	Moment of inertia	kg·m^2	0.01
L	Motor inductance	H	0.01
R_{mot}	Motor coil resistance	Ohms	0.2–0.5
K_I	Motor torque coefficient	N·m/A	1.63
R_{init}	Battery discharge resistance	Ohms	0.036
Q_{bat}	Battery capacity	A·sec	1332
$K_{R_{bat}}$	Resistance parameter	N/A	-(2–5)

Table 3.3: Parameters of the combined flight, motor, and battery dynamical system

mode using initial conditions and parameters in Table 3.2 and 3.3. The range of values noted in Table 3.3 have been used in the model; the results included were produced using the following nominal values determined by assuming that the angle of attack gives near optimal aerodynamic efficiency: $C'_D = 0.1$, $C'_{L,flap} = 0.5$, $C'_{L,glide} = 2$, $b = 0.2$, $K_{R_{bat}} = -2.5$. As can be seen in the output, the battery discharges over time as the servos consume energy. The flight path is parabolic, because the vehicle gains altitude only when the motor angular rate is sufficiently high. As the battery voltage drops, the motor angular rate decreases and the vehicle descends even while flapping. However, because the platform is still flapping but with diminished power, it maintains a lift coefficient of $C_{L,flap}$ and exhibits a steep descent angle. Z_{bat} is normalized to fit in the range [0,1]. The impact of implementing an intermittent gliding duty cycle on battery longevity and flight endurance is examined next.



(a) (b) (c)

Figure 3.4: Simulation of continuous flapping mode: (a) longitudinal dynamics; (b) angular rate; and (c) onboard energy usage.

3.3 Glide Cycle Design and Performance Analysis

Natural flyers utilize a variety of intermittent flight modalities based upon constraints such as atmospheric conditions, energy level, and altitude. This section describes the analysis and comparison of three intermittent gliding/flapping modalities: (1) time-based switching; (2) altitude-based switching; and (3) voltage-based switching. Each modality has strengths and weaknesses. These modalities were studied for the purpose of creating a framework of options that can be tailored to a particular robotic application and provide an increase in the performance parameters when compared to only flapping and no gliding.

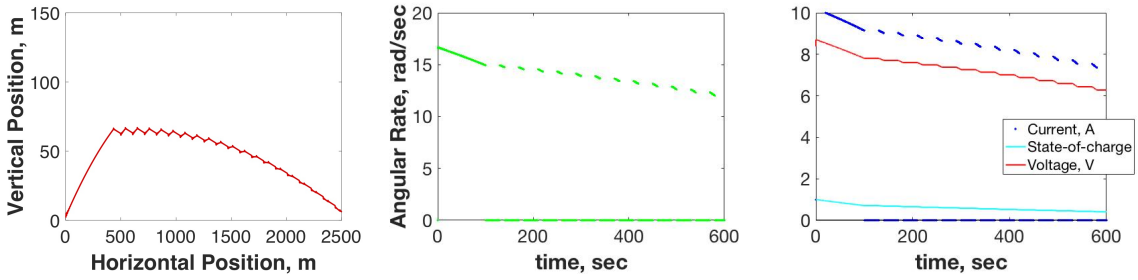
The performance parameters, battery endurance and effective flight distance, were chosen to evaluate the performance of intermittent gliding and flapping. Because the RoboRaven servos shut off at 6V [95], the vehicle gains altitude while flapping only when the battery voltage exceeds 6V. Therefore, battery endurance is defined as the duration of time the battery provides 6V or more. Furthermore, the platform should maintain a minimum height during flight. The effective flight distance is the horizontal distance traveled while remaining higher than the initial altitude.

3.3.1 Time-based switching

The time-based intermittent gliding modality is characterized by the duration of time the platform performs flapping or gliding before switching, i.e., the duty cycle. The duty cycle can be symmetric, i.e., time spent flapping or gliding is the same, or asymmetric. Both symmetric and

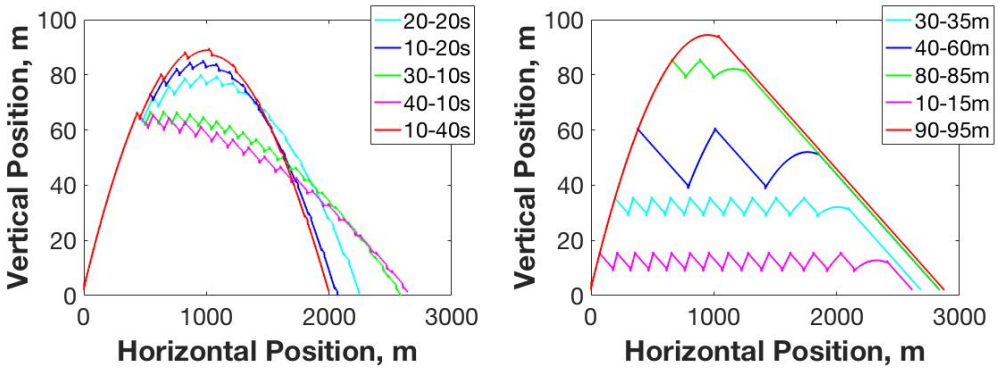
asymmetric duty cycles were tested to determine their respective effects on the model. Duty cycles were measured in seconds (glide–flap): 20–20, 30–30, 10–20, and 30–10.

The simulation results indicate an increase in battery endurance and flight distance when time-based switching is used in comparison to constant flapping behavior. As an example of the flight profile generated when intermittently gliding, Figure 3.5 shows a 30-10 second asymmetric duty cycle simulation, and Figure 3.6 (a) shows the longitudinal dynamics for a chosen series of duty cycles. Furthermore, the tabulated results shown in Figure 3.7 show that duty cycles with longer periods of gliding (both asymmetric and symmetric) yield the most improvement in the performance metrics. Specifically, the two asymmetric duty cycles with the longest gliding and shortest flapping times (30-10 and 20-10) performed the best in improving the performance metrics. Figure 3.8 shows a colorbar representation of time-based gliding and flapping switching, analyzed according to the performance metrics.



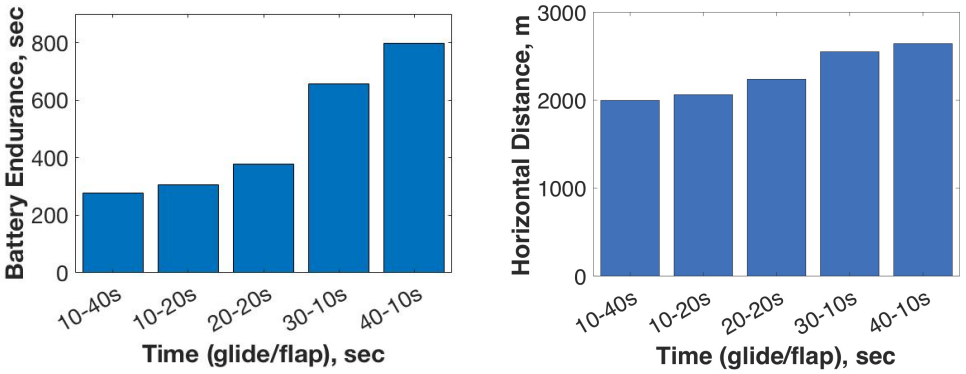
(a) (b) (c)

Figure 3.5: Model simulation with a 30-10 second duty cycle: (a) longitudinal dynamics; (b) angular rate; and (c) onboard energy usage.



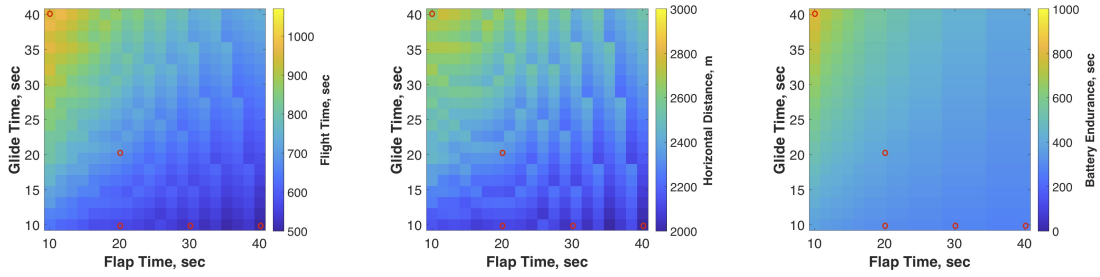
(a) (b)

Figure 3.6: Longitudinal dynamics with (a) time-based switching; and (b) altitude-based switching



(a) (b)

Figure 3.7: Simulation results for time-based switching: (a) battery endurance vs. glide cycle; and (b) flight distance vs. glide cycle



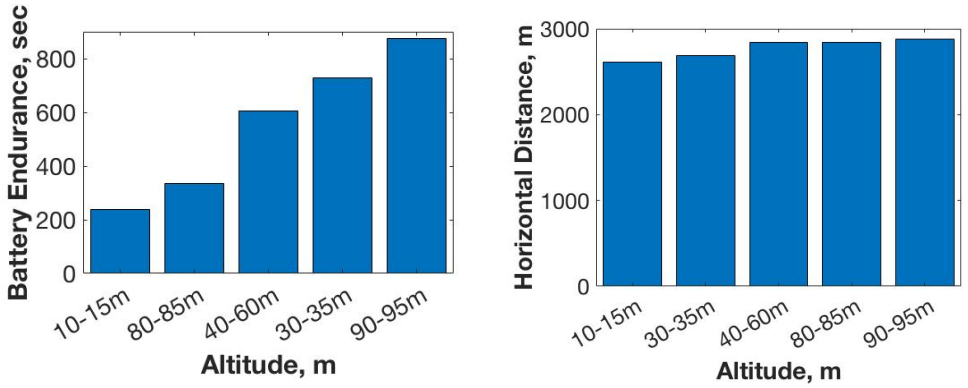
(a) (b) (c)

Figure 3.8: Flight distance and battery endurance for time-based switching. The red dots show the points chosen for the simulation results described above.

3.3.2 Altitude-based switching

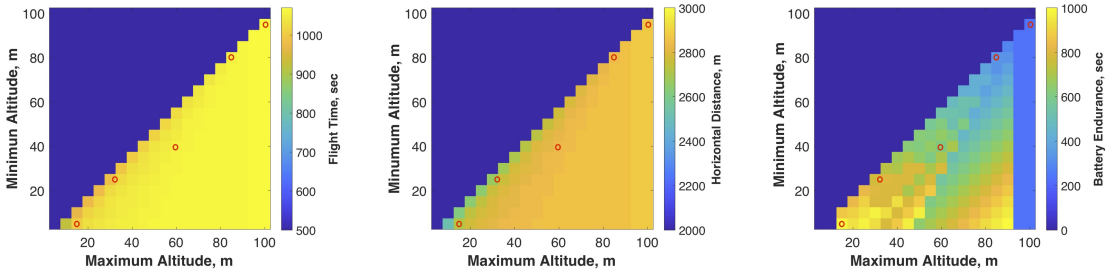
Altitude-based intermittent gliding is characterized by a cyclical increase and decrease in altitude during the flapping and gliding stages. This approach is based upon the choice of maximum flapping altitude and minimum gliding altitude. Cycle outcomes in flight distance, battery endurance, and flight time can be tuned to fit the application. Maximum and minimum altitudes from 2m to 100m were tested. When the minimum voltage was reached (6V), the simulation initiated a final glide to the ground. Fig. 3.6 (b) shows a selection of the maximum/minimum altitude combinations. Fig. 3.8 shows a larger representation of the final results in the flight distance, battery endurance and final flight times of each combination.

Altitude-based switching is another way of improving flight distance and battery endurance in comparison to a constant flapping behavior, as can be seen in Fig. 3.9. However, when comparing time-based and altitude-based switching, an interesting principle arises. The altitude-based flights all achieved greater flight distances than the time-based glides. However, the altitude-based flights with very high maximum altitudes had a worse battery endurance outcome than altitude-based flights with lower maximum altitude and most of the time-based flights. Furthermore, most of the flight distance advantages in the altitude-based flights comes from the final glide stage that occurs after the battery has reached its terminal voltage. Therefore, while reaching a battery exhausting height and gliding to the ground does increase the flight distance, it yields a decrease in effective battery endurance. Figure 3.10 shows altitude-based switching gliding and flapping times, analyzed according to the performance metrics. The upper region of the graphs represent infeasible altitude combinations where the maximum altitude is below the minimum altitude. The battery endurance color graph shows a crossover point in performance around the 5m minimum altitude and 50m maximum altitude point.



(a) (b)

Figure 3.9: Simulation results for altitude-based switching: (a) battery endurance vs. altitude-based cycle; and (b) flight distance vs. altitude-based cycle



(a) (b) (c)

Figure 3.10: Flight distance and battery endurance for altitude-based switching. The ”null” space above the altitude outputs represent impossible altitude combinations where the minimum altitude is larger than the maximum. The red circles show the points tested by the original simulation.

3.3.3 Voltage-based switching

The voltage-based intermittent gliding modality is characterized by a single transition from flapping to gliding when the minimum voltage is reached. From there, the platform glides until it reaches the initial altitude. For this modality, the battery endurance is defined as the amount of time it takes to get to the minimum voltage V_{min} rather than 6V. Minimum voltages for this experiment ranged between 6V and 8V; 0V is a base value representing an all-flapping mode.

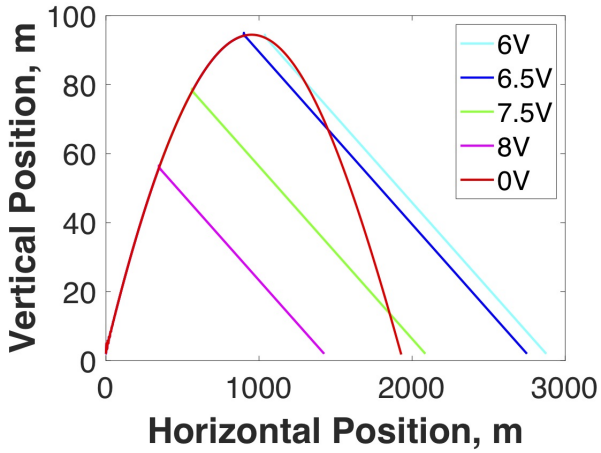
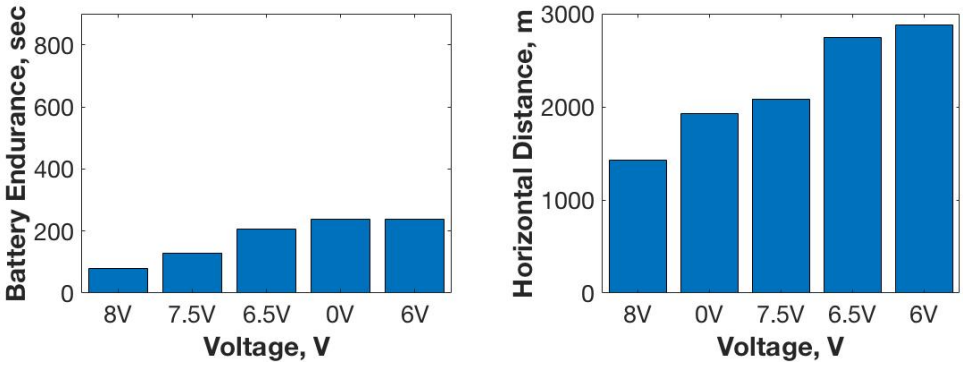


Figure 3.11: Longitudinal dynamics using voltage-based switching



(a) (b)

Figure 3.12: Simulation results for voltage-based switching: (a) battery endurance vs. voltage-based cycle; and (b) flight distance vs. voltage-based cycle

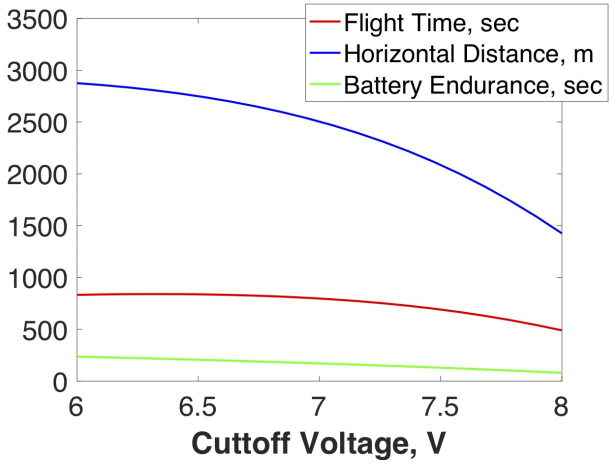


Figure 3.13: Performance of voltage-based switching mode

The results show that while voltage alone can be used as a switching variable, it should be considered along with other parameters such as altitude. Cutting the battery off at the highest level (8V) did not improve the battery endurance or the horizontal distance. Since there is only one glide cycle in this modality, rather than a constant switching that might use some of the residual voltage, the 8V could not cover a significant distance because the flight was terminated before it reached an advantageous height. Setting V_{min} = 6V–6.5V improves the horizontal distance and battery endurance. A range of results across multiple V_{min} are shown in Fig. 3.13.

3.4 Conclusion

This chapter presented a state-space model describing hybrid flapping and gliding behavior of a flapping-wing unmanned aerial vehicle by combining the phugoid model of flight dynamics, an electro-mechanical motor model, and a Thévenin equivalent battery model was developed. This state-space representation, directly related the gliding-flapping performance of the platform to the onboard energy utilization and was used in a numerical simulation to demonstrate the flapping behavior of a FWUAV. This demonstration was used as a baseline comparison to hybrid flights. Using the numerical simulation, the performance of three hybrid flight modalities were compared with respect to battery endurance and flight distance. Finally, the numerical simulation showed that intermittent flight affected, and in most cases, improved overall flight performance.

CHAPTER 4

GLIDING WING DESIGN AND PERFORMANCE CHARACTERIZATION

It is a well-studied principle that a flapping vehicle's wing planform affects all of its flight characteristics including thrust generation and gliding performance [103, 104, 102]. Therefore, this section describes the theory and experimental results of a study on the gliding performance of various FWUAV wing planform designs. Background information defining wing planform and describing its effect on flight performance will be presented as context for the following flight analysis of gliding wings. Chosen wing designs will be presented as potential candidates for flight analysis, mathematical evaluation and to explore the effects of wing design on potential intermittent gliding success. Finally, a flight demonstration to evaluate and compare the gliding performance of the various wing designs will be presented and discussed.

4.1 The Study of Glide Performance and Wing Geometry

A wing's planform is defined as its geometric shape as viewed from above [104, 105]. The planform is specified by parameters such as taper, aspect ratio, twist and camber [102, 104] which directly affect the flow of air over the wing and, therefore, affect such aerodynamic parameters as lift, drag, Reynold's number, flight velocity, and the gliding performance. In many instances there is a close corollary change in flight behavior resulting from a change in one aspect of planform geometry. For instance, low aspect ratio wings (wings with a generally small span compared to its chord) are known have higher drag coefficients than other wings, but also significantly lower Reynold's numbers [106]. As another example, wings with high tapering (the progressive decrease in camber from base to tip) tend to increase lift and decrease drag without much added weight [104, 105].

The resulting diversity in overall planforms, ranging in shape from elliptical to rectangular and even triangular, represent a large design space in which wing shape may be tailored to specific

flight types (subsonic, acrobatic etc.) as well as flight and gliding behavior [105]. Multiple studies have explored and expanded this design space for different flight vehicles including for micro-air vehicles [106]. However, it is in combination with an understanding of biological wing planforms and their relationship to flight behaviors that the elements of wing design theory might be applied to flapping-wing systems. For the most part, the thrust and power dynamics of a traditional aircraft are not generated by the wings. However, biological systems and flapping wing vehicles rely on their wing planform for flight generation and glide effectiveness.

The diversity of flight behavior in biological systems is as large as the actual number of flying species. However, it has been shown that clues toward understanding flight behavior may be gathered from wing shape [107, 108]. According to a study by Cornell's Ornithology Laboratory, avian wing planforms can be divided into five categories based upon both their shape and the general type of flight behavior to which they correlate. For example, wings that enable soaring behavior can be described as passive, having long primary feathers that enable birds to catch thermals in the atmosphere [107, 108]. Other wings can be described as "active", having a long span and very short cord that enable birds, such as albatrosses, to glide for very long distances. Other categories include elliptical wings (good for short bursts of energy and acrobatics), high speed wings, and hovering wings. With this in mind, it can be hypothesized that, starting from a base shape, progressive changes in a wing planform, according to aspect ratio, taper, curvature and wing area might shift the bird's flight behavior from a long range glider to an acrobatic glider, or from a swift flying bird to one that hovers in one place [108].

Observing this phenomenon in biological systems has led to the exploration of the flapping-wing, planform design space as it correlates with flight behavior. An example of this is the work that was done by Ansari [103] who explored the effect of wing geometry on the hovering behavior of an insect-inspired MAV. He explored a design space of 13 different wing planforms that varied based on aspect ratio, pitch axis, radial chord and length. Furthermore, he developed equations that related the total lift of the platform to the wing planform, length and area. The final results of his simulations tracked the increase of decrease if total lift as a function of the wing planform

[103]. Similar work was done by Singh and Chopra [109] with the addition of a stationary flapping apparatus on which realistic experimental data was gathered on various insect-inspired wing designs. His work showed a direct correlation between force generation and wing planform and material composition [109].

Finally, as was stated previously in chapters 1 and 2, Gerdes completed work on the parameterization of Robo Raven wings. In his work he created a series of wings that were scaled 35%, 60% and 100% in area from the designated baseline wing [57, 95]. His work included simulation and experimental results that confirmed the direct effect of wing area on the generation of lift and thrust. He also showed that effective flapping frequency increased or decreased because of wing area and power draw and that acrobatic capabilities were also affected. His processes and results informed the research presented in this chapter [57, 95].

4.2 Development and Analysis of Chosen Wing Geometries

A Robo Raven wing design characterization study was developed to correlate intermittent gliding potential with specific changes in wing planform parameters based on glide performance. The goal of this design space was to (1) experimentally understand the effects of changes in wing area and aspect ratio on the aerodynamic parameters affecting glide performance and (2) to create a framework that might be used to tailor future wing designs to a desired intermittent gliding behavior. It is important to note that all Robo Raven wings have a very similar and high taper ratio. Therefore, aspect ratio was chosen as a more important parameter. As the research conveyed, the chosen wing parameters should directly affect the generation of lift and drag as well as the spatial placement of laminar or turbulent flow on the wing. These changes, in turn, should affect gliding parameters such as the horizontal distance (d), flight velocity (ν), flight path angle (θ) and overall gliding profile.

Understanding how changes in these parameters would affect gliding performance began with a mathematical representation of the Robo Raven1 wing planform. Firstly, a definition of each of the parameters was necessary. Figure 4.1 gives a visual representation of each parameter as they

pertain to a wing's geometry. The aspect ratio was defined as the ratio of a wing's span (S) to its chord (C_b). A wing with a higher aspect ratio would have a larger span and smaller chord and vise versa for a wing with a lower aspect ratio. Finally, the wing's area had to be specially derived for Robo Raven 1's unique wing planform. It was observed that the wing area could be derived by subdividing the total area into the area of a rectangle with an arced area removed. Therefore, the equation for wing area is as follows, with the area of the rectangle portion being a function of the wing's span (S) and chord at the base (C_b), and the arched section represented by the function Γ.

$$WingArea = C_b S - \Gamma \tag{4.1}$$

As can be seen in figure 4.1, the wing's arced section was divided into 5 subsections (y), which were used in deriving the arced section's area using the trapezoidal rule. The final arced area can be seen below.

$$\Gamma = \frac{\Delta y}{2}[f(y_0) + 2f(y_1)...2f(y_4) + f(y_5)] \tag{4.2}$$

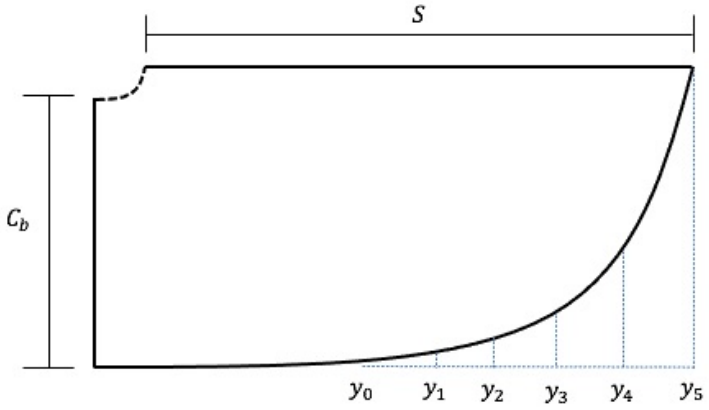


Figure 4.1: Geometric representation of Robo Raven 1 baseline wing with important design space parameters

4.2.1 The Original Robo Raven1 Wing Planform

The original Robo Raven 1 wing was designed with planform parameters that mirrored the average wingspan of a raven bird [56]. Therefore, it does not have a comparatively high aspect ratio. Nonetheless, this original wing has shown good results in previous flight, test stand and dive testing [56] and will be used as a control group for the wing design study. Its wing planform parameters as well as a picture of the original wing can be seen in table 4.2 and figure 4.2 below.



Figure 4.2: The original Robo Raven1 Wing.

4.2.2 The Chosen Wing Planforms

Three wing planform specimens were chosen for the characterization study and design space development. Each specimen was designed to exhibit an analytical alteration of one or more important design space parameters. The first two wing specimens, wings A and B, had the same parameters as the two wings used in [57, 95]. From the original wing, these wing planforms have been scaled up and down by approximately 8 $\%$ and 28$\%$ in area, while maintaining essentially the same aspect ratio. These wings were chosen because their tests might indicate if scaling area has a positive or negative affect on the platform's lift production. It might also analyze the potential for stalling behavior. The natural inspiration for these wings were birds that have wing shapes similar to a raven's but are smaller (like a crow) or larger (like an eagle) in area. Wing E has a more severe taper and higher aspect ratio than the other wings. Results of this wings test might be used to

elucidate the effects of aspect ratio and taper in the increase or decrease of drag. The natural inspiration of this wing was the albatross, whose high aspect ratio wing enables long soaring flights. The chosen wing planforms and their natural comparisons can be seen in Table 4.1. Please note that this analysis will maintain the wing names designated in previous Robo Raven research [57]. This is why the previously unused specimen has been labeled Wing E.

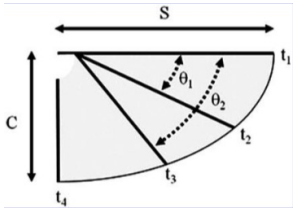
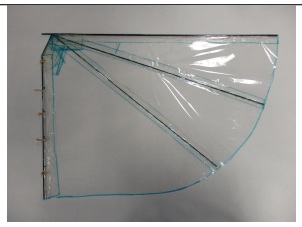
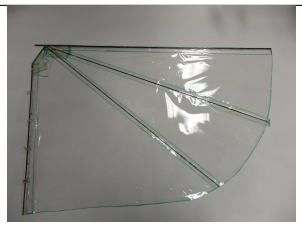
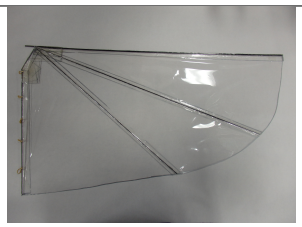
Bird wing	Flapping Wing	Adjusted Parameter
		0% AR, 0%A_w
		-11.6% AR, -8.2%A_w
		-12.2% AR, +28%A_w
		+3.4% AR, +20.9%A_w

Table 4.1: A comparison of the percent change in planform parameters between the original Robo Raven wing and the chosen wing specimens. The design chosen wing planform specimens were further inspired by the natural fliers of (a) a crow (b) an eagle and (c) an albatross [110]

Each wing specimen was characterized using the ratios and equations mentioned above. The wings were also weighed. The parameters of each wing can be seen in Table 4.2 below.

Wing Specimen	Weight (g)	Aspect Ratio	Wing Area (m^2)
Original	22.6	1.79	0.182
A	22	1.59	0.167
B	24.5	1.58	0.233
E	24.1	1.86	0.220

Table 4.2: Measured parameters for the original Robo Raven 1 wing and each wing planform specimen

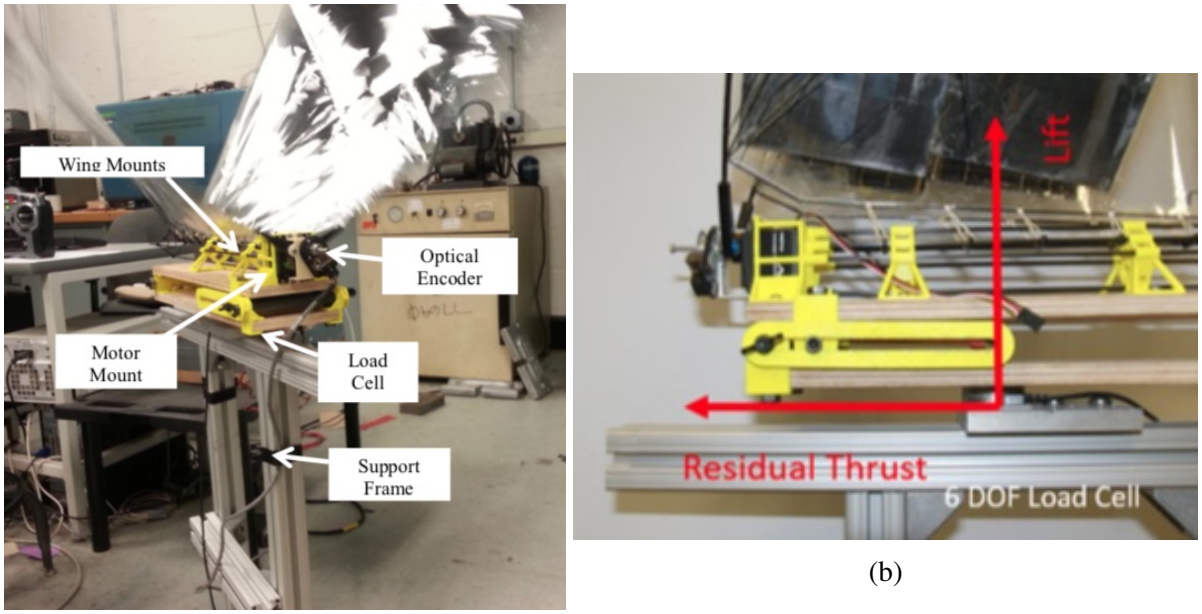
4.3 Experimental Study of Chosen Wings

An analytical relationship between wing planform and potential gliding performance, was required to develop the final design space. Therefore, a body of data was compiled on the three chosen wing specimens via a two-part characterization study. First, a prediction study was conducted using formerly acquired, Robo Raven 1 wing experimental data. Then, each wing was analyzed on the flying Robo Raven 1 platform in a free glide. The combined, experimental data and predictive modeling created a well-rounded characterization of the relationship between wing design and gliding performance.

4.3.1 Wing Prediction Study Using Test Stand Characterization

The wing prediction study used previously acquired force and torque data to analyze lift and drag trends as they pertain to changes in angle of attack. This information was then used, in conjunction with the equations for wing area and aerodynamic parameters described in the sections above, to interpolate the probable flight behavior of the chosen wing specimens. All previous wing experiments were conducted using a Robo Raven 1 configured, stationary apparatus and wind tunnel. The stationary apparatus was a non-flying Robo Raven 1 platform that was developed for precise force testing and wing characterization. It was a carbon copy of the flying Robo Raven 1 platform in that it possessed all of its actuators and control systems. The non-flying platform was placed upon a board that could be adjusted to up to an 18 $^\circ$ angle of attack. The platform's servo motors

were configured with a US Digital E5 optical shaft encoder which enabled the precise measurement of servo and wing angle when flapping. Force data was acquired using a six-axis, ATI Mini 40 transducer, which was placed under the platform's center of gravity. The transducer was rated for $< 1/50$ N resolution, however, previous characterization showed that the actual resolution was approximately, $< 1/100$ N [95]. To ensure that the servo motors and controller received the same amount of voltage throughout the test, power was controlled using a Powerwerx SPS - 30 DM, 30 Amp power supply. Data from the transducer was communicated using an ethernet connection and processed via a National Instruments Compact DAQ Chassis with NI 9227, NI 9402, and NI 9205 processors [95]. A MATLAB Simulink program was used to initiate the tests and record the data. The final data was then printed to an excel sheet.



(a) (b)

Figure 4.3: The Robo Raven 1 configured test stand (a) while flapping [95] (b) with the force direction notated [97]

During the experiments presented in this chapter, the platform was tested in airflow that mimicked flight airspeed. Therefore, a wind tunnel was developed that provided approximately 5 m/s of airflow to the platform. The wind tunnel was made of approximately 1in thick, Dupont construction foam and generated airflow using a large metal fan. Each stationary test was conducted at 0hz

flapping frequency and with the wings held at a 0°dihedral angle to mimic gliding behavior. The experiment consisted of three rounds of data acquisition, lasting approximately 45 sec each round, at 0°, 5°, 10°, 15°, and 18°angle of attack. Acquisition of data was initialized and controlled using the Simulink software. The wing used in the previous experiments was the 100 % wing referenced in [95] which is also this study's wing A.

As can be seen in figure 4.4, the raw F_z values are related to the actual lift values via the angle of attack. Therefore, the actual lift values were processed using equation 4.3 and plotted. An important observation seen in this data is that the platform's angle-of-attack directly affects its lift generation and that there exists an optimal angle-of-attack above which lift begins to decrease. There also exists a severe drop in lift between 15°and 18°and it might, therefore, be hypothesized that at these severe angles the platform begins to stall.

$$Lift = F_z \cos\theta \tag{4.3}$$

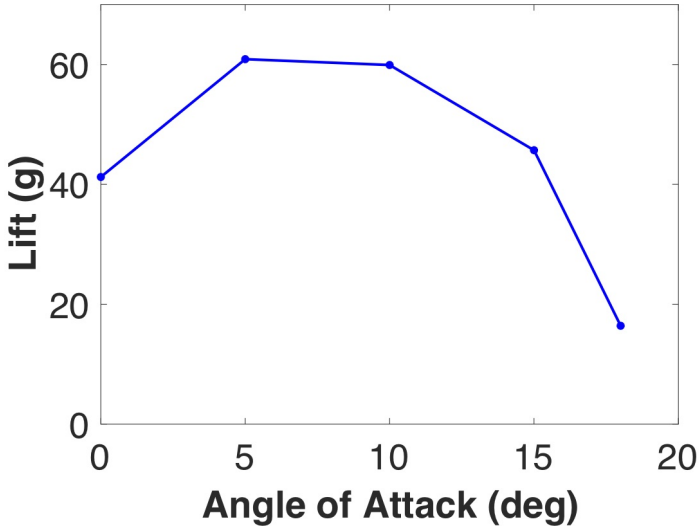


Figure 4.4: Raw lift vs. angle of attack data from previous wing experiments for wing A in a 5 m/s airflow wind tunnel. This experiment looked at the gliding behavior with two wings on the test stand

The slope changes in lift provide important insight into the gliding profile created by the previous wing configuration. Therefore, the predictive study focused on the potential change in lift

profiles for the chosen wing specimens. The slope formula was used to evaluate the Δ lift for each of the graphical data's four parameterized sections. For this analysis it was assumed that the slope of change in coefficient of lift ($\Delta C_{L,glide}$) was an unchanging independent variable for each of the wing specimens. Therefore, using the following equation, the calculated Δ lift and the previous wing's dimensions, the Δ lift for each of the wing specimens was predicted. The final data can be seen in figure 4.5.

$$\Delta Lift = \Delta C_{L,glide} 0.5 \rho \nu^2 A_w \tag{4.4}$$

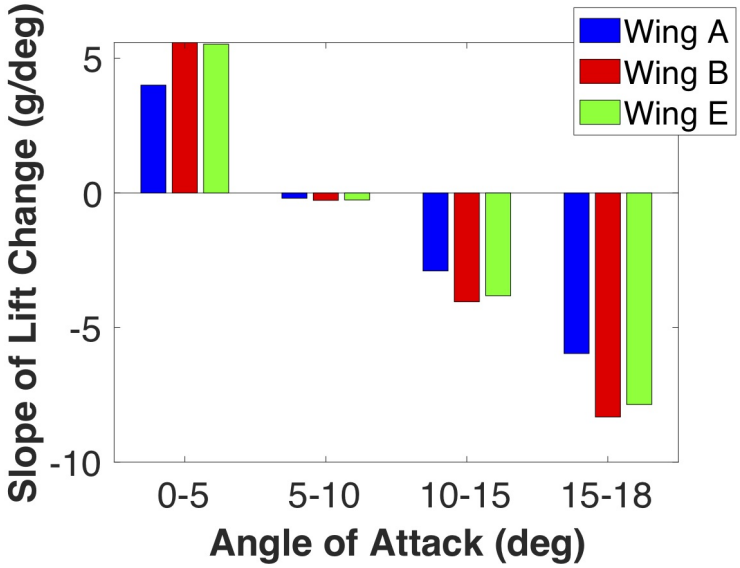


Figure 4.5: Interpolated, predicted slope of Δ lift values, scaled for each of the wing specimens according to slope of Δ angle-of-attack

$\Delta C_{L,glide}$	**Calculated Value (g/deg)**
Slope 1	1.566
Slope 2	-0.077
Slope 3	-1.133
Slope 4	-2.333

Table 4.3: Calculated slope of $\Delta C_{L,glide}$ from the previous wing A data that was used to calculate Δ lift for each of the wing specimens

The predictive study is only one part of the design space development, yet it yielded some important observations. Firstly, wing B, which has the largest planform area but the same aspect ratio as wing A, has the most severe negative Δ lift from 10°to 18°angle-of-attack. In the same way, wing E also showed a higher negative Δ lift than wing A, but not as much as wing B. These results may support the theory that an increase in aspect ratio combined with a high taper ratio can increase lift slightly better than an overall increase in area. The higher increase in Δ lift between flight angles 0°and 5°for both Wing B and C might further support this theory. The conclusions resulting from this data were compared with the gliding flight data.

4.3.2 Flight Analysis of Gliding Wings

Each wing specimen was tested on the Robo Raven 1 platform in a free glide. The expected outcomes of this type of analysis was (1) the analysis of each wing's flight path angle θ as derived from the gliding slope, (2) the graphical characterization of each wing's gliding profile, and (3) the analysis and comparison of each wing's $C_{L,glide}/C_D$ ratio. Furthermore, while the prediction study produced the potential aerodynamic outcomes of each wing based on a possible angle of attack, the flight analysis was designed to provide analytical representations of actual flight behavior to be used in the design space development.

Mathematical Characterization of $C_{L,glide}/C_D$ ratio

To begin, a mathematical model for the C_D to $C_{L,glide}$ ratio was developed using a 2D longitudinal model of the Robo Raven1 platform in free glide. Fundamentally, the ratio of C_D to $C_{L,glide}$ can be derived from the ratio of Lift to Drag [111, 112]. Derivation of the Lift to Drag ratio began with the phugoid equation from Chapter 2, i.e equations 2.2 – 2.3. It was assumed that the platform was in a free, smooth descent and not acted upon by thrust. This means that the rate of change for the flight speed ($\dot{\nu}$) and the flight path angle ($\dot{\theta}$) are 0. Therefore, the following equations are derived.

$$\frac{F_{lift}}{m} = -g\cos\theta \tag{4.5}$$

$$\frac{F_{drag}}{m} = g\sin\theta \tag{4.6}$$

Substituting the aerodynamic components, and simplifying the fraction, yields the following ratio.

$$\frac{C_{L,glide}}{C_D} = -\frac{\cos\theta}{\sin\theta} = -\frac{1}{\tan\theta} \tag{4.7}$$

The aerodynamic coefficients can be further related to the flight path, using the information in figure 4.6. Assuming a trigonometric relationship in the flight path, the angle of descent is related to the ratio of altitude (z) to flight distance (x), and the final equation achieved. Note, the ratio is negative, because the original definition of flight path angle was pointed upward.

$$\frac{C_{L,glide}}{C_D} = -\frac{d}{h} \tag{4.8}$$

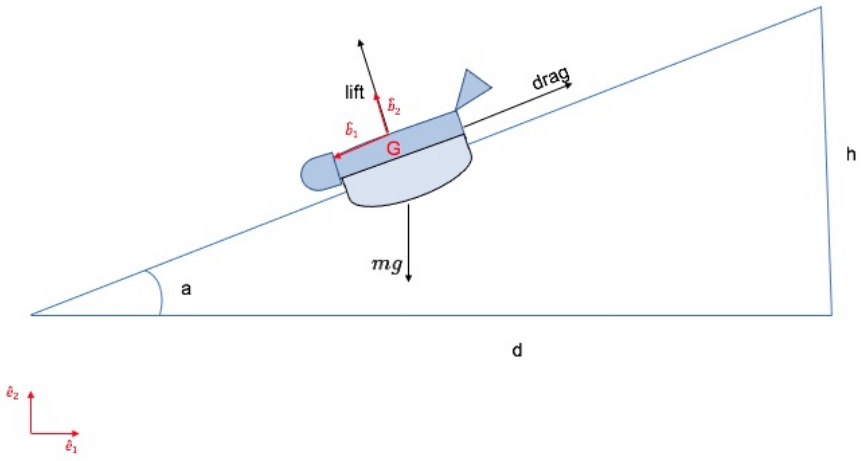


Figure 4.6: The gliding dynamics of Robo Raven1

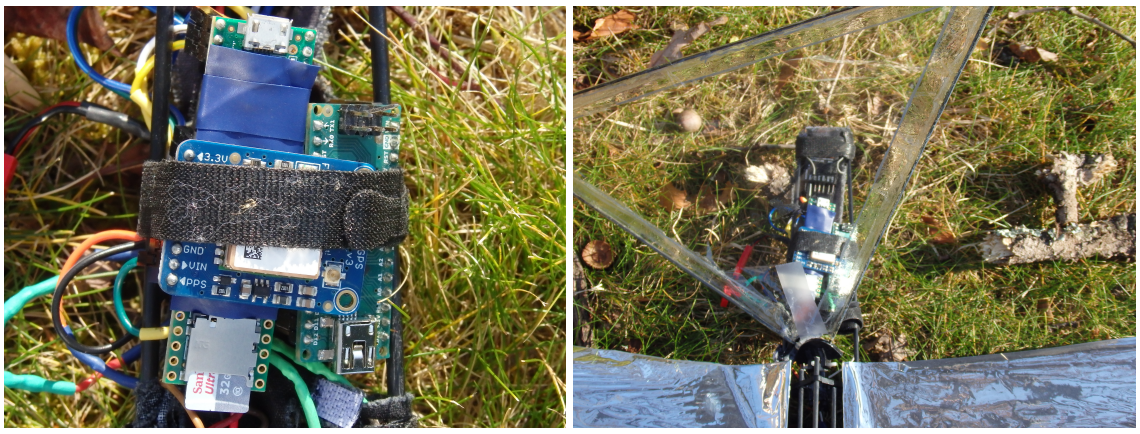
Measurement of Flight Distance and Phugoid Parameters

The important states representing Robo Raven 1's gliding path and phugoid dynamics are horizontal position (x), vertical position (z), flight path angle (θ), and flight speed (ν). Horizontal and vertical position characterize the flight distance and flight profile, while flight path angle and flight speed characterize flight efficiency and performance. Barometers, accelerometers, and magnetometers are some of the most common sensors used to measure these parameters. However, each of these sensors only measure a few of the important parameters and do not possess their own logging capabilities. Therefore, to get the desired data out of these sensors a group of them would need to be combined and additional weighty logging boards would have to be added.

Ultimately, a GPS unit became the sensor of choice as GPS sensors can not only measure all of the performance parameters, but also the corresponding positions, dates and times. The Adafruit GPS Breakout Board was chosen due to its low weight and easy setup. The Adafruit GPS can measure the longitude and latitude of the platform with an accuracy of $<$ 3m and with an update rate of 10 Hz. It is a 3.3V-5V powered sensor. All GPS systems work through satellite communication and therefore, require a satellite fix before data collection can begin. The accuracy of data can often be determined by the number of satellites a GPS system uses. The Adafruit GPS could fix to up to 8 satellites but required at least 30 seconds before all of the satellites were found and fixed upon. Furthermore, it possessed an internal antenna, which cut down on the excess weight of an external antenna but required that the antenna always be placed facing upwards and unobstructed.

The GPS could not be easily integrated into the current Robo Raven electronics without complicating the current code. Furthermore, although the GPS board possessed its own internal logging capabilities removing data from the internal flash was not a reliable process and often produced incorrect data. Therefore, a Teensyduino 3.6 was used as the controlling and logging board for the GPS. The Teensyduino 3.6 is an Arduino-compatible board containing multiple serial ports and analog/digital pins. It possesses its own on board microSD port, which enabled easy data logging. Finally, the Teensyduino 3.6 is powered by 5V, which could be supplied from the original Arduino

nano without an additional power source. Figure 4.7 shows the Teensyduino and GPS and its position on the rear of the platform.



(a) (b)

Figure 4.7: Pictures of the GPS sensor system showing (a) the Teensyduino and GPS and (b-c) the position of the GPS on the platform

Flight Analysis of Original Robo Raven Wing

Each gliding flight was performed using the modified Robo Raven 1 platform that was described above. The gliding flights commenced with the release of Robo Raven 1 from a hill of known height and ended when Robo Raven 1 reached ground. To ensure quality altitude data, the onboard GPS was allowed approximately 45 seconds to fix on as many satellites as possible before the flight was initiated. The glide began with a brief 1 - 2 second flapping phase to get the platform up to flight speed. Afterwards, the servo motors were shut off by the human operator, at a dihedral angle of 0°, and the platform was allowed to free glide until flight termination. It is important to note, that the flights were conducted in an unpredictable, outdoor environment. Therefore, to ensure gliding quality, flights were conducted on days with low wind (between 4-9 mph), good visibility and no precipitation. A glide was considered successful if the platform continued on a smooth path to the ground without undesirable behavior such as sudden impacts or flips. If a sudden crosswind threw the platform off course or caused hovering behavior, the data from that flight was discarded.

First, to create a baseline of data, the original Robo Raven1 wing was analyzed. The raw altitude was processed in the following manner. First, the data was properly analyzed taking into

account the actual time of flight. Obvious anomalous data was removed. Flight distance was calculated for the cleaned data from the latitude and longitude, via the @distvincenty Excel function. The final values were plotted. Visualization of the flight path began with the generation of a "smooth fit" from the data. Therefore, a 7^{th} degree polynomial function was fit to the data using the MATLAB polyfit function so that the flight path could be easily seen. The $C_{L,glide}/C_D$ ratio and flight path angle (θ) was evaluated using a "linear fit" averaged slope (also using the polyfit function) and equation 4.8. The final average $C_{L,glide}/C_D$ ratio and flight path angle (θ) can be seen in table 4.4.

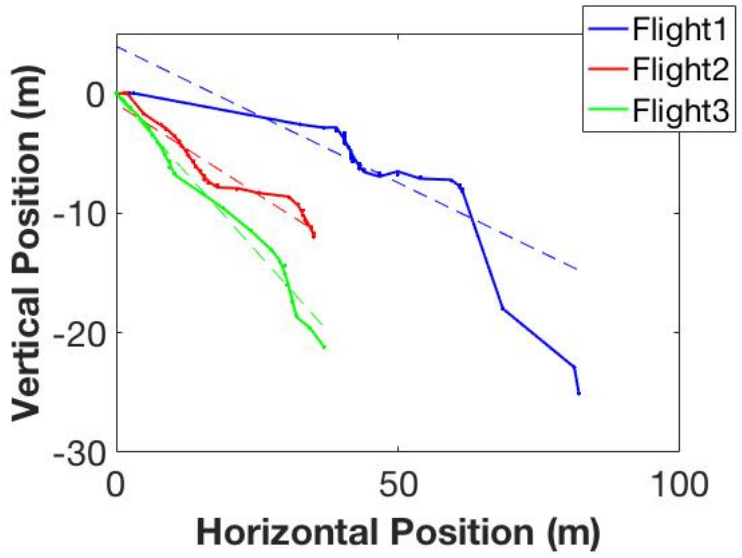


Figure 4.8: The graphical results of the $C_{L,glide}/C_D$ ratio experiments

Flight Parameter	Flight 1	Flight 2	Flight 3	Final Avg.	STDV
$C_{L,glide}/C_D$	4.38	3.32	1.90	3.2	1.24
Flight Path Angle θ	12.86°	16.76 °	27.76°	19.13°	7.73°

Table 4.4: Calculated average $C_{L,glide}/C_D$ ratio values for the original Robo Raven wing specimens after using a linear fit of the flight path data and the final overall average and standard deviation of the $C_{L,glide}/C_D$ ratio

Flight Analysis of Chosen Wing Sections

A set of two mirror wings was developed based upon each of the chosen specimen's planform parameters. The type, placement and angles of the carbon fiber spars remained the same as the original wing. The same thickness mylar sheet was also used for the wing's body. The chosen wing specimens were tested in the same manner and environment as the original Robo Raven wings. After the raw altitude was analyzed, the $C_{L,glide}/C_D$ ratios and flight path angles (θ) for each wing specimen were calculated. The results can be seen in table 4.6 below.

It was clear, from the resulting data, that simple changes in aspect ratio, taper ratio and wing area affected the glide performance. Each wing seemed to have distinct glide paths that were mostly similar to each other in shape. The shape of these paths had a few governing characteristics such as the number of changes in slope magnitude or changes in flight path angle from negative to positive. For instance, wing B's glide paths seemed to have a sudden drop in altitude, followed by a leveling off with alternating positive to negative changes in flight path angle θ. On the other hand, wing A dropped steadily, with moments of pitching up, but to a lower distance and did not seem to level off as much. Finally, wing E possessed many changes in slope but also dropped faster to a lower point. In recalling phugoid theory and the results from the test stand prediction study, it was clear that the overall change in slope magnitude and flight path angle ($\dot{\theta}$) was directly related to changes in the $C_{L,glide}/C_D$ ratio during the glide. The distinct signature of these changes was used to analyze the overall gliding performance for each wing.

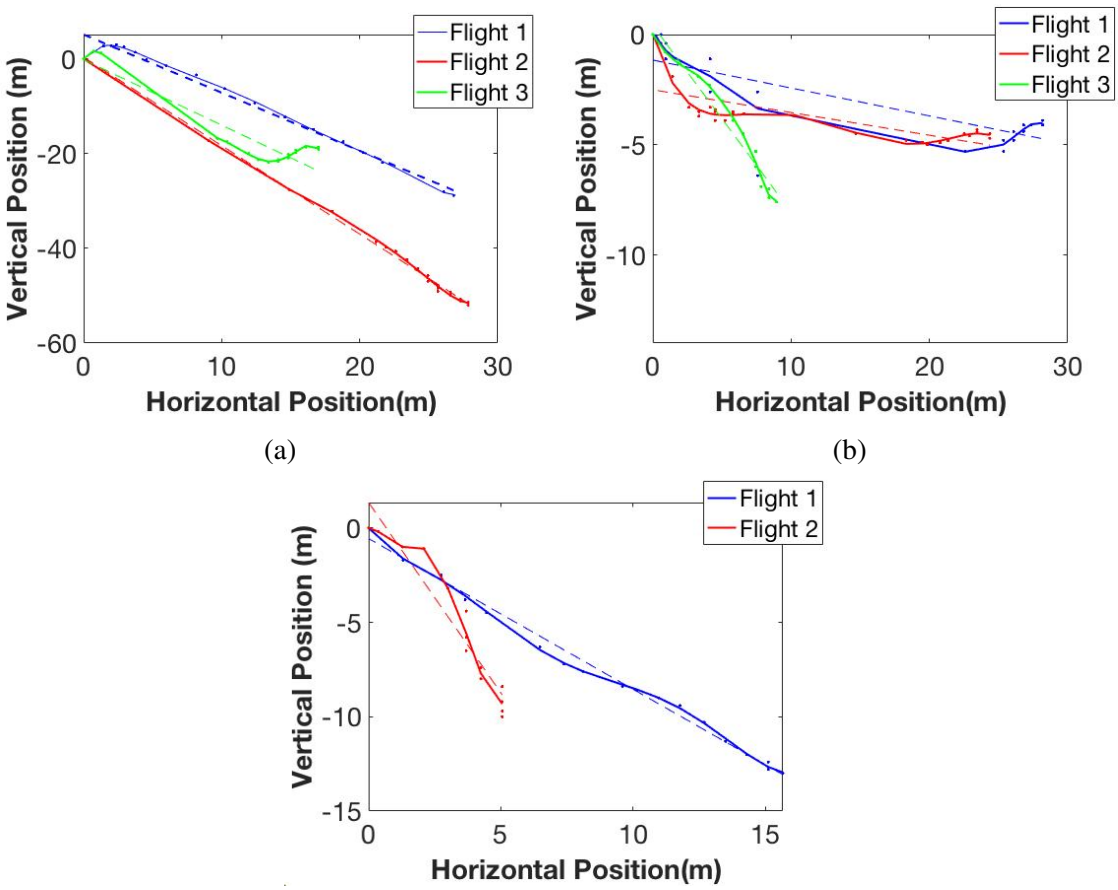


Figure 4.9: Flight demonstration results for the (a) Wing A (b) Wing B and (c) Wing E

Wing Specimen	Flight 1	Flight 2	Flight 3	Final Avg.	STDV
Wing A	50.82°	61.85°	54.10°	55.5°	5.66°
Wing B	7.222°	5.888°	40.26°	17.79°	19.47°
Wing E	38.62°	63.62°	N/A	51.12°	17.68°

Table 4.5: Calculated flight path angle θ values for each linearized path for each wing specimen

Wing Specimen	Flight 1	Flight 2	Flight 3	Final Avg.	STDV
Wing A	0.815	0.535	0.724	0.691	0.14
Wing B	7.891	9.697	1.181	6.256	4.49
Wing E	1.252	0.496	N/A	0.871	0.53

Table 4.6: Calculated average $C_{L,glide}/C_D$ ratio values for each of the wing specimens after parameterizing the flight path and the final average $C_{L,glide}/C_D$ ratio for each wing specimen

Finally, the averaged data was correlated to the wing planform parameters via a bi-linear,

Least-Mean-Squared fit. As was stated before, conventional aerodynamic theory states that as AR increases, drag should decrease. Interestingly, the final analysis showed a negative relationship between aspect ratio (AR) and $C_{L,glide}/C_D$ ratio. This is different than the conventional theory. However, it is important to note that Robo Raven wings are generally "low aspect ratio" wings [95], in that the numerical value of their span and chord is small (even if the ratio of span to chord is high). These types of wings are known to have unique properties that defy normal aerodynamic convention. Furthermore, these wings are highly flexible [95, 96] and twist dynamically during flight. The trailing edge of the wing is especially prone to morphing and twisting. This enables Robo Raven's flapping flight through quasi-steady aerodynamics, but this behavior is also known to affect the behavior of $C_{L,glide}/C_D)$ ratio in a way that defies stiff-wing aerodynamic convention [113, 114, 115]. It has been shown in related publications that convex, trailing edge morphing of a wing can increase the $C_{L,glide}/C_D$ ratio, whereas concave morphing can decrease it [113]. In previous Robo Raven research conducted by Perez-Rosado [97, 116], 3D DIC characterization conducted on the original Robo Raven wing showed that during a general downstroke, the wing tends towards a concave shape. In particular, there existed a highly convex region on the lower right portion of the wing. That region coincides with where the cross spars flex the most. Therefore, wings with simlar aspect ratios will have similar convex behavior. However, wings with higher aspect ratios possess less of this region and smaller length of the most flexible spar. Thus, their region of convexity is less and translated. These inherent aspects of the wing design may account for the unconventional $C_{L,glide}/CD$ ratio results.

Nevertheless, the gliding analysis showed a correlation between the modification of wing parameters and the magnitude of $C_{L,glide}/C_D$ ratio. This in turn shows the ability to tailor wing design for gliding performance.

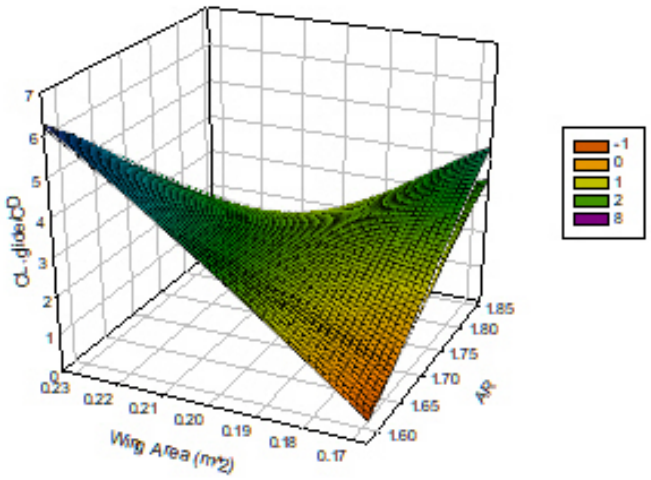


Figure 4.10: Modeled bilinear surface of $C_{L,glide}/C_D$ ratio as a function of aspect ratio, AR and planform area, A_w

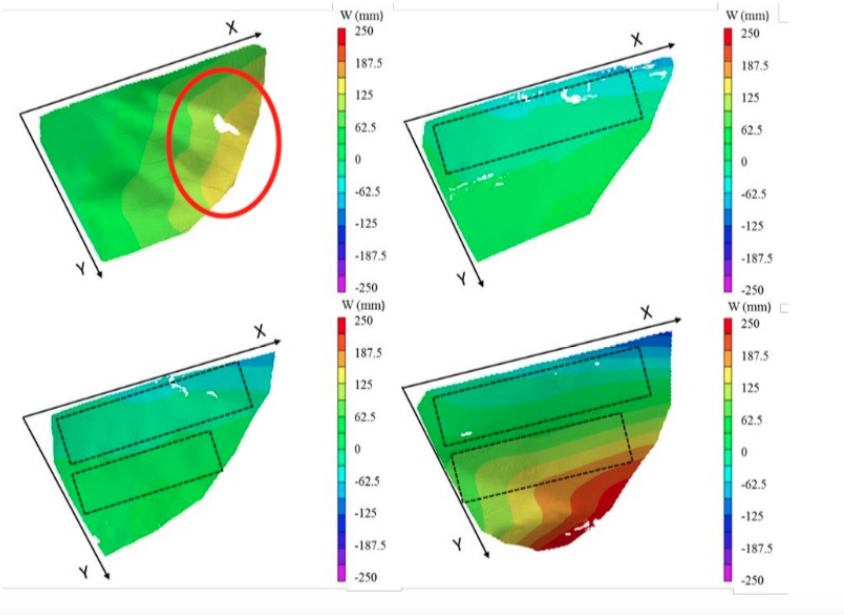


Figure 4.11: Comparison of displacement in Robo Raven wings during downward flapping. It displays the effect of variable in wing stiffness on wing flexion. This characterization was originally conducted in previous Robo Raven research by Perez-Rosado [116]. The region of high convexity in the original Robo Raven wing can be seen in the red circle.

By looking at the previous research for wings A and B, it is possible to consider an acceptable

"all-around" wing design for intermittent gliding. Wings A and B, being based upon wing designs from previous research [56, 95], have undergone test stand evaluation of their lift and thrust generating capabilities. The results can be seen in figure 4.12 below. From this information, it might be surmised that the data favors wing B for both flapping and gliding behavior. However, though it was possible to use wing B in a gliding flight, the size of this wing made it difficult to use in flapping flight. Use of this wing would require a slight change in the length of the platform that goes beyond the scope of this work.

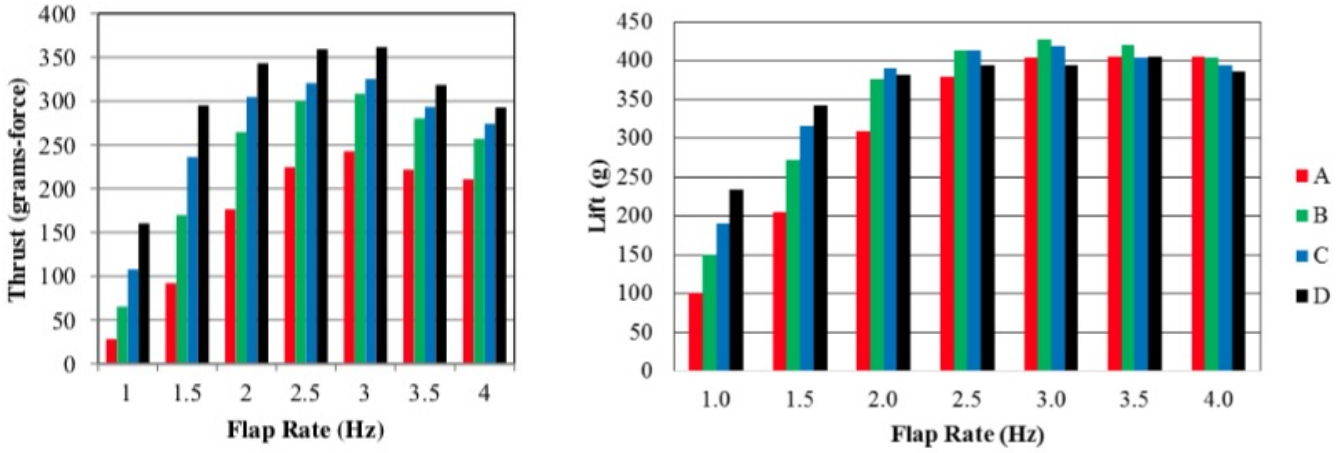


Figure 4.12: Measured thrust and lift values for wings A and B from previous research [56, 95] Please note, "wings C and D" have not been used in this chapter's gliding evaluations, but represent wings that have similar AR as wings A and B but have been scaled up in area.

4.4 Summary of Gliding Wing Characterization Results

The final design space utilized the information gained from the predictive study and flight analysis to create a pictorial representation of the direct relation between the chosen wing parameters and predicted gliding performance. Table 4.7 displays how a user might begin with a basic wing shape and by tailoring wing area or aspect ratio can change the angle of descent and $\Delta\, C_{L,glide}/C_D$ ratio throughout the flight as well as depth of glide and distance traveled during glide. It is also possible to tailor the design to decrease negative design aspects while maintaining good ones. For example,

one might increase both aspect and taper ratio at the same time to create a wing with the sliding performance of a higher area wing, but with less of the weight.

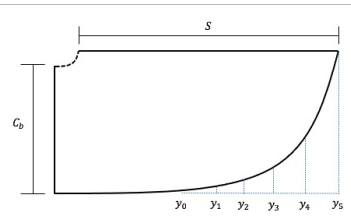
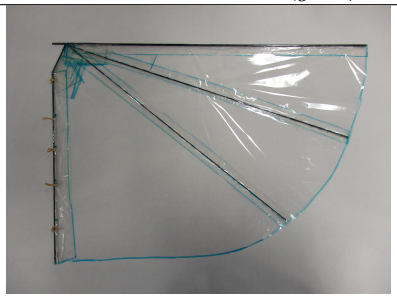
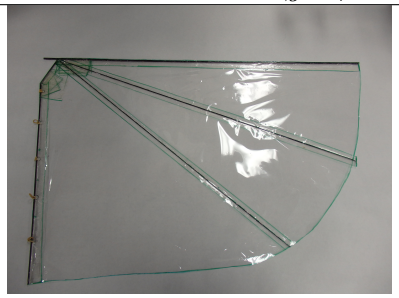
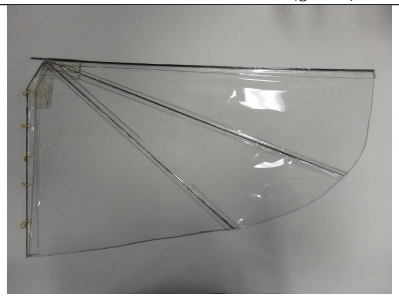
Begin with basic wing shape		
-11.6% AR, -8.2%A_w Decrease in + lift slope 78.41 % decrease in $C_{L,glide}/C_D$	-12.2% AR, +28%A_w Highest increase in + lift slope 95.5 % increase in $C_{L,glide}/C_D$	+3.4% AR, +20.9%A_w Increase in + lift slope 72.78 % decrease in $C_{L,glide}/C_D$
		

Table 4.7: Final summary of gliding wing characterization relating wing planform to slope of Lift and $C_{L,glide}/C_D$ values using information from the prediction study and the flight analysis

4.5 Conclusion

The overall goal of this chapter was to describe the exploration and characterization of a FWUAV wing planform design's effect on gliding performance parameters. To wit, in this chapter the following concepts were presented or developed. Wing specimens were designed and manufactured by a percentage increase or decrease of aspect ratio (AR), taper ratio (TR), and wing are (A_w) with respect to the original Robo Raven wing. Equations were developed that parameterized the unique Robo Raven wing planform and the $C_{L,glide}/CD$ ratio. These developed equations were used to analyze the gliding performance for each wing specimen. A predictive analysis was conducted which showed the dependence of lift generation on angle of attack and that there exists an angle of attack after which the platform loses lift and begins to stall. Flight analysis on both the original wing and the chosen wing specimens showed a distinct correlation between gliding behavior,

average $C_{L,glide}/C_D$ ratio and wing planform aspect ratio (AR), taper ratio (TR) and area (A_w). In comparison to the original Robo Raven wing, there was a -78.41 $\%$, +95.5 $\%$ and -72.78$\%$ change in average $C_{L,glide}/C_D$ ratio for the wing A, B, and E wings respectively. A bi-linear fit of the data showed an unexpected trend relating the change in AR to the expected change in $C_{L,glide}/C_D$ ratio. However, an effective explanation of this behavior was identified based upon the flexion of the wing during flight. It was shown through previous research that a highly concave region exists on the trailing edge of the wing which is decreased with an increase in aspect ratio. Concavity in the wing can affect the $C_{L,glide}/C_D$ ratio in a way similar to that seen in the experimental results. Finally, from previous thrust data, it was shown that Wing B was an acceptable overall wing design. However, use of this wing, due to its size, requires an adaptation to the Robo Raven body that was outside of this research's scope.

CHAPTER 5

FLIGHT VALIDATION OF HYBRID FLAPPING-GLIDING STATE SPACE MODEL

This chapter will present the experimental method by which the hybrid flapping/gliding model presented in chapter 3 was physically demonstrated. To begin, Robo Raven 1's conversion into a platform capable of measuring the model's performance parameters will be discussed. After this, results of continuous flapping and hybrid flapping-gliding flight demonstrations will be discussed.

5.1 Description of Modified Experimental Test Bed: Robo Raven 1

Examination of the Chapter 3 model through flight demonstration was done to (1) analyze the feasibility of implementing an intermittent flapping/gliding cycle on a real-world experimental apparatus; (2) characterize the effectiveness of intermittent gliding on improving the performance parameters of flight distance and battery performance; and (3) compare the model results with real values obtained during the demonstration. Therefore, the performance parameters outlined in Chapter 3, namely flight distance and battery endurance, governed Robo Raven 1 modification choices. As can be seen in Chapter 2, the original Robo Raven 1 platform possessed no sensing capabilities and was entirely controlled by an on board microprocessor. Thus, the original platform was adapted from its original configuration to include sensors that would enable the in-flight measurement of the performance parameters.

Priority was placed upon choosing sensors that were lightweight and/or could measure more than one parameter at a time. This choice was made to decrease the complexity of the modification, decrease the potential for sensor noise, and most importantly, to decrease excess weight. Besides flapping frequency and wing geometry, platform weight is the most important parameter in determining the ability of the platform to fly properly. From previous research [95, 49], it has been shown that a Robo Raven 1 weight of approximately 222 grams was capable of prolonged flight. Therefore, when the sensors were chosen, an accounting of weight was required. The individual

components of Robo Raven 1 were measured (without the addition of sensors) to understand the baseline weight of the platform. Table 5.1 shows the final weight measurements of Robo Raven 1 components.

Part	**Weight (g)**
Exterior Frame	24.8
Electronics and Wires	26.7
Front Servos and Holder	175.0
Tail and Holder	17.8
Wings	46.8
Additional Pieces	2.5
Final Total	293.6

Table 5.1: Weight account of the Modified Robo Raven1 Platform

With the platform showing flight capability at this weight, the choice was made to not add more than another (20g) of weight. Therefore, modifying the platform became an iterative process during which time, components were added or removed, the wings were tailored to the platform and even the wires were trimmed in length until the platform reached a desired weight. The final modified platform included sensors that could measure the desired performance parameters without the addition of too much weight.

5.1.1 Measurement of Battery Voltage

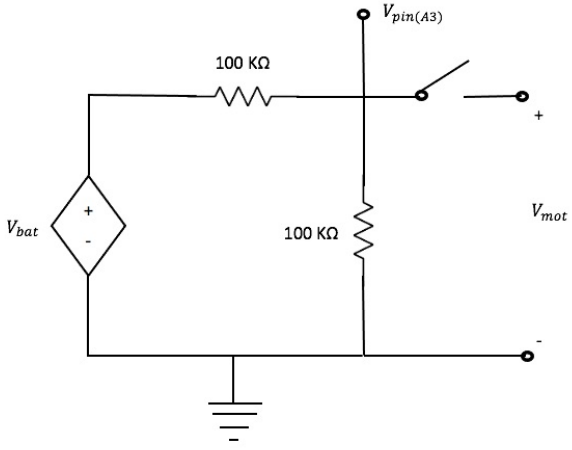
A sensor was designed to measure the battery voltage overtime during flight. The data collected from the voltage sensor would give real-world insight into the battery endurance performance parameter outlined in chapter 3. The choice of what type of sensor to use came down to three factors: weight, any potential current draw, and potential data noise. There were also concerns about safety, i.e whether or not the sensor's direct connection to the onboard battery would cause overheating or damage to the battery or circuit. During flights the platform often landed quite violently. Therefore, the durability of the sensor was also taken into consideration.

A voltage divider circuit proved to be a simple but effective voltage sensor and was also a lightweight addition to the platform. Its circuit, which can be seen in figure 5.1a consisted of

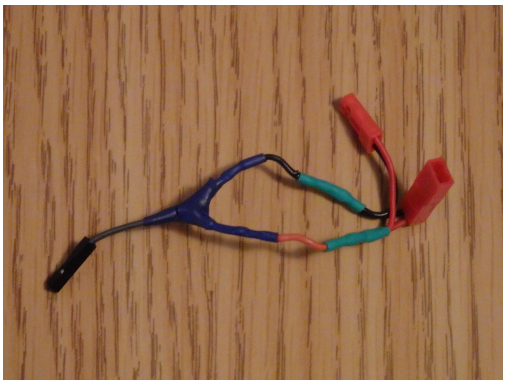
two 100KΩ resistors in series that mitigated harmful current to the Arduino analog A3 pin. In this circuit diagram, the battery was correctly characterized as a current-dependent source since the drain of battery voltage was dependent upon the current consumed by the system (mainly the servos). The flapping and gliding phases, and thus the change in current draw from the servos, was represented by a switch element in the circuit. The raw voltage, measured by the A3 pin (V_{pin}), was therefore represented by equation 5.1 below which was derived from equation 3.23.

$$V_{pin} = Z_{bat} + \sigma(t) R_{bat} I_{mot} \tag{5.1}$$

Recalling from equation 3.20 that the current in the motor, $I_{mot} = -I_{bat}$ the raw values as seen by the A3 pin were properly related to the flapping and gliding of the servos. The σ term represented the switch in the system between flapping to gliding. In essence when the platform flapped, the A3 pin measured the value of voltage as consumed by the servos. When the platform glided, the A3 pin measured only the residual voltage as represented by the battery's state-of-charge (Z_{bat}), which was itself an integral of the current drain overtime (recall equation 2.9). The final values were logged by the Arduino nano and, using serial connections, sent to the Teensyduino to be printed on the onboard SD card.



(a)



(b)

Figure 5.1: Voltage sensor (a) circuit and (b) picture

5.1.2 Final Robo Raven 1 Configuration and Block Diagram

A final configuration of the modified Robo Raven 1 platform contained both the GPS and voltage sensing capabilities, as well as internal logging capabilities. This was accomplished with the additional weight of only 17.7 g, and the utilization of a single external power source. A hardware and software systems diagram of the final configuration can be seen in figures 5.2 and 5.3. The controlling software on the Arduino nano board did not change with the modification. Therefore, the software diagram only displays the new software on the Teensyduino.

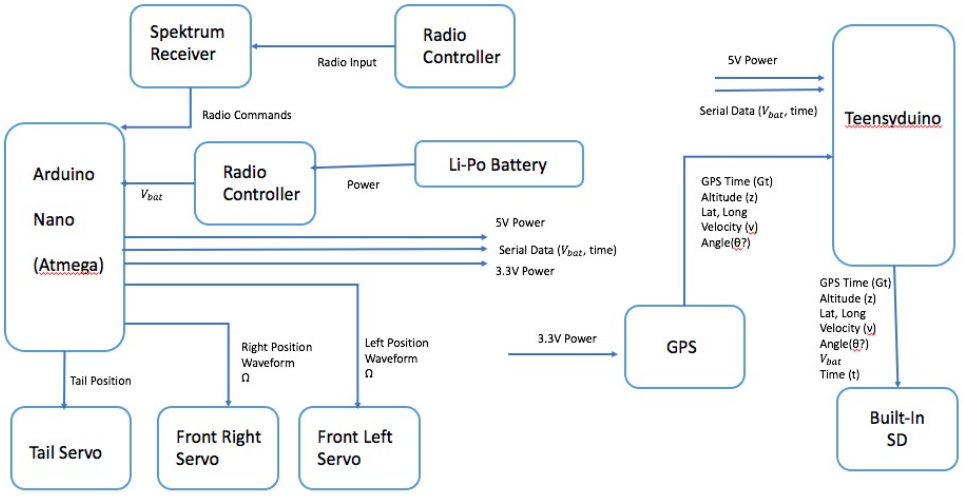


Figure 5.2: The modified Robo Raven 1 hardware system diagram

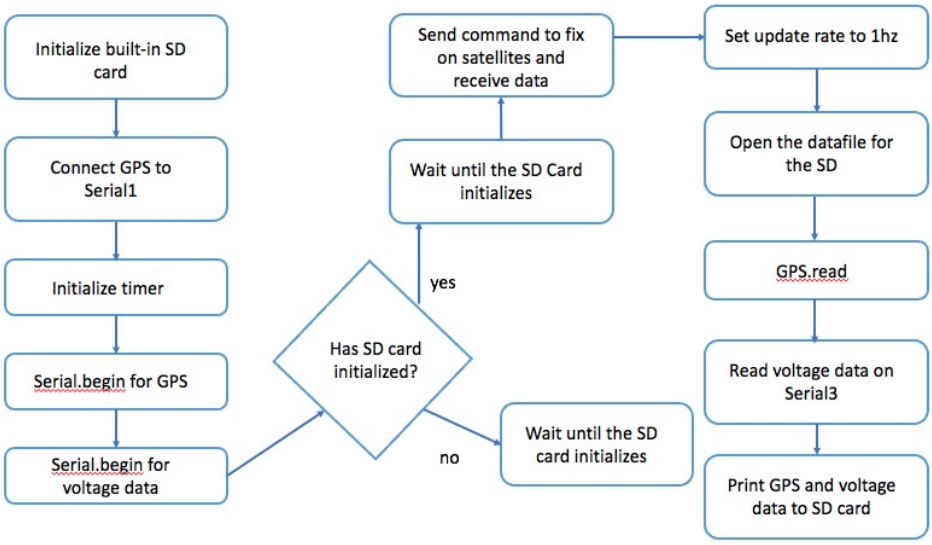


Figure 5.3: The modified Robo Raven 1 software system diagram

5.2 Experimental Flight Test Results

The flight simulations presented in Chapter 3 represented the investigation of three intermittent gliding techniques and their ability to improve flight performance. However, simulations alone cannot fully explore the potential of intermittent gliding. They were performed solely with ideal conditions and did not take into account various real-world factors that can affect flight behavior such as atmospheric conditions (wind, pressure change etc.) or changes in platform center-of-gravity during the flight. The simulations assumed that all of the intermittent gliding techniques could feasibly be conducted on a FWUAV and that the resultant flight outcomes were completely uniform. Therefore, flight analyses were conducted to correlate the real-world potential of intermittent gliding techniques with the simulated results.

5.2.1 Demonstration of Continuous Flapping Flight Behavior

Examining the real-world potential of intermittent gliding required an understanding of the modified Robo Raven1's flight behavior during a continuous flapping cycle; that is a cycle in which there is not intermittent gliding. The overall goal of this demonstration was to provide a baseline criterion by which to judge the outcome of a hybrid cycle that utilized intermittent gliding. The

desired outcomes of these flight demonstrations included graphical representations of flight and battery behavior as measured by the onboard sensors, as well as a potential emerging trend of flight performance from which inferences about overall flight behavior might be generated.

Previous research has shown that Robo Raven 1's flight performance can be easily influenced by environmental factors. Therefore, the flight environment was chosen carefully. Robo Raven was only flown during days with winds forecasted between 4 and 9 mph. Higher winds would often inhibit Robo Raven's ability to generate effective thrust and high wind gusts could cause a sudden loss of altitude. Moreover, Robo Raven 1 was flown in spaces with mostly flat ground that also preferably contained an amount of wind shelter from trees or bushes. Robo Raven 1 was flown during all seasons. However, special attention was paid to potential servo overheating during the summer. Preference was also given to spaces that contained as little metal objects or powerlines as possible. These factors would affect the GPS's ability to fix on satellites, causing delays in flight initiation and affecting data accuracy.

The demonstrations were conducted in the following manner. To initiate the flight, Robo Raven 1 was launched into the air by the human operator at approximately a 30° to 50° angle. Directional control during flight was given by the human operator. After launch the platform was then left to fly continuously until the platform reached the ground and the demonstration terminated. The platform would reach the ground for a variety of reasons including a loss of altitude (sudden or over time) or a depletion of the battery.

The specific variables measured during the demonstration were the geospacial position (latitude and longitude), flight speed (ν) (in knots), compass heading, altitude of the platform above sea level (z^*), time and date, and the number of fixed satellites. Also recorded was the battery load voltage (V) and the time of battery discharge. Overall flight distance (x) was calculated using the latitude and longitude data and the "distVicinity" function in excel. A 2D "satellite view" of each flight path was processed from the raw latitude, longitude and altitude data. The raw data was converted into flat earth coordinated using the "lla2flat" function in MATLAB. The final result seen in figure 5.4b shows the flight paths in easting and northing cartesian coordinates.

GPS measured altitude accuracy is variable and can depend upon such factors as the number of satellites on which the GPS has fixed and the amount of current received by the sensor. The altitude accuracy had a tendency to increase overtime as the GPS fixed on more satellites, thus generating a "settling trend" in the final data. Because the voltage overtime was also being measured, flight initiation could not always wait for the minutes it took for the GPS to finish settling. Therefore, anomalous data points were analyzed and removed after the flight. The "settling trend" was also analyzed and removed.

Finally, to truly represent the platform's gain in altitude vs. distance, the raw data had to be further converted and fitted. The altitude (z) referenced in Chapter 3 was the distance between the flying platform and the ground. However, the GPS worked on a "global system" the reference point for the raw altitude (z*) was the distance between the platform and the "current median sea level". Therefore, it was determined that relative altitude would be a better representation of the platform's real altitude. The raw altitude (z*) was converted using the following equation. The resulting data was smoothed via a 7th degree polynomial using the "polyfit" function in MATLAB.

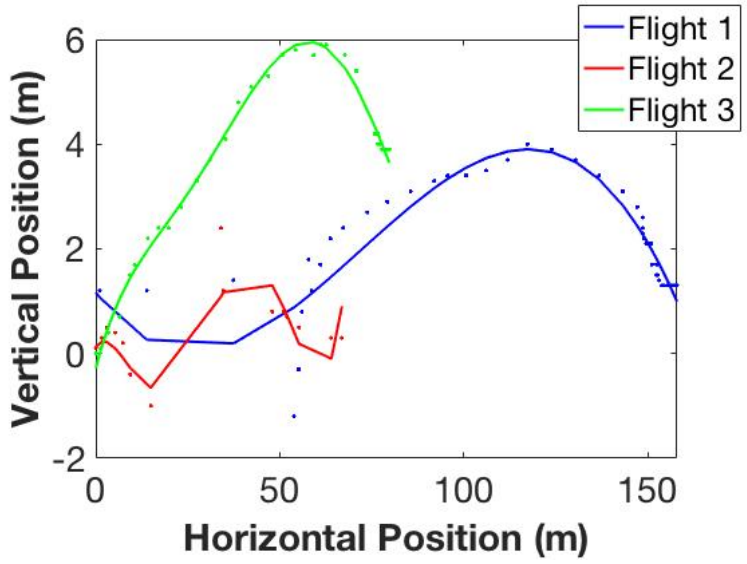
$$z = z^* - z^*(0) \tag{5.2}$$

Figure 5.4 shows the altitude (z) vs. flight distance (x) for each of the three flight demonstrations. The final values of x and z are not as high an amount as was seen in the Chapter 3 simulation. However, as was stated before, the simulation did not take into account the instantaneous variations in wind conditions, the weight of the platform, or other variables that affected Robo Raven's ability to gain and maintain altitude. However, the overall shape of the plots showed similar trends in climbing, leveling off and descent. These plots were used as a standard by which the hybrid plots were compared.

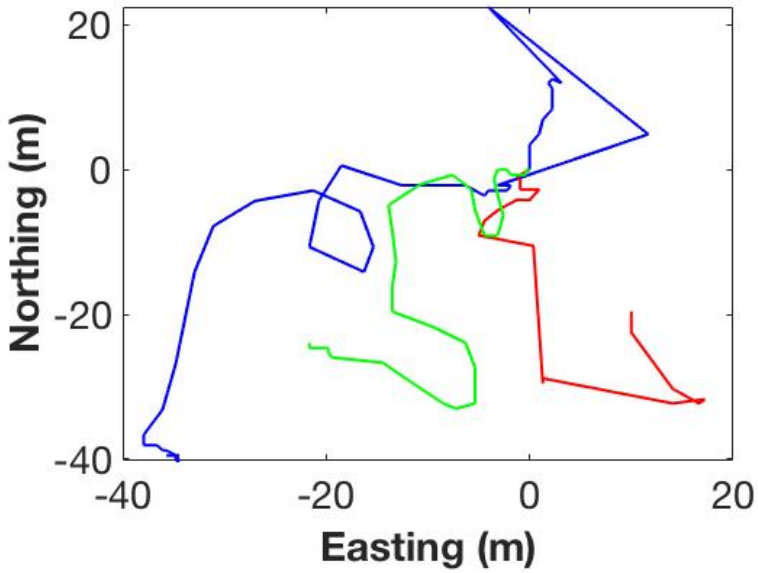
As was stated previously, the raw voltage, as measured using the Arduino A3 pin, was the consumed "system voltage" or the amount of voltage the Robo Raven1 components drew from the battery. The overall profile of figure 5.5 correctly depicted the behavior of the measured voltage overtime as predicted by equation 5.1. The overall profile was further corroborated by the measured

voltage of previous Robo Raven research [117]. According to the results of figure 5.5, when Robo Raven was not flapping, the voltage began at an initial voltage that corresponded to the full voltage supply in the battery. At this point, the platform was drawing all of the internal battery voltage. However, when Robo Raven1 began a flapping phase the servos, rated at 7.5 V operating voltage, drew the bulk of the battery voltage. Therefore, the measured voltage, V_{pin} dropped to this level. However, as the platform continued to flap, the battery drained itself and the measured voltage decreased. When the flight terminated, or Robo Raven entered a gliding phase, the measured voltage went back up to the full amount the battery could supply. This final (or resting voltage) was lower than the original value and a representation of the integrated state-of-charge as seen in equation 2.9.

The continuous flapping flight behavior was examined using the raw voltage data. The amount of battery drain, or ΔV_{bat}, was calculated via the following procedure. Firstly, the data was fitted using a 31st degree polynomial and the "polyfit" function in MATLAB. ΔV_{bat}, was defined as the difference between the initial measured voltage and the averaged resting voltage, or the values of V_{pin} when the flight had terminated. The final ΔV_{bat} values for each flight can be seen in table 5.2.

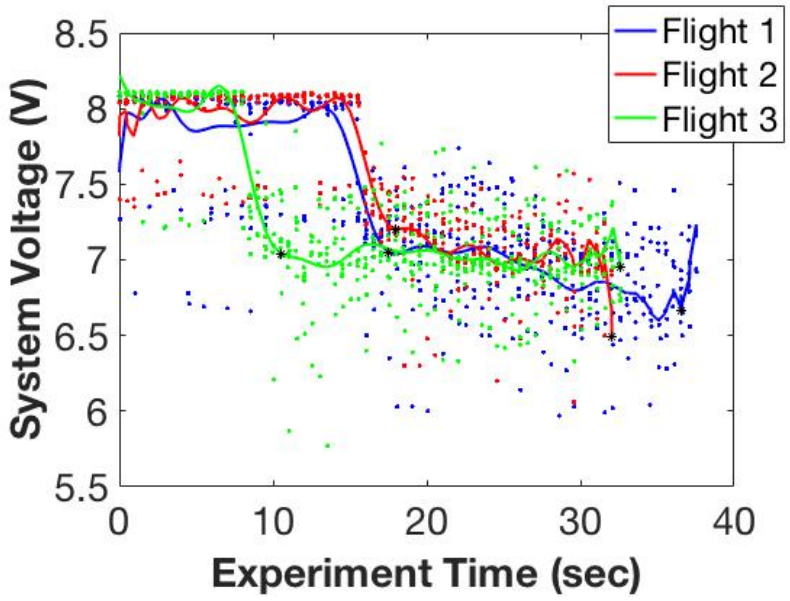


(a)



(b)

Figure 5.4: Flight demonstration results of continuous flapping flight (a) 2D phugoid profile, (b) Latitude vs. Longitude during flight for the three represented flights



(a)

Figure 5.5: (a) Raw voltage vs. time (b) voltage data trend lines for each flight

Flight	ΔV_{bat}
Flight 1	0.619
Flight 2	N/A
Flight 3	0.605

Table 5.2: $\Delta V_{bat}$for each of the continuously flapping flight demonstrations

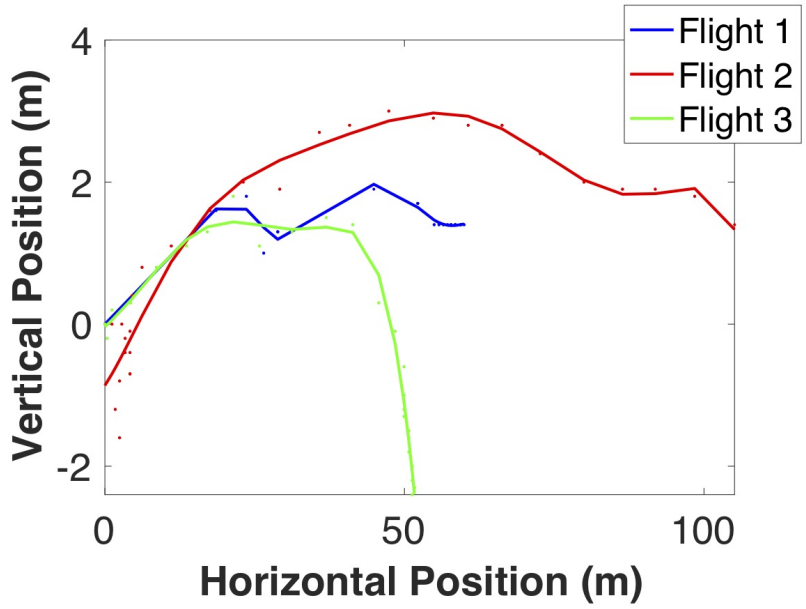
5.2.2 Demonstration of Hybrid Flapping/Gliding Flight

The hybrid flapping-gliding flights were characterized by alternating periods of thrust generating, platform ascent and periods of "zero" power draw, lift controlled descent. The hybrid flight demonstrations examined the real-world effects of intermittent gliding on Robo Raven1's flight performance by comparing the flight results with results of the continuous flapping flights and Chapter 3's simulations. It also allowed for the examination of the underlying behaviors and trends of flight behavior seen in real-world hybrid flight, that might be used to make inferences on the overall nature of hybrid flight.

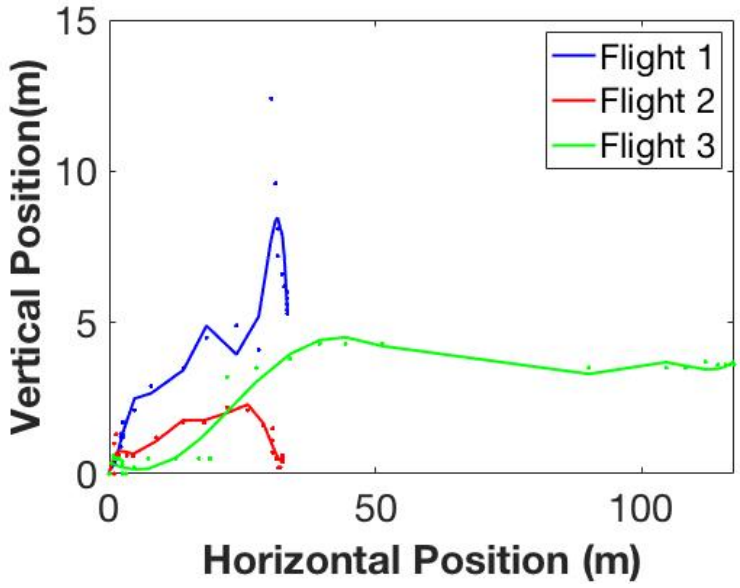
Due to real-world constraints, the hybrid flights conducted in these demonstrations were more

simplified and contained less cycles of flapping and gliding than in the Chapter 3 simulations. Demonstrations began with the simplest hybrid flight containing only two flapping cycles and one gliding cycle and increased in complexity to contain three flapping cycles and two gliding cycles. The hybrid flight demonstrations were conducted in the same flight environment as the flapping demonstrations and with a similar procedure. Switching from flapping to gliding behavior was controlled by the human operator. When to switch was predominantly determined by the platform's altitude and the human controller's intuition about the current atmospheric environment. A glide was not initiated until the platform was at a sufficient height such that a loss in altitude would not terminate the flight. Glides were also avoided when there seemed to be momentarily strong crosswinds.

The flight data was processed using the same procedure as the continuously flapping flights. The resulting flight path data is represented in figures 5.6-5.7. The results graphically demonstrated the feasibility of performing hybrid flights using the modified Robo Raven 1 platform. Since hybrid switching was determined by available altitude and atmospheric conditions, the glide times for both types of hybrid flights were more varied and often briefer in length than in the Chapter 3 simulations. Nonetheless, figure 5.6 correctly shows undulations in altitude that correspond with the switching from flapping to gliding phases.

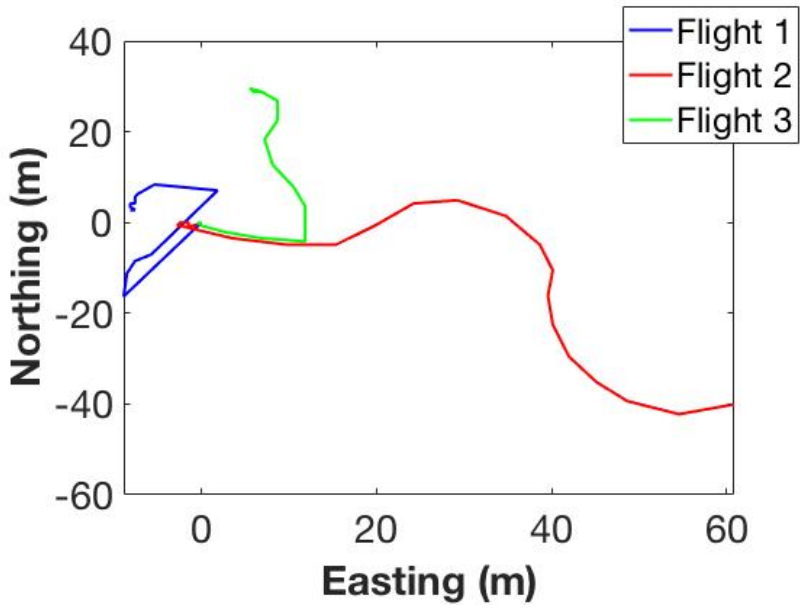


(a)

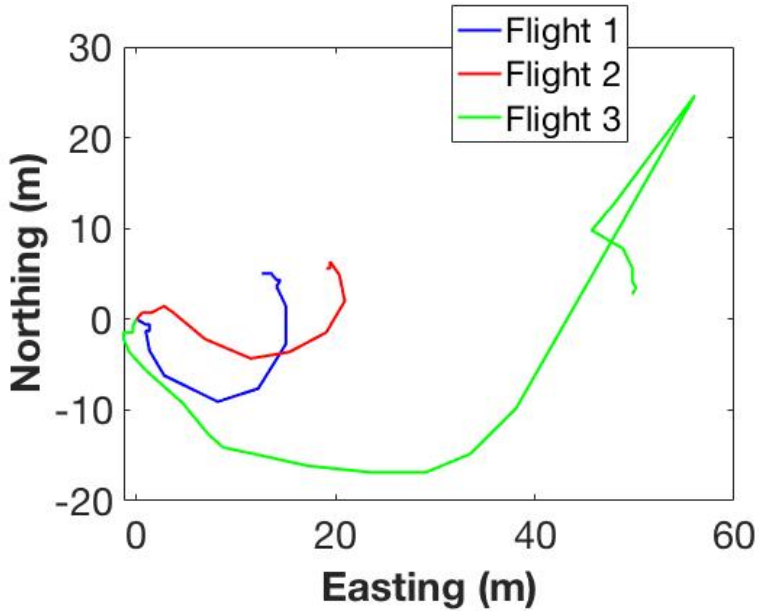


(b)

Figure 5.6: Flight demonstration results of 2D phugoid profile for hybrid flapping-gliding flights with (a) one gliding cycle (b) two gliding cycles

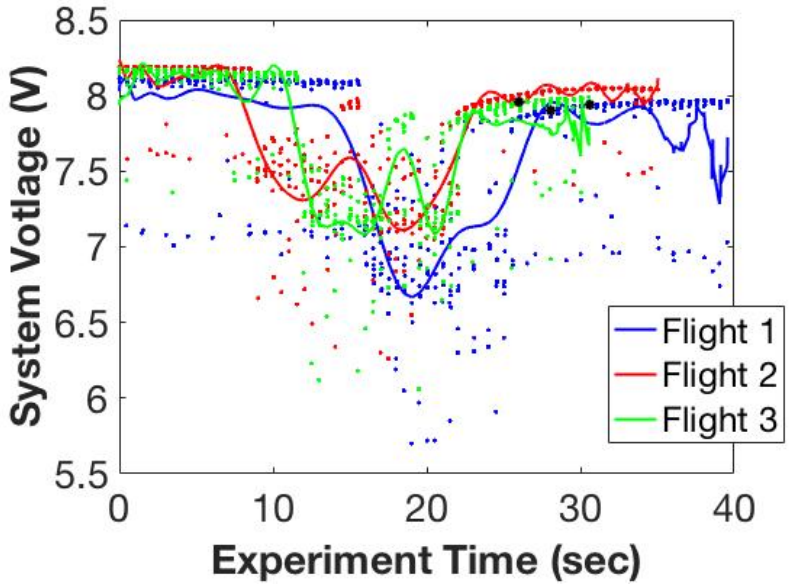


(a)

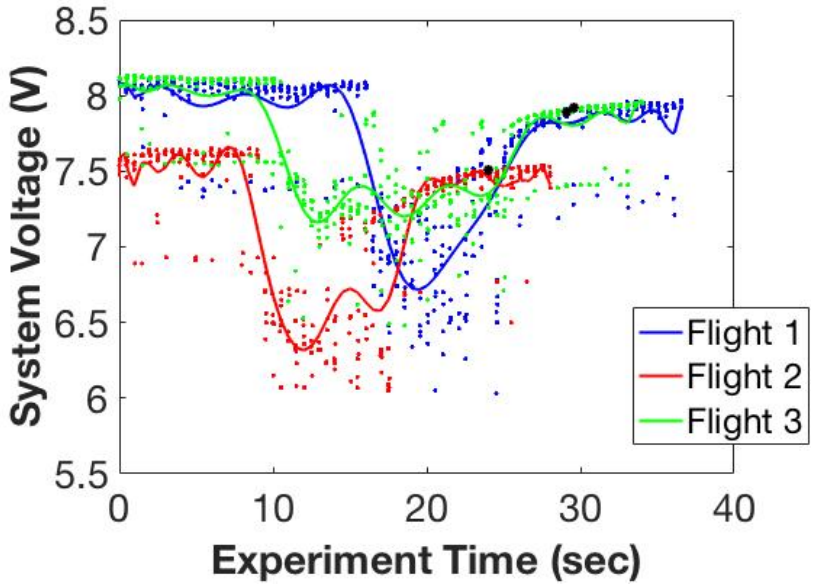


(b)

Figure 5.7: Flight demonstration results of Latitude vs. Longitude during flight with (a) one gliding cycle (b) two gliding cycles



(a)



(b)

Figure 5.8: Voltage discharge vs time for the hybrid flapping-gliding flights with (a) one gliding cycle (b) two gliding cycles

The average drop in battery voltage overtime was also calculated using the same procedure as the continuously flapping flights. Due to the constant switch from flap to glide, the voltage measured by V_{pin} experienced a settling behavior when the flight terminated. The average ΔV_{bat} values were taken after the voltage had reached a steady state. The points at which the estimated

steady state began can be seen as black *s on the graph. The average drop in battery voltage for each hybrid flight can be seen in table 5.3.

Flight	ΔV_{bat} **1 Glide**	ΔV_{bat} **2 Glide**
Flight 1	0.30	0.24
Flight 2	0.19	0.09
Flight 3	0.26	0.26

Table 5.3: ΔV_{bat} for each of the 1 glide and 2 glide hybrid flight demonstrations

The average ΔV_{bat} and discharge rate, the drop in voltage overtime, were calculated for all of the analyzed flights and compared with each other. This can be seen in table 5.4. It can be clearly seen from the data that implementing intermittent gliding techniques decreased the amount of battery drain overtime by between 32.03% and 46.09% when compared with a continuously flapping flight. In particular, it seems that the hybrid flight with two gliding cycles experienced the smallest amount of battery drain (46.09%). However, it is not clear if there is an upper limit (as seen in the Chapter 3 simulations) to the addition of gliding cycles above which performance begins to decrease.

The distance overtime, seen in table 5.5 was calculated for each of the flights. This value is much more difficult to use for effective evaluation due to the unpredictability of the data. It is also important to note that this data does not represent the "flight speed" of the platform, but rather the time averaged speed seen during the takeoff, cruising and landing phases of flight. Once more, the hybrid flight performed better than the continuously flapping flight, with the one glide flight performing 23.73% better and the two glide flight performing 16.95% better. Outside environmental influences, the flight limitations of the platform and other factors might contribute to there being less of an increase with the two glide flights.

Finally, the drop in voltage per distance, seen in table 5.6 was calculated to represent the spacial drain of the battery during flight. Both hybrid flights out performed the continuously flapping flight. The one glide hybrid flight outperformed by only 2.1% but the 2 hybrid flight outperformed by 29.6%. Each of these performance metrics show an improvement of flight when utilizing an intermittent gliding cycle.

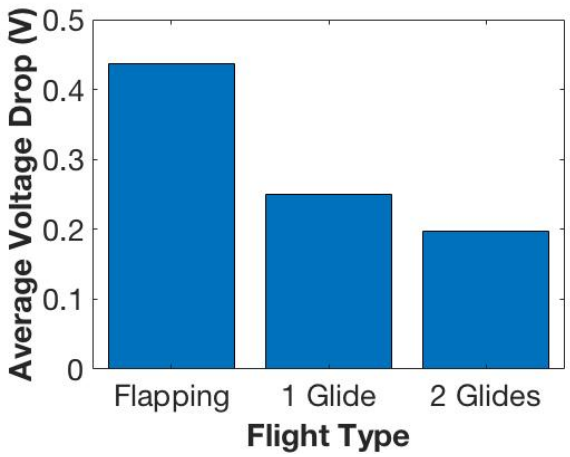


Figure 5.9: Average ΔV_{bat} values for the full flapping, 1 glide hybrid and 2 glide hybrid flights

Flight	1 (mV/sec)	2 (mV/sec)	3 (mV/sec)	Average (mV/sec)
Flap	10.3	N/A	15.2	12.8
1 Glide	9.8	5.4	10.8	8.7
2 Glide	8.1	3.7	8.9	6.9

Table 5.4: A comparison of the voltage drop vs. flight time for each of the flights and the average value for each flight method

Flight	1 (m/sec)	2 (m/sec)	3 (m/sec)	Average (m/sec)
Flap	4.32	2.09	2.45	2.95
1 Glide	1.96	1.78	2.99	2.25
2 Glide	1.97	1.35	4.04	2.45

Table 5.5: A comparison of the flight distance vs. flight time for each of the flights and the average value for each flight method.

Flight	1 (mV/m)	2 (mV/m)	3 (mV/m)	Average (mV/m)
Flap	2.38	N/A	6.20	4.29
1 Glide	5	3.04	N/A	4.2
2 Glide	4.11	2.74	2.20	3.02

Table 5.6: A comparison of the voltage drop vs. flight distance for each of the flights and the average value for each flight method.

5.3 Analysis of Aerodynamic Performance

5.3.1 Experimental Analysis of $C_{L,flap}/C_D$ Ratio

A major assumption of the simulations discussed in Chapter 3 was that the coefficient of lift during flapping, $C_{L,flap}$ and the coefficient of lift during gliding, $C_{L,glide}$ were different values. This assumption was based upon understanding of a fundamental change in aerodynamic regimes during Robo Raven's hybrid flight, from a steady state regime when gliding to a quasi-steady state regime when flapping. From this understanding it was hypothesized that the flapping motion of the wings during flight generated a separate lift from the almost "fixed-wing" lift generated when gliding. Therefore, it became a worthwhile endeavor to analyze the real-world $C_{L,flap}$ to C_D ratio, and explore the validity of this hypothesis. This was accomplished using the flight data gathered during the previously discussed, continuous flapping experiments.

Once again, a mathematical model representing the flight behavior of the platform during flight was developed. During climbing flight, the platform has the additional aerodynamic component of thrust. The thrust component, due to flapping was already defined in Chapter 3. Therefore, beginning with the modified phugoid (equation 3.7) and assuming that the rate of change in the flight path angle is 0, the following equation is derived.

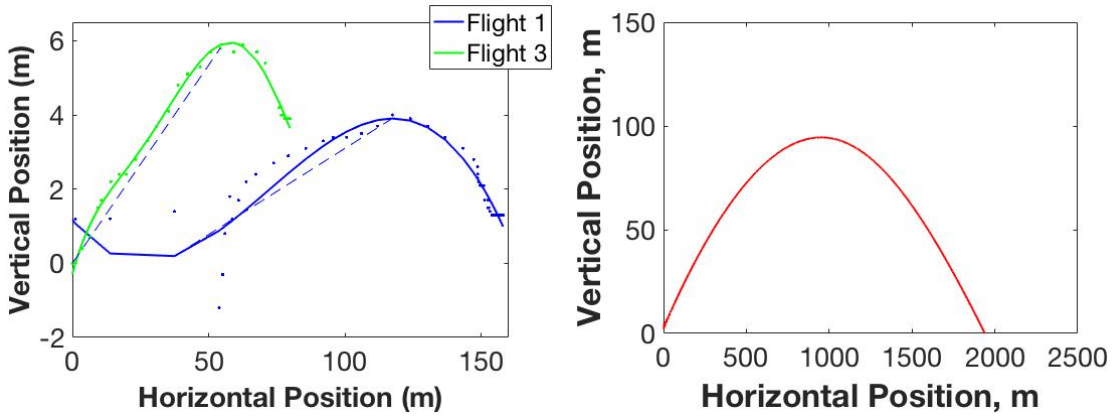
$$\frac{F_{thrust}}{m} = C_T \Omega_f^2 \tag{5.3}$$

Using a similar process to what was used for the ratio of $C_{L,glide}/C_D$, the aerodynamic coefficients were substituted for the forces. The resulting equation is a complex fraction that cannot be trigonometrically simplified. The flapping frequency, Ω_f and the thrust coefficient, C_T', are both known parameters. Furthermore, the variable, C_T' is represented by the equation 5.5. Therefore, this equation is still solvable, as there is only one unknown variable.

$$\frac{C_{L,flap}}{C_D} = -\frac{g\cos\theta}{g\sin\theta + C_T'\Omega_f^2} \tag{5.4}$$

$$C_T' = \frac{C_T}{m} \tag{5.5}$$

The highest amount of thrust generation is produced during the climbing phase of flight. It is also assumed that this is where the coefficient of lift due to flapping reaches its peak. Therefore, the angle of ascent was used as the θ for the ratio. A best fit slope line was used to determine the slope of climb and its associated flight path angle. Using the slope, and equation 5.4, it was possible to calculate the $C_{L,flap}/C_D$ ratio.



(a) (b)

Figure 5.10: A comparison of (a) the graphical results of the $C_{L,flap}/C_D$ ratio experiments with (b) the original simulated longitudinal dynamics

Ratio	Experimental	Original Simulation
$C_{L,glide}/C_D$	3.2	20
$C_{L,flap}/C_D$	1.4	5

Table 5.7: A comparison of the aerodynamic coefficient ratios between the original simulation values and the final values from this experiment. As can be seen, the values are very far off because the simulation assumed an optimized platform as stated before. Using the values from the experiment, the simulation values were modified to more system correct values

From the comparison of the experimental and original $C_{L,glide}/C_D$ and $C_{L,flap}/C_D$ ratios it is clear that the experimental platform is not the optimized platform assumed in the original chapter 3 simulations. However, They follow the simulation trend that the $C_{L,glide}/C_D$ ratio is both different and larger than the $C_{L,flap}/C_D$ ratio. It can also be seen from the comparison seen in figure 5.10

that the original simulated longitudinal flight path had a much higher altitude and distance than the experimental data. The lack of environmental disturbances such as cross winds, the out-of-plane movement of the Robo Raven tail and the decrease in flapping amplitude as the battery decays led to a simulation that grately over predicted the platform's flight path. Therefore, the simulation was qualitatively modified to more accurately fit the experimental data.

5.3.2 Modified Simulation of $C_{L,flap}/C_D$ Ratio based on Experimental Results

Improvement of the original simulation became possible through a qualitative, graphical fit of the simulated longitudinal curve to the experimental flight path. The goal of this modification was to improve the accuracy of the simulation based on realistic flight behaviors. To begin, the initial conditions were changed to more accurately fit the experimental conditions. The initial speed of the platform was lowered to below top flight speed. Furthermore, the initial height was changed to zero to fit the "relative altitude" of the experimental data. A full accounting of the new initial conditions can be seen in table5.8.

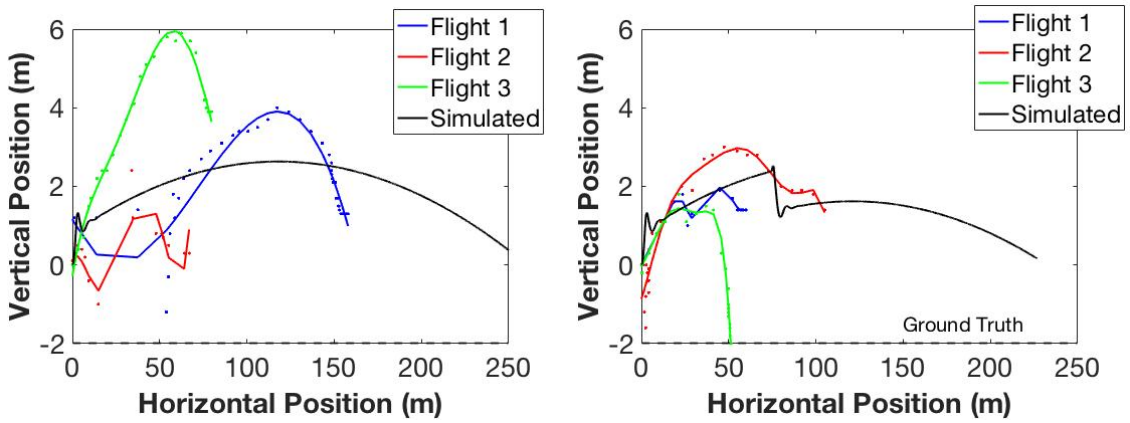
State	Description	Units	Initial Value
x	Horizontal position	m	0
z	Vertical position	m	0
θ	Flight path angle	rad	0
ν	Flight speed	m/sec	2
Ω	Motor angular rate	rad/sec	0
I_{mot}	Motor current	A	1
Z_{bat}	Battery state-of-charge	N/A	1
R_{bat}	Battery internal resistance	ohms	0.036
V_{bat}	Battery voltage	V	8.5

Table 5.8: Adjusted initial conditions of the combined flight, motor, and battery dynamical system

The experimental value of C_T was calculated using an understanding of drag forces generated from previous experiments [95] and equation 5.4. Assuming that the $C_{L,glide}/C_D$ ratio is the experimental value of 1.4, we arrive at the following calculations. Because of the flight path angle from the experimental data, a 6.107°angle was assumed.

$$0.3 * (9.8 * cos(6.107^{\circ})/1 - 9.8 * sin(6.107^{\circ}))/16 = 0.115 \tag{5.6}$$

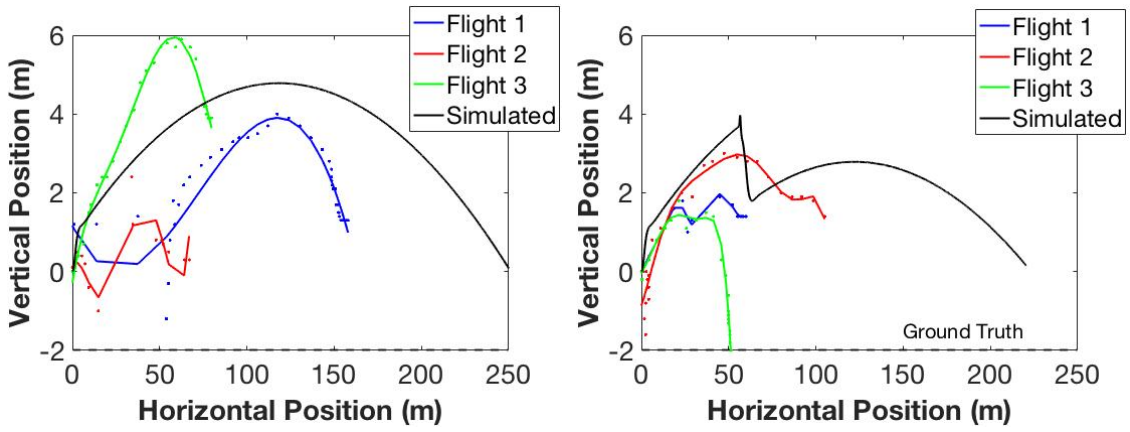
The paths plotted in figure 5.12 represent the superimposed fully flapping and one glide hybrid over the experimental data. Using the experimental ratios, and a coefficient of thrust adapted to the flight platform, the C_L/C_D ratios were changed until a more accurate flight path was formulated. Attention was most paid to the fitting of the maximum altitude and the flight shape. Assuming that the C_D was the same for both flapping and gliding (as was assumed in the previous simulation), the modified ratios, seen in table 5.9 were developed.



(a) (b)

Figure 5.11: A comparison of longitudinal dynamics for a fully flapping phase and a 1 glide hybrid phase for both the experimental flight paths and the modified simulations. The C_L/C_D ratio values for both flap and glide were achieved by adapting the C_T parameters to the flight apparatus and qualitatively fitting the curves to more geometrically fit the experimental curves.

After the initial adjustment, the simulation was further adjusted using the previous qualitative approach, according to a more correct coefficient of thrust. Using the modified aerodynamic ratios and equation 5.4 a more accurate coefficient of thrust was calculated. The graphs in figure5.12 show the adjusted flight path. Finally, modified and C_T modified simulation C_L/C_D ratios can be seen in table 5.9.



(a) (b)

Figure 5.12: Comparison of experimental results for longitudinal dynamics for a fully flapping phase and a 1 glide hybrid phase modified with the simulation using a C_L/C_D of 3 for glide and 1 for flapping, which are closer to what we expect from the Robo Raven 1 platform. The resulting simulated flight paths were also within the range of experimental measurements, similar to the flight paths in figure 5.11 that were qualitatively fit. Thus, it could be concluded that the sensitivity of the simulation to C_L/C_D values was in the range of uncertainty for the experimental data.

Value	Experimental	Qualitative Fit to Path	Value Closer to Experiment
$C_{L,glide}/C_D$	3.2	3.64	3.1
$C_{L,flap}/C_D$	1.4	2.12	1
C_T (kg-m)	0.111	0.067	0.163

Table 5.9: A comparison of the aerodynamic coefficient ratios between the experimental and modified simulations. The experimental coefficient of thrust C_T value was calculated using information from past drag experiments. The more correct coefficient of thrust C_T was calculated according to the ratio values.

5.4 Conclusion

This chapter presented the flight validation of hybrid flapping/gliding techniques and the state-space model first characterized in Chapter 3. In doing so, it explored the effects of intermittent gliding techniques on overall flight performance. To accomplish this goal, the Robo Raven 1 platform was modified to include sensing capabilities through the addition of GPS and voltage sensors. The modified platform was successfully flown in a series of continuously flapping and hybrid flights. The final data collected and analyzed from these flights showed that the use of

intermittent gliding in a flight had the ability to improve batter drain overtime by up to 46%, distance traveled overtime by approximately 24%, and the battery drain vs. flight distance by close to 30 %. The important assumption, from the Chapter 3 simulations, that $C_{L,glide}/C_D$ and $C_{L,flap}/C_D$ were distinct ratios was tested through real-world gliding flights. It was shown through the experimental results that these values are in fact different, though smaller in value than the ideal values chosen in Chapter 3. Using a qualitative, graphical fitting approach and the experimental data, the simulation was adjusted to a more correctly predict Robo Raven's flight behavior.

CHAPTER 6
CONCLUSION

6.1 Scientific and Technical Contributions

6.1.1 State Space Modeling the Flight Dynamics and Battery Utilization for Hybrid Flap/Glide Flight

Tracking the performance of intermittent gliding flight as it relates to the energy preserved overtime is a complex yet useful process in the development of aerial machines with extended flight times. This paper presented, to the author's knowledge, the first state-space model that directly related the aerodynamic performance and onboard power dynamics of a FWUAV. The simplified method for glide performance analysis allowed for the identification and characterization of multiple metrics for intermittent glide cycle designs. Resulting analysis further supported intermittent gliding as a successful method for flight extension. This method can be easily applied to any FWUAV with a programmable flapping frequency. Furthermore, this method can be adapted to other UAV systems via the modification of thrust representation. Finally, it can be used for further simulation of new intermittent cycle methods.

6.1.2 Gliding Wing Design and Performance Characterization

The tunability of conventional wing planform design to generate a desired type of flight is well documented. This work proved that a similar principle exists in unconventional FWUAV wing designs by showing distinct trends in flight behavior unique to specific wing planforms. Design spaces that allow users to track change in flight behavior as a function of wing planform parameters have been developed for both conventional and sub-micro FWUAV wings. The procedure presented in this work expanded the development of wing design spaces to the "bird-scale" level and presented viable non-laboratory analysis strategies. The demonstration of $C_{L,glide}/C_D$ ratio

dependence on angle-of-attack and planform-dependent slope change in lift, expanded the Chapter 4 flight analysis and proved the tunability of lift generation. Furthermore, the parameterization of gliding path based upon the spatial change in $C_{L,glide}/C_D$ ratio is a method that future researchers might use to characterize new wing planform designs.

6.1.3 Flight Validation of Flapping-Gliding State Space Model

Simulation of FWUAV intermittent gliding does not inherently prove that such methods can be successfully implemented on a real-life system. The unpredictability of such variables as the aerial environment, the vibrations of the platform due to flapping and the constant change in pitch and twist of the wings cannot be easily modeled in a simulation yet has significant impact on the effectiveness of an intermittent gliding flight. This work presented a method by which the addition of sensors to an FWUAV allowed for the real-life analysis of intermittent gliding viability. The analysis of real-world, hybrid flapping/gliding flights showed the viability of intermittent gliding as a flight extension method by demonstrating a positive effect on battery endurance during a flight. This work also presented evidence that the coefficient of lift due to gliding and flapping were distinct and different values. Furthermore, a framework was presented by which future researchers might determine the unique coefficients characteristic of their platforms. This provided important insight for the robust development of future FWUAV aerodynamic models.

6.2 Ongoing and Future Work

The analysis in Chapter 4 was able to prove a benefit of intermittent gliding on flight performance. However, it only featured human-controlled, altitude-based intermittent gliding and did not include flights with more than two gliding cycles. Therefore, future research should expand on this work by exploring the other modes of intermittent gliding simulated in Chapter 3, namely glide-switching based on voltage, time, and more varied altitude differences. While these methods can be accomplished with human control, it would be efficient to investigate the possibility of autonomous or semi-autonomous switching. To do this, the methods based on voltage and altitude will require

feedback loops that use the sensor data for decision making. In the past, autonomous, altitude-based diving was demonstrated on the Robo Raven platform [70]. A similar method might be adapted for autonomous gliding.

Only one form of bio-inspired, flight extension was explored in this research. The intermittent gliding method relied purely on the aerodynamic behavior and actuation mechanics of the platform. It did not take into account any external means of flight extension, nor did it pursue any non-sensor adjustments to the platform such as morphing wings, controllable tails or energy capture methods. In particular, morphing wings and controllable tails might be used to extend flights. The sinusoidal bounding behavior that some birds use to extend flight duration utilizes wing and tail morphing to turn the body into an aerodynamically advantageous shape. In another way, natural flyer's utilization of advantageous wind fields often involves the morphing of wingtips to "tack" into and out of the wind like a sail [13, 19]. Future work should also look into the possibility of combining a morphing wing method with internal mass movement to generate bounding behaviors for flight extension. Previous work on Robo Raven has shown the ability to control the platform's pitch in a glide through an internal weight-moving mechanism [118].

Furthermore, this work did not consider methods that advantageously use atmospheric conditions including different types of soaring methods and gust energy extraction methods. Future work might include the development of static soaring capabilities in a FWUAV. The autonomous loitering algorithm developed in previous Robo Raven research might be adapted for static soaring [98]. The algorithm (equation 6.1–6.2) uses a PID controller to create a circular flight path around a central GPS waypoint by controlling the tail position. In combination with a thermal seeking algorithm, the loitering algorithm might be adapted to generate advantageous static soaring flight paths. A thermal seeking algorithm could take many forms including a visual sensor method, like a camera, a temperature sensing method, or an energy state estimation method that mimic previous work [41, 43, 42]. There might even be the possibility of combining the aerodynamic advantages of flock flying with collaborative searching of a thermal [42].

$$u_i = K_p e_i + \frac{K_i}{2}(e_i - e_{i-1})\Delta t + \frac{K_d(e_i - e_{i-1}}{\Delta t} \tag{6.1}$$

$$TailPosition = NeutralTail + u \tag{6.2}$$

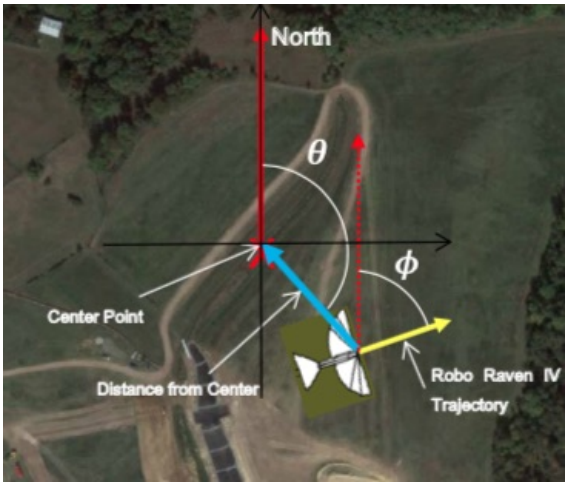


Figure 6.1: A pictoral representation of the PID controller parameters [98]

The use of dynamic soaring to further flight endurance is another method that should be researched in the future. As was stated before, autonomous dynamic soaring is difficult and therefore, the implementation of dynamic soaring might require the proper interaction of a human operator with a semi-autonomous platform as was seen in this work [37, 38]. The wing parameterization done in Chapter 5 could be expanded to the tailoring of wing designs for dynamic soaring performance. To accomplish this, wing specimens should be tested on their ability to either increase the coefficient of thrust, C_T during the climbing phase, or to increase the coefficient of Lift during the descending, gliding phase, $C_{L,glide}$. Path planning for soaring optimization would have to optimize wind shear utilization and the high altitude turning angle [34].

Finally, all of the results in this dissertation were confined to the Robo Raven1 platform. Future work should investigate an expansion of the simulations and experimental methods to the Robo Raven5, mixed-mode platform. The Robo Raven5 platform is capable of achieving higher altitudes and faster flight speeds and has, therefore, the potential to demonstrate more elaborate intermittent

gliding methods. It is also capable of a higher payload which allows for the development of a more complex and accurate suit of sensors. However, these advantages come with special considerations. Through an adaptation of the C_T, the simulation presented in Chapter 3 should be changed to include the thrust generated by the rear motors. Also, Robo Raven5 is powered by a larger 850mAh battery, as opposed to the smaller 350mAh battery that Robo Raven1 uses. This battery affords more charge, but the rear motors often deplete the battery quickly. Future simulations and flight demonstrations should take this into consideration.



Figure 6.2: A closeup of the Robo Raven 5 platform. Note the increase in payload afforded by the rear propellers

BIBLIOGRAPHY

[1] B. Galkin, J. Kabilda, and L. A. DaSilva, "UAV as Mobile Infrastructure: Addressing Battery Life," *IEEE Communications*, vol. 57, pp. 132–137, 6 2019.

[2] G. A. Folkertsma, W. Straatman, N. Nijenhuis, C. H. Venner, and S. Stramigioli, "Robird: A Robotic Bird of Prey," *IEEE Robotics Automation*, vol. 24, pp. 22–29, 3 2017.

[3] E. F. Helbling and R. J. Wood, "A Review of Propulsion, Power, and Control Architectures for Insect-Scale Flapping-Wing Vehicles," *Applied Mechanics Reviews*, vol. 70, 1 2018.

[4] A. Perez-Rosado, A. Griesinger, H. Bruck, S.K. Gupta, "Performance Characterization of Multifunctional Wings with Integrated Solar Cells for Unmanned Aerial Vehicles.," ASME IDETC/CIE, 2014.

[5] C. Patel and I. Kroo, "Control Law Design for Improving UAV Performance Using Wind Turbulence," 44th AIAA Aerospace Sciences Meeting and Exhibit, 2006.

[6] J. Cobano, D. Allejo, S. Vera, G. Heredia, and A. Ollero, "Multiple Gliding UAV Coordination for Static Soaring in Real Time Applications.," IEEE International Conference on Robotics and Automation, 2013.

[7] N. Depenbush, J. Bird, and J. Langelaan, "The AutoSOAR Autonomous Soaring Aircraft, Part1: Autonomous Algorithms," *Journal of Field Robotics*, pp. 868–889, 2019.

[8] B. Goodheart, "Tracing the History of the Ornithopter," *Journal of Aviation/Aerospace Education Research.*, 2011.

[9] O. Chanute, "Progress in Flying Machines," *American Engineer and Railroad Journal.*, 1894.

[10] E. Jamsari, M. Nawi, A. Sulaiman, R, Sidik, Z. Zaidi, and M. Ashari, "Ibn Firnas and His Contribution to the Aviation Technology of the World," *Advances in Natural and Applied Sciences*, vol. 7, pp. 74–78, 1 2013.

[11] U. Gulcat, *Fundamentals of Modern Unsteady Aerodynamics*. Springer, 2010.

[12] W. Shyy, H. Aono, C. Kang, and H, Liu, *An introduction to flapping wing aerodynamics*. Cambridge University Press, 2013.

[13] C. Pennycuick, *Modelling the flying bird*. Amsterdam, 2008.

[14] J. DeLaurier, "An Aerodynamic Model for Flapping-Wing Flight," *The Aeronautical Journal of the Royal Aeronautical Society*, 1993.

[15] T. Mueller and J. DeLaurier, "Aerodynamics of Small Vehicles," *Annual Review of Fluid Mechanics*, vol. 35, pp. 89–111, 1 2003.

[16] A. Hedenstrom, and G. Spedding, "Beyond robins: aerodynamic analyses of animal flight," *Journal of The Royal Society Interface*, vol. 5, pp. 596–601, 23 2008.

[17] J.M.Wakeling, "Dragonfly Aerodynamics and Unsteady Mechanisms: A Review," *Odonatologica*, vol. 22, pp. 319–334, 3 1993.

[18] D. Lentink, and M. Dickinson, "Rotational accelerations stabilize leading edge vortices on revolving fly wings," *Journal of Experimental Biology*, vol. 212, pp. 2705–2719, 16 2009.

[19] J. Videler, *Avian Flight*. Oxford University Press, 2005.

[20] G. Sachs, "In-flight measurement of upwind dynamic soaring in albatrosses," *Progress in Oceanography*, vol. 142, pp. 47–57, 2016.

[21] G. P. Sachs and B. Gruter, "Maximum travel speed performance of albatrosses and uavs using dynamic soaring," *AIAA Scitech 2019 Forum*, 2019.

[22] M. Denny, "Dynamic soaring: Aerodynamics for albatrosses," *European Journal of Physics*, vol. 30, pp. 75–84, 1 2008.

[23] Z. Akos, M. Nagy, S. Leven, and T. Vicsek, "Thermal soaring flight of birds and unmanned aerial vehicles," *Bioinspiration Biomimetics*, vol. 5, pp. 22–29, 4 2010.

[24] A. E. Holness, H. Solheim, H. A. Bruck, and S. K. Gupta, "A design framework for realizing multifunctional wings for flapping wing air vehicles using solar cells," *International Journal of Micro Air Vehicles*, vol. 11, 2019.

[25] A. Perez-Rosado, R. D. Gehlhar, S. Nolen, S. K. Gupta, and H. A. Bruck, "Design, fabrication, and characterization of multifunctional wings to harvest solar energy in flapping wing air vehicles," *Smart Materials and Structures*, vol. 24, 6 2015.

[26] J. Chen, R. Ghannam, M. Imram, and H. Heidari, "Wireless Power Transfer for 3D Printed Unmanned Aerial Vehicle (UAV) Systems," IEEE Asia Pacific Conference on Postgraduate Research in Microelectronics and Electronics, 2018.

[27] S. Anton, A. Erturk, D. Na Kong, and D. Inman, "Self-Charging Structures Using Piezoceramics and Thin-Film Batteries," In Proceedings of ASME Conference on Smart Materials, Adaptive Structures and Intelligent Systems, 2009.

[28] V. Bonnin, C. Toomer, E. Benard, and J. Moschetta, "Energy-Harvesting Mechanisms for UAV Flight by Dynamic Soaring," *International Journal of Micro Air Vehicles*, vol. 7, pp. 213–229, 3 2015.

[29] M. Deittert, A. Richards, C.A. Toomer, and A. Pipe, "Engineless Unmanned Aerial Vehicle Propulsion by Dynamic Soaring," *Journal of Guidance, Control, and Dynamics*, vol. 32, pp. 1446–1457, 5 2009.

[30] N. Lawrence, and S. Sukkarieh, "Autonomous Exploration of a Wind Field with a Gliding Aircraft," *Journal of Guidance, Control, and Dynamics*, vol. 34, pp. 719–733, 3 2011.

[31] N. Lawrance, and S. Sukkarieh, "A Guidance and Control Strategy for Dynamic Soaring with a Gliding UAV," 2009 IEEE International Conference on Robotics And Automation, 2009.

[32] N. Lawrance, "Autonomous soaring flight for unmanned vehicles," Ph.D. dissertation, University of Sydney, 2011.

[33] I. Mir, A. Maqsood, S. Eisa, H. Taha, and S. Akhtar, "Optimal Morphing-Augmented Dynamic Soaring Manuevers for Unmanned Air Vehicle Capable of Span and Sweep Morphologies," *Aerospace Science and Technology*, vol. 79, pp. 17–36, 2018.

[34] X. Gao, Z. Hou, Z. Guo, R. Fan, and X. Chen, "Analysis and design of guidance-strategy for dynamic soaring with uavs," *Control Engineering Practice*, vol. 32, pp. 218–226, 2014.

[35] M. Allen, "Autonomous Soaring for Improved Endurance of a Small Uninhabited Air Vehicle," 43rd AIAA Aerospace Sciences Meeting and Exhibit, 2005.

[36] Z. Li, and J. Langelaan, "Parameterized Trajectory Planning for Dynamic Soaring," AIAA SciTech Forum, 2020.

[37] M. Bolsough, "Autonomous Dynamic Soaring," 2017 IEEE Aerospace Conference, 2017.

[38] M. Boslough, "Autonomous dynamic soaring platform for distributed modile sensor arrays," Albuquerque, New Mexico, Tech. Rep., 2002.

[39] D. Edwards, "Implementation Details and Flight Test Results of an Autonomous Soaring Controller," AIAA Guidance, Navigation, Control Conference, and Exhibit, 2008.

[40] M. Allen, "Updraft Model for Development of Autonomous Soaring Unihabited Air Vehicles," 44th AIAA Aerospace Sciences Meeting and Exhibit, 2006.

[41] M. Allen and V. Lin, "Guidance and control of an autonomous soaring uav," Edwards, California, Tech. Rep., 2007.

[42] K. Cheng and J. Langelaan, "Guided Exploration for Coordinated Autonomous Soaring Flight," AIAA Guidance, Navigation, and Control Conference, 2014.

[43] M. Stolle, Y. Wanatabe, C. Doll, and J. Bolting, "Vision-Based Lifespan and Strength Estimation of Sub-Cumulus Thermal Updrafts for Autonomous Soaring," International Conference on Unmanned Aircraft Systems, 2016.

[44] N. Depenbusch, J. Bird, and J. Langelaan, "The AutoSOAR Autonomous Soaring Aircraft Part 2 Hardware Implementation and Flight Results," *Journal of Field Robotics*, vol. 35, pp. 435–458, 4 2017.

[45] K. Andersson, I. Kaminer, and K. Jones, "Autonomous Soaring; Flight Test Results of a Thermal Centering Controller," AIAA Guidance, Navigation, and Control Conference, 2010.

[46] L. Johnson, D. Paley, and H. Bruck, "Modeling the flight and battery dynamics of a flapping-gliding unmanned aerial vehicle," *Journal of Guidance Control and Dynamics*, vol. 44, no. 12, pp. 2276–2283, 2021.

[47] N. Gavrilovic, E. Bernard, P. Pastor, and J. Moschetta, "Performance improvement of small unmanned aerial vehicles through gust energy harvesting," *Journal of Aircraft*, vol. 55, no. 2, pp. 741–754, 2018.

[48] J. Langelaan and G. Bramesfeld, "Gust Energy Extraction for Mini and Micro Unihabited Aerial Vehicles," 46th AIAA Aerospace Sciences Meeting and Exhibit, 2008.

[49] A. Holness, H. Bruck, and S.K. Gupta, "Design of Propellor-Assisted Flapping Wing Air Vehicles for Enhanced Aerodynamic Performance," ASME IDETC/CIE, 2015.

[50] A. Ramezani, X. Shi, S. Chung, and S. Hutchinson, "Bat Bot (B2), A Biologically Inspired Flying Machine," IEEE International Conference on Robotics and Automation, 2016.

[51] A. Ramezani, S.-J. Chung, and S. Hutchinson, "A Biomimetic Robotic Platform to Study Flight Specializations of Bats," *Science Robotics*, vol. 2, 3 2017.

[52] K. De Clercq, R. de Kat, B. Remes, B. vanOudheusden, and H. Bijl, "Flow Visualization and Force Measurements on a Hovering Flapping-Wing MAV 'DelFly II'," AIAA Fluid Dynamics Conference, 2012.

[53] G. C. H. E. deCroon, M. Perçin, B.D.W. Remes, R. Ruijsink, and C. De Wagter, *The DelFly: design, aerodynamics, and artificial intelligence of a flapping wing robot*. Springer, 2016.

[54] G. C. H. E. deCroon, K. M. E. de Clercq, R. Ruijsink, B. Remes, and C. de Wagter, "Design, Aerodynamics, and Vision-Based Control of the Delfly," *International Journal of Micro Air Vehicles*, vol. 1, pp. 71–97, 2 2009.

[55] J. V. Caetano, M. Percin, C. C. deVisser, B. VanOudheusden, G. C. H. E. deCroon, C. deWatger, B. Remes, and M. Mulder, "Tethered vs. Free Flight Force Determination of the DelFly II Flapping Wing Micro Air Vehicle," International Conference on Unmanned Aircraft Systems, 2014.

[56] J. Gerdes, A. Holness, A. Perez-Rosado, L. Roberts, A. Greisinger, E. Barnett, J. Kempny, D. Lingam, C.-H. Yeh, H. A. Bruck, and S. K. Gupta, "Robo Raven: A Flapping-Wing Air Vehicle with Highly Compliant and Independently Controlled Wings," *Soft Robotics*, vol. 1, pp. 275–288, 4 2014.

[57] J. Gerdes, H. Bruck, and S.K. Gupta, "A Systematic Exploration of Wing Size on Flapping Wing air Vehicle Performance," ASME IDETC/CIE, 2015.

[58] A. Ramezani, S. U. Ahmed, J. Hoff, S.J. Chung, and S. Hutchinson, "Describing Robotic Bat Flight with Stable Periodic Orbits," *Biomimetic and Biohybrid Systems Lecture Notes in Computer Science*, pp. 394–405, 2017.

[59] G. C. H. E. De Croon, M. A. Groen, C. D. Wagter, B. Remes, R. Ruijsink, and B. W. V. Oudheusden, "Design, aerodynamics and autonomy of the DelFly," *Bioinspiration Biomimetics*, vol. 7, 2 2012.

[60] M. Lok, E. Helbling, X. Zhang, R. Wood, D. Brooks, and G. Wei, "A Low Mass Power Electronics Unit to Drive Piezoelectric Actuators for Flying Microrobots," *IEEE Transactions on Power Electronics*, vol. 33, pp. 3180–3191, 4 2018.

[61] N. Gaissert, R. Mugrauer, G. Mugrauer, A. Jebens, K. Jebens, "Inventing a Micro Aerial Vehicle Inspired by the Mechanics of Dragonfly Flight," *Towards Autonomous Robotic Systems Lecture Notes in Computer Science*, pp. 90–100, 2014.

[62] M. Rosen, G. Pivain, R. Sahai, N. Jafferis, and R. Wood, "Development of a 3.2g Untethered Flapping-Wing Platform for Flight Energetics and Control Experiments," IEEE International Conference on Robotics and Automation, 2016.

[63] B. Finio, and R. Wood, "Open-Loop Roll, Pitch, Yaw Torques for a Robotic Bee," International Conference on Intelligent Systems and Robotics, 2012.

[64] A. Desbiens, Y. Chen, and R. Wood, "A Wing Characterization Method for Flapping-Wing Robotic Insects," International Conference on Intelligent Systems and Robotics, 2013.

[65] Z. Toeh, S. Fuller, P. Chirarattananon, N. Perez-Arancibia, J. Greenberg, and R. Wood, "A Hovering Flapping-Wing Microrobot with Altitude Control and Passive Upright Stability," International Conference on Intelligent Robots and Systems, 2012.

[66] M. H. Rosen, G. lePivain, R. Sahai, N. T. Jafferis, and R. J. Wood, "Development of a 3.2g Untethered Flapping-Wing Platform for Flight Energetics and Control Experiments," 2016 IEEE International Conference on Robotics and Automation (ICRA), 2016.

[67] D. Olejnic, F. Muijres, M. Karasek, L. Camilo, C. Wagter, and G. C. H. E. deCroon, "Flying into the wind: Insects and bio-inspired micro-air-vehicles with a wing-stroke dihedral steer passively into wind gusts," *Frontiers in Robotics and AI*, vol. 9, 2022.

[68] S. Bansmer and R. Radespiel, "Flapping flight: High thrust and propulsive efficiency due to forward gliding oscilations," *AIAA Journal*, vol. 50, no. 12, pp. 2937–2941, 2012.

[69] D. Xue, B. Song, W. Song, and Z. Han, "Aeroelastic Optimization of Flap-gliding Micro Air Vehicle Wings," AIAA/ISSMO Multidisciplinary Analysis and Optimization Conference, 2016.

[70] L. J. Roberts, H. A. Bruck, and S. K. Gupta, "Modeling of Dive Maneuvers for Executing Autonomous Dives With a Flapping Wing Air Vehicle," *Journal of Mechanisms and Robotics*, vol. 9, 6 2017.

[71] S. Kamesh and S. Pradeep, "Phugoid approximation revisited," *Journal of Aircraft*, vol. 36, no. 2, pp. 465–467, 1999.

[72] M. V. Cook, *Flight Dynamics Principles (Second Edition)*. 30 Corporate Dr., Suite 400, Burlington, MA, 01803: Butterworth-Heinemann, 2007.

[73] L. Johnson, D. Paley, and H. Bruck, "Modeling the Flight Dynamics and Battery Utilization of a Hybrid Flapping-Gliding UAV," In Proceedings of AIAA SciTech, 2021.

[74] F. W. Lanchester, *Aerodonetics: Constituting the Second Volume of a Complete Work on Aerial Flight*. London: London: A. Constable, 1908.

[75] S. Sunderland, *The art of phugoid*, 2020 (accessed: 06.08.2020).

[76] M. Jongerden and B. R. Haverkort, "Battery modeling," *CTIT Report*, 2008.

[77] H. Hinz, "Comparison of lithium-ion battery models for simulating storage systems in distributed power generation," *Inventions*, vol. 4, no. 3, pp. 41–63, 2019.

[78] H. He, R. Xiong, and J. Fan, "Evaluation of litium-ion battery equivalent circuit models for state of charge estimation by an experimental approach," *Energies*, vol. 4, pp. 582–598, 2011.

[79] C. Zhang, J. Jiang, L. Zhang, S. Liu, L. Wang, and P. C. Loh, "A generalized soc-ocv model for lithium-ion batteries and the soc estimation for lnmco battery," *Energies*, vol. 9, no. 11, pp. 900–916, 2016.

[80] R. Zhang, B. Xia, B. Li, L. Cao, Y. Lai, W. Zheng, H. Weng, W. Wang, and M. Wang, "A study on the open circuit voltage and state of charge characterization of high capacity lithium-ion battery under different temperature," *Energies*, vol. 11, no. 9, pp. 2408–2425, 2018.

[81] G. Saldana, J. S. Martin, I. Zamora, F. Asensio, and O. Onederra, "Analysis of the current electric battery models for electric vehicle simulation," *Energies*, vol. 12, no. 14, pp. 1–27, 2019.

[82] S. M. Mousavi and M. Nikdel, "Various battery models for various simulation studies and applications," *Renewable and Sustainable Energy Reviews*, vol. 32, no. 1, pp. 477–485, 2014.

[83] B. Saha, E. Koshimoto, C. Quach, S. Vazquez, E. Hogge, T. Strom, B. Hill, and K. Goebel, "Predicting Battery Life for Electrical UAVs," In Proceedings of Infotech @ Aerospace 2011, 2011.

[84] B. Saha, C. Quach, and K. Goebel, "Optimizing Battery Life for Electric UAVs Using a Bayesian Framework," In Proceedings of IEEE Aerospace Conference, 2012.

[85] S. Mansouri, P. Karvelis, G. Georgoulas, and G. Nikolakopoulus, "Remaining useful battery life prediction for uavs based on machine learning," *IFAC Papers Online*, vol. 50, no. 1, pp. 4727–4732, 2017.

[86] M. Chen and G. A. Rincon-Mora, "Accurate electrical battery model capable of predicting run-time and i-v performance," *IEEE Transactions on Energy Conversion*, vol. 21, no. 2, pp. 504–511, 2006.

[87] W. Chang, "The state of charge estimating methods for battery: A review," *ISRN Applied Mathematics*, vol. 2013, no. 1-7, 2013.

[88] G. Sierra, M. Orchard, K. Goebel, and C. Kulkarni, "Battery health management for small-size rotary-wing electric unmanned aerial vehicles: An efficient approach for constrained computing platforms," *Reliability Engineering and System Safety*, vol. 182, pp. 166–178, 2019.

[89] L. Traub, "Validation of endurance estimates for battery powered uavs," *Aeronautical Journal*, vol. 117, no. 1197, pp. 1155–1166, 2013.

[90] B. Saha, E. Koshimoto, C. Quach, E. Hogge, T. Strom, B. Hill, S. Vazquez, and K. Goebel, "Battery Health Management System for Electric UAVs," In Proceedings of IEEE Aerospace Conference, 2011.

[91] L. Traub, "Range and endurance estimates for battery-powered aircraft," *Journal of Aircraft*, vol. 48, no. 2, pp. 703–707, 2011.

[92] H. Zhang, M. Zhou, and X. Lan, "State of charge estimation algorithm for unmanned aerial vehicle power-type lithium battery packs based on the extended kalman filter," *Energies*, vol. 12, pp. 3960–3975, 2019.

[93] S. Wang, C. Fernandez, Y. Fan, J. Feng, C. Yu, K. Huang, and W. Xie, "A novel safety assurance method based on the compound equivalent modeling and iterate reduce particle-adaptive kalman filtering for the unmanned aerial vehicle lithium ion batteries," *Energy Science and Engineering*, vol. 8, pp. 1484–1500, 2019.

[94] S. Jung and H. Jeong, "Extended kalman filter-based state of charge and state of power estimation algorithm for unmanned aerial vehicle li-po battery packs," *Energies*, vol. 10, pp. 1237–1250, 2017.

[95] J. Gerdes, "Improved prediction of flapping wing aerial vehicle performance through component interaction modeling," Ph.D. dissertation, University of Maryland - College Park, 2018.

[96] J. Gerdes and H. Bruck and S. Gupta, "Improving Prediction of Flapping-Wing Motion by Incorporating Actuator Constraints with Models of Aerodynamic Loads Using In-Flight Data," *Journal of Mechanisms and Robotics*, vol. 9, 2017.

[97] A. Perez-Rosado and H. Bruck and S. Gupta, "Integrating Solar Cells Into Flapping Wing Air Vehicles for Enhanced Flight Endurance," *Journal of Mechanisms and Robotics*, vol. 8, 2016.

[98] L. J. Roberts, H. Bruck, and S. K. Gupta, "Autonomous Loitering Control for a Flapping Wing Miniature Aerial Vehicle with Independent Wing Control," ASME IDETC/CIE, 2014.

[99] A. Holness, H. Bruck and S.K. Gupta, "Characterizing and modeling the enhancement of lift and payload capacity resulting from thrust augmentation in a propeller-assisted flapping wing air vehicle," *International Journal of Micro Air Vehicles*, vol. 10, pp. 50–69, 1 2017.

[100] E. Konuk and D. Landman, "Trajectory simulation with Battery Modeling for Electric Powered Unmanned Aerial Vehicles," In Proceedings of AIAA SciTech Forum, 2021.

[101] Platzer, M. and Jones, K. and Young, J. and Lai, J., "Flapping-Wing Aerodynamics: Progress and Challenges," *AIAA Journal*, vol. 46, pp. 2136–2149, 9 2008.

[102] A. Kundu, *Aircraft Design*. Cambridge, NY: Cambridge University Press, 2010.

[103] S. Ansari, K. Knowles, and R. Zbikowski, "Insectlike flapping wings in hover part 2: Effect of wing geometry," *Journal of Aircraft*, vol. 45, no. 6, pp. 1976–1990, 2008.

[104] Nicolai L. and Carichner G., *Fundamentals of Aircraft and Airship Design*. Reston, VA: American Institute of Aeronautics and Astronautics, 2010.

[105] Dauntless Software, *Wing planform*, 2022 [Online].

[106] A. Pelletier and T. Mueller, "Low reynolds number aerodynamics of low-aspect-ratio, thin/flat/cambered-plate wings," *Journal of Aircraft*, vol. 37, no. 5, pp. 825–832, 2000.

[107] T. Liu, K. Kuykendoll, R. Rhew, and S. Jones, "Avian wing geometry and kinematics," *AIAA Journal*, vol. 44, no. 5, pp. 954–963, 2006.

[108] Cornell Lab of Ornithology, *Birds and their wing shapes*, 2022 [Online].

[109] B. Singh and I. Chopra, "Insect-based hover-capable flapping wings for micro air vehicles: Experiments and analysis," *AIAA Journal*, vol. 46, no. 9, pp. 2115–2135, 2008.

[110] D. Liu and B. Song and W. Yang and X. Yang and D. Xue and X. Lang, "A Brief Review on Aerodynamic Performance of Wingtip Slots and Research Prospect," *Journal of Bionic Engineering*, vol. 18, pp. 1255–1279, 2021.

[111] Marchmann J., *Aerodynamics and Aircraft Performance, 3rd edition*. Blacksburg, VA: James F. Marchmann in Association with the University Libraries at Virginia Tech, 2021.

[112] Glenn Research Center, *Lift to drag ratio*, 2022 [Online].

[113] E. J. Chae, A. Moosavian, A. Pankonien, and D. Inman, "A Comparative Study of a Morphing Wing," 2017 Conference on Smart Materials, Adaptive Structures, and Intelligent Systems, 2017.

[114] L. Zhao, Q. Huang, X. Deng, and S. Sane, "The Effect of Chord-Wise Flexibility on the Aerodynamic Force Generation of Flapping Wings: Experimental Studies," 2009 IEEE International Conference on Robotics and Autonation, 2009.

[115] N. Beals, and A. Jones, "Lift Production by a Passively Flexible Rotating Wing," *AIAA Journal*, vol. 53, pp. 2995–3005, 2015.

[116] A. Perez-Rosado, "Design, fabrication, and performance characterization of multifunctional structures to harvest solar energy for flapping wing aerial vehicles," Ph.D. dissertation, University of Maryland - College Park, 2016.

[117] J.Gerdes, H. Bruck and S.K Gupta, “Improving Prediction of Flapping-Wing Motion By Incorporating Actuator Constraints With Models of Aerodynamic Loads Using In-Flight Data.,” *Journal of Mechanisms and Robotics*, vol. 9, 2 2017.

[118] A. Holness, “Strategies for enhancing performance of flapping wing aerial vehicles using multifunctional structures and mixed flight modes,” Ph.D. dissertation, University of Maryland - College Park, 2018.